Force Generation and Cytoskeletal Structure of Single Platelets

Molly Y. Mollica

A dissertation

submitted in partial fulfilment of the

requirements for the degree of

Doctor of Philosophy

University of Washington

2022

Reading Committee:

Wendy E. Thomas, Co-Chair

Nathan J. Sniadecki, Co-Chair

Jennifer Davis

Program Authorized to Offer Degree:

Bioengineering

University of Washington

Abstract

Force Generation and Cytoskeletal Structure of Single Platelets

Molly Y. Mollica

Co-chairs of the Supervisory Committee:

Nathan J. Sniadecki, Department of Mechanical Engineering

Wendy E. Thomas, Department of Bioengineering

Cardiovascular disease is the most common cause of death worldwide, and one in four deaths is related to dysfunctional blood clotting. Platelet forces are an emerging metric for the balance of clotting and bleeding due to recent demonstrations of their powerful abilities to predict bleeding risk in trauma patients and detect bleeding dysfunction more sensitively than all existing clinical tests. While existing methods have indicated the clinical and scientific potential of platelet forces, they have been hampered by low-yield, inability to co-measure immunofluorescent cell markers, and/or arbitrary restriction of cell spreading. To address these limitations, we developed a technique (dubbed “black dots”) that enables high-yield co-measurement of cellular forces and immunofluorescent-labeled cell markers in a single image without constraining cell spreading. Applying black dots to measure single-platelet forces, we identify biophysical factors that associate with force generation, determine the effects of platelet storage conditions on function, and identify unique cytoskeletal morphologies induced by

different key blood proteins. As a result of the high yield and high resolution of data obtainable with black dots, approaches including multivariate mixed effects modeling, K-means clustering, and machine learning were able to be applied to elucidate complex relationships between platelet activation, structure, and force generation. Identifying factors that associate with platelet forces, characterizing effects of storage temperature on platelet force generation, and elucidating platelets' complex reaction to activating proteins has implications in bleeding, clotting, and transfusion medicine.

Table of Contents

List of Figures ..... **v**

List of Tables ..... **vii**

Acknowledgements **1**

Chapter I: Introduction **2**

Chapter II: Background **4**

2.1 Measuring single-cell forces 4

2.1.1 Traction force microscopy (TFM) introduction 5

2.1.2 Wrinkling membranes on polysiloxane 6

2.1.3 Marker deformation on polysiloxane 7

2.1.4 Reference-free traction force microscopy 8

2.1.5 Alternative traction force materials: polyacrylamide, native ECM, and engineered gels 9

2.1.6 Deformable structures to measure cell forces: microposts or nanoposts 10

2.1.7 Deformable structures to measure cell forces: silicon cantilevers 13

2.1.8 Summary and future outlook on the measurement of single-cell forces 15

2.2 Platelets and the measurement of their force generation 16

2.2.1 Introduction: platelets and the role of their force generation 16

2.2.2 Measurement of single platelet forces 17

Chapter III: Black Dots To Measure Single Platelet Forces and Investigate Heterogeneity of Platelet Forces **21**

3.1 Introduction 21

3.2 Materials and Methods 23

3.2.1 Microfabrication of patterned stamp 23

3.2.2 Sacrificial PVA film production 23

3.2.3 Flexible PDMS substrate preparation 24

3.2.4 Microcontact printing and functionalization of black dots 24

3.2.5 Platelet isolation and seeding 26
3.2.6 Immunocytochemistry 27
3.2.7 Imaging and image analysis 27
3.2.8 Force calculation 28
3.2.9 Area and circularity calculations 29
3.2.10 F-actin dispersion calculation 29
3.2.11 K-means clustering 29
3.2.12 Statistics 30
3.2.13 Cell exclusion considerations 30
3.3 Results 32
3.3.1 Microcontact printing of black dots with uniformity in size, spacing, and shape 32
3.3.2 Reference-free traction force microscopy with black dots 33
3.3.3 Platelet forces correlate with spread area, circularity, and F-actin dispersion 35
3.3.4 Multivariate mixed effects modeling reveals cooperative effects between F-actin dispersion and circularity and between F-actin dispersion and spread area 37
3.3.5 Unbiased clustering supports relationship between spread area, circularity, F-actin dispersion, and platelet force 40
3.4 Discussion 41
3.5 Conclusion 42
3.6 Supplementary information 43
3.6.1 Supplementary Note 43
3.6.2 Supplementary Methods 44
3.6.3 Donor Specific Results 45
3.6.4 Technique Resolution, Yield, Sensitivity, and Traction Reconstruction Considerations 46
3.6.4 Supplementary Figures 49
3.7 Acknowledgements 60
3.8 Author contributions 60
Chapter IV: Forces of Stored Platelets 61

4.1 Introduction 61
4.2 Methods 61
4.2.1 Platelet collection and storage 61
4.2.2 Whole blood collection and preparation for the multi-platelet force assay 62
4.2.3 Preparation of washed platelets after storage for the single-platelet force assay 62
4.2.4 Multi-platelet (block and post) force assay 62
4.2.5 Single-platelet (black dots) force methodology 63
4.3 Results 65
4.3.1 Multi-platelet aggregation and force generation 65
4.3.2 Single-platelet spreading and force generation 67
4.4 Discussion 69
4.5 Author contributions 69
Chapter V: Cytoskeletal Morphology and Force of Platelets on VWF versus Fibrinogen 70
5.1 Introduction 70
5.2 Methods 72
5.2.1 Blood collection 72
5.2.2 Seeding platelets onto fibrinogen or VWF-treated coverslips 72
5.2.3 Black dots methodology 72
5.2.4 Fixing and immunofluorescent staining 76
5.2.5 Imaging via confocal microscopy and structured illumination microscopy 76
5.2.6 F-actin morphology assessment and machine learning 76
5.3 Results 78
5.3.1 Platelet F-actin morphology differs on fibrinogen and von Willebrand Factor and observed morphologies are detectable via machine learning 78
5.3.2 Platelets generate more force on VWF than on fibrinogen 80
5.3.3 F-actin structure corresponds to subcellular force localization 82
..... 83
5.4 Discussion 84

5.5 Author Contributions 85

Chapter VI: Discussion and Outlook 86

Black dots and measuring cellular force generation 86

Platelet forces have basic science and clinical significance 88

References 89

Appendix A: Bad Blood – Blood Research's Perpetuation of Racism & Standards Moving Forward 108

The perpetuation of racism by blood research 108

Standards for inclusion of race or racial inequities in blood research 112

List of Figures

Figure 1 – Cellular forces can be measured using deformable materials. 5

Figure 2 – The first method to study cellular forces involved silicone wrinkling. 6

Figure 3 – Cellular forces can be measured by the displacement of markers embedded in a deformable material. 8

Figure 4 – Cellular forces can be measured by the deflection of posts. 12

Figure 5 – Quantification of cellular forces by tracking the displacement of microposts. 13

Figure 6 – Black dots overview, manufacturing, and characterization. 32

Figure 7 – Black dots offer a higher yield way to measure forces. 35

Figure 8 – Platelet size, shape, and structure correlate with platelet force. 37

Figure 9 – Platelet size, shape, and structure do not strongly correlate with each other, but increase together with force. 38

Figure 10 – K-means clustering of platelet size, shape, and structure predict differences in force. 40

Figure 11 – ECM treatment of black dots. 49

Figure 12 – Selection of substrate stiffness. 50

Figure 13 – Black dots can be printed over larger areas. 51

Figure 14 – Field of view containing many platelets adhered to and contracting on the black dots. 52

Figure 15 – Force-area relationship by donor. 53

Figure 16 – Force-circularity relationship by donor. 54

Figure 17 – Force-F-actin dispersion relationship by donor. 55

Figure 18 – Platelet size, shape, and structure do not strongly correlate with each other, but increase together with force. 56

Figure 19 – Interaction plots demonstrate cooperative interactions between F-actin dispersion and circularity as well as F-actin dispersion and area. 57
Figure 20 – K-means clustering for each donor. 58
Figure 21 – Effect of pattern size on force estimation. 59
Figure 22 – Platelet aggregate force and area in response to shear flow. 66
Figure 23 – Single-platelet forces of stored platelets. 68
Figure 24 – From the literature: platelet F-actin morphology on fibrinogen and VWF. 71
Figure 25 – Platelet F-actin morphology differs on fibrinogen and von Willebrand Factor and is detectable via machine learning. 79
Figure 26 – Platelets on VWF produce more force and more force per area than platelets on fibrinogen. 81
Figure 27 – Higher resolution force analysis reveals correspondence between F-actin structure and subcellular force localization. 83

List of Tables

Table 1 – Review of platelet single-cell force studies. 19

Table 2 – Multivariate mixed effects model summary shows significant interaction effects.....40

Acknowledgements

I am deeply, deeply grateful to my labmates, graduate cohort, mentors, mentees, professors, colleagues, coaches, teachers, friends, family, and partner. Throughout my life and education, their support in the forms of scientific input, experimental assistance, career guidance, training, encouragement, emotional support, and more have immeasurably contributed to my education, my career, and the work in this dissertation.

Chapter I: Introduction

Upon vascular injury, platelets bind, reorganize their cytoskeleton, and generate forces to stop bleeding and strengthen a hemostatic plug. Reduced force generation of platelet aggregates in trauma patients is predictive of bleeding risk[1] and diminished force generation of single platelets is indicative of bleeding disorders[2]. Further, in some individuals who have a tendency to bleed or bruise easily but who have normal results for all clinically available bleeding tests, single-platelet force measurements revealed an absence of a subpopulation of highly contractile platelets present in healthy controls[2]. Studies of single-platelet forces have also revealed mechanical and chemical cues that impact force generation[2–4], surface receptors and signaling pathways involved in force transmission[2,5], and heterogeneity in force generation of platelets[2–8]. These results ultimately demonstrate the importance of platelet force generation in the regulation of hemostasis, the utility of measuring single-platelet forces, and the necessity to measure a large population of platelets to capture their force heterogeneity. While single-platelet force assays have been informative, existing methods to measure platelet forces have been hampered by low-yield, inability to co-measure immunofluorescent stains, and/or restriction of platelet spreading. Aim 1 of this dissertation addresses these limitations.

Aim 1: To develop a single-cell traction force technique that is high-yield, is compatible with immunofluorescent stains, and does not restrain cell size or shape, demonstrating its functionality measuring single-platelet forces.

While single-platelet forces are an emerging technique to characterize platelet function, it is unknown how storage conditions of platelet donations affect their force generation.

Aim 2: To assess the effects of platelet storage conditions on platelet force generation.

Studies seeding platelets onto fibrinogen result in early-bound platelets with punctate F-actin nodules and later-bound, spread platelets with elliptical, hollow F-actin morphology[2,3,6–20]. This F-actin morphology is

notably different from the homogeneous, solid F-actin morphology observed on von Willebrand Factor (VWF)[5,21]. F-actin structure on VWF and fibrinogen has not been compared directly and differences in nodule and hollow morphology have not been described in the literature. Additionally, platelet F-actin structure and subcellular force generation have not been investigated. Aim 3 of this dissertation investigates this difference in cytoskeletal morphology and its relationship to total platelet force and subcellular localization of forces.

Aim 3: To characterize platelet cytoskeletal structure and force generation on fibrinogen and VWF.

Taken together, these aims will provide a high-yield and high-resolution single-cell force measurement technique compatible with co-measurement of key cell markers without restraining cell size and shape. This technique will be employed to elucidate factors relating to the heterogeneity of forces, effects of storage and circulation time on platelet force generation, and alterations in cytoskeletal morphology on different activating proteins.

Chapter II: Background

2.1 Measuring single-cell forces

Cells are able to crawl, contract, and probe their physical surroundings through the generation of cytoskeletal forces.[22] Their ability to generate these forces is essential to the development, function, and maintenance of tissue for it provides a mechanism for cells to migrate to areas of need or pull together to provide shape and integrity to a tissue.[23,24] Failure to produce appropriate forces can facilitate developmental defects, poor tissue function, or diseased states.[25,26] The wide interest in cellular forces and their importance in cell biology has fueled the development of tools that can measure these forces in single cells and multicellular structures.

Cellular forces arise from regions of tension within the cytoskeleton that are transmitted to points of adhesion with the extracellular matrix (ECM) or between neighboring cells. Cytoskeletal tension is due to the motor activity of bipolar myosin filaments as it binds to two or more actin filaments, causing them to move past each other in an antiparallel fashion.[27] When a cell is attached to its environment (ECM or adjacent cells), the movement of cytoskeletal filaments causes contractile forces to be transmitted to that environment through sites of adhesion. These forces can range from the scale of piconewtons to nanonewtons depending on the size and maturation of the adhesion site, as well as the degree of actin-myosin activity within a cell.

Cellular forces transmitted to a cell's environment can deform the environment. Tools used to measure cellular forces, often termed traction force microscopy (TFM), measure the deformation of the environment to quantify the amount of force the cell produces. This calculation of cell forces relies on the fundamental principle of Hooke's Law: the amount of force applied to an elastic material is linearly related to the amount of deformation observed in the material. The measurement of cellular forces is a difficult task because of their microscopic size and transmission of force to multiple points of adhesion that are nanoscale.

Moreover, cells are living entities that respond to physical stimuli.[28] Thus, an additional challenge traction force microscopy is characterizing cell forces without inadvertently affecting their function.

2.1.1 Traction force microscopy (TFM) introduction

The first approaches to measure cellular forces were performed on deformable materials. It is common with these approaches to seed cells onto the surface of a substrate that has adhesive ligands for cellular attachment. As cell generate cell-matrix forces at their locations of adhesion, they cause the substrate to deform. Since a cell's adhesions are often distributed within the cell-substrate interface, they can be described as tractions, i.e. force per unit area. The magnitude and direction of cellular forces are inferred by the amount of deformation at its surface (Figure 1A).

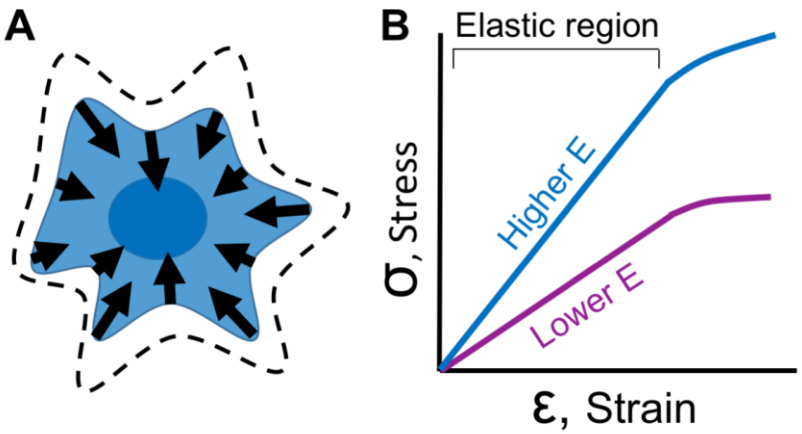

Figure 1 – Cellular forces can be measured using deformable materials. (A) A cell grown on the surface of a deformable material produces contractile forces that causes displacements on the surface of the material. Dashed lines represent the projected cell area before contraction. Arrows indicate the location, direction, and magnitude of the forces produced by a cell. (B) To measure cellular forces, elastic materials are often used which have a linear relationship between applied stress and observed strain. The slope of this linear relationship is referred to as the modulus of elasticity or Young's Modulus (E). To achieve the same amount of strain in a soft (lower E, purple line) or stiff material (higher E, blue line), more stress needs to be applied to the stiff material. Once the Young's Modulus of a material is known, one can measure deformation caused by cellular forces and infer the magnitude and direction of those forces. This figure was published in [94].

To infer cellular forces from material deformation, a key material relationship must be characterized: the proportion in which applied forces cause deformations to a material. This relationship is usually described as stress versus strain (Figure 1B) where stress (σ) is the applied force divided by the area over which it is applied and strain (ε) is the ratio change in distance between points on a surface. Knowing the stress versus strain behavior of a material enables one to calculate the modulus of elasticity (E) or Young's Modulus, which is the slope of the stress versus strain data in its linear elastic region (Figure 1B). It is ideal to use materials whose chemistry and manufacturing process lead to stable and consistent material properties. Materials historically and commonly used include polysiloxane (silicone), polyacrylamide, native ECM, and engineered gels.

2.1.2 Wrinkling membranes on polysiloxane

The first work to measure cellular forces involved seeding cells on a thin membrane of polysiloxane, more commonly known as silicone rubber. As a cell contracted or migrated, the membrane deformed to the point that it buckled or wrinkled (Figure 2A).[29] This technique was used to compare forces of different cell types, noting that fibroblasts produced the most wrinkles (Figure 2B), while macrophages were less contractile and cause no wrinkles on the surface.[30] The authors of this seminal work made their deformable substrates by exposing a film of polysiloxane fluid to a flame in order to crosslink a thin membrane at the surface of the polymer. Composed of a silicon-oxygen backbone, polysiloxane is considered biologically inert and non-toxic. Additionally, the material is linearly elastic within the range of forces produced by cells. Polysiloxanes are also relatively unsusceptible to problems due to biochemical exchange, such as shrinkage. Perhaps their greatest advantage is their transparency to optical and fluorescence microscopy, which make it possible to observe the cells as well as the wrinkles they cause.[29]

Others expand on the original wrinkling method by using UV irradiation to reduce the stiffness of the polysiloxane membranes, making it more permissible to wrinkling at a lower range of cellular forces.[31,32] This method was used to measure cellular forces during cytokinesis[31] and to examine the dynamics of cellular forces during cell locomotion[32]. Silicone wrinkling has also been used to assess the regulation of

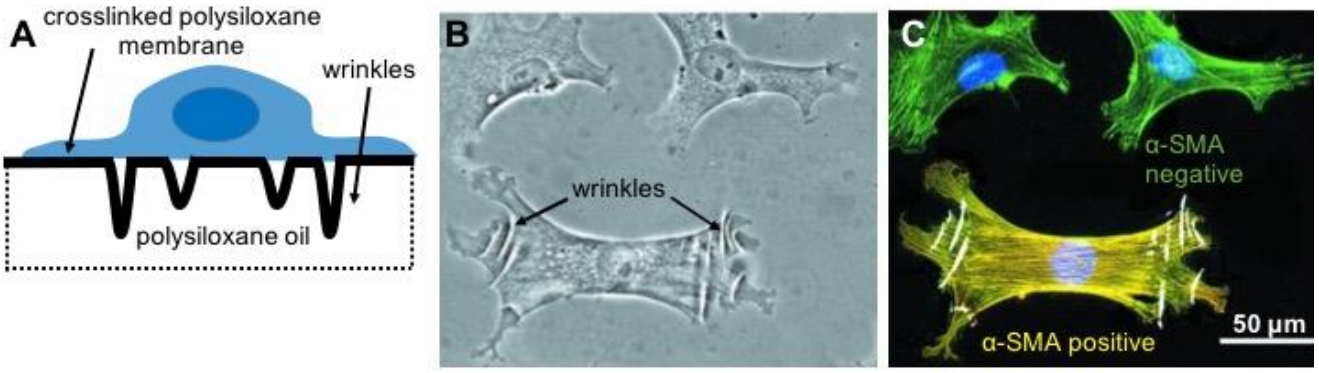

Figure 2 – The first method to study cellular forces involved silicone wrinkling.
(A) Cells were seeded on a polysiloxane fluid that was briefly exposed to a flame to crosslink a thin surface. Cellular forces deformed the membrane and caused to buckle or wrinkle. (B) Wrinkles in the silicone membrane can be visualized under light microscopy. (C) When used in conjunction with fluorescent microscopy, the magnitude of cellular forces can be correlated with the expression of biomarkers. For example, a fibroblast that is positive for α-smooth muscle actin (SMA) (yellow) create cellular forces that produce visible wrinkles, unlike those that are negative for α-SMA (green). B and C are adapted from [34]. This figure was published in [94].

myosin activity by caldesmon[33] and to identify α-smooth muscle actin as a biomarker of contractile myofibroblasts[34] (Figure 2B-C). This wrinkling method was groundbreaking to the field and was a simple method to adopt by others, requiring only silicone oil and a flame, but also necessitated a fair degree of skill to produce membranes that were consistent in thickness and stiffness between substrates.

2.1.3 Marker deformation on polysiloxane

In order to gain more quantitative data on cellular forces, a method was developed in which wrinkling is avoided and latex beads are embedded into the top surface of a polysiloxane membrane to visually track the deformations in the substrate (Figure 3A).[35] Specifically, latex beads were brushed into the liquid surface of polysiloxane and then a glow discharge device was used to form a crosslinked membrane that encapsulated the beads. Beads in an undeformed, zero-displacement state (before cellular deformation) were imaged as a reference image (Figure 3B). Keratocytes then migrated into an area and displaced the beads. Bead displacement was calculated by comparing an image of displaced beads to the reference image of the zero-displacement state (Figure 3C-D). Using this technique, it was observed that the largest forces occurred at the marginal edges of the cell, not at the extended front edge.[35–37] In addition, this technique facilitated the first quantitative data of the magnitude (length of arrow) and direction (orientation of arrow) of cellular forces.[35–38]

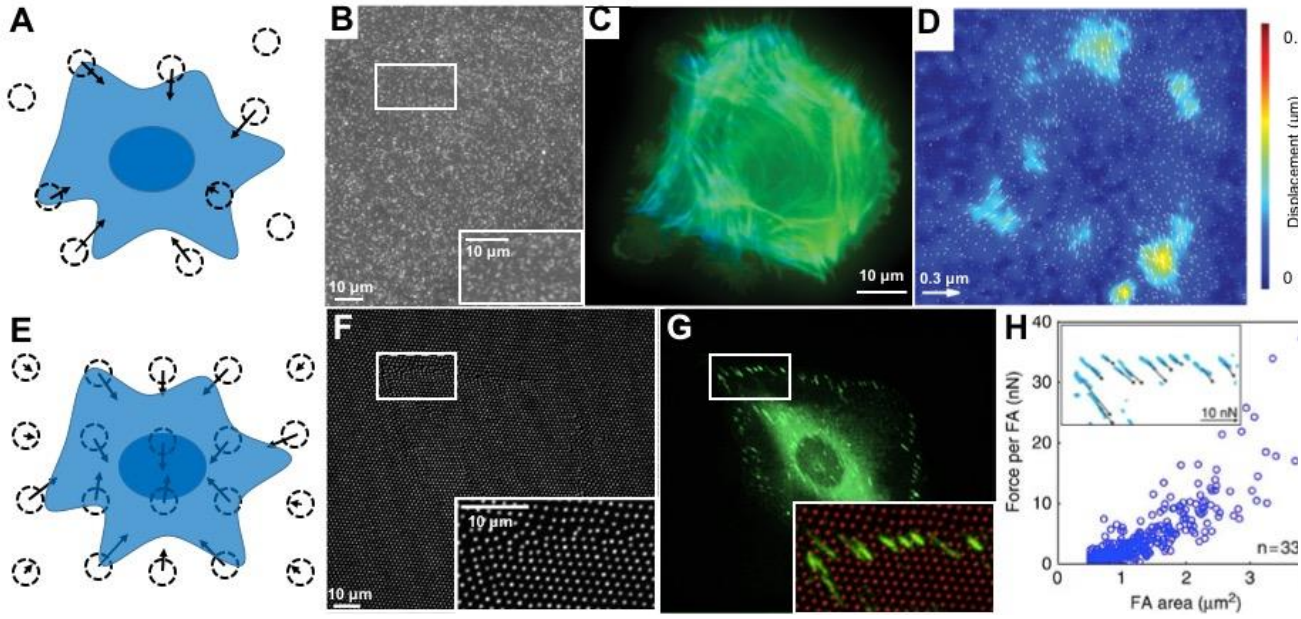

Figure 3 – Cellular forces can be measured by the displacement of markers embedded in a deformable material. (A) Surface displacements can be calculated from the movement of beads randomly embedded in the material. Dotted circles indicate the bead location after cellular displacement and the arrows indicate the magnitude and direction of their displacement. (B-D) Fluorescent microscopy allows for the analysis of bead displacements (white dots in B) and spatially arrangement of actin filaments (green and blue in C, where blue is the actin closer to the surface). Bead displacement vectors can be calculated (arrows in D) and overlaid on a colormap to visualize areas of large displacements (colors in D, units of colormap are μm.). (E) Beads can also be placed in a non-random orthogonal or hexagonal pattern. (F-H) Fluorescent microscopy allows for imaging the displaced position of the bead (white dots in F and red dots in the inset in G) along with fluorescent microscopy of their focal adhesions (FA) by paxillin (green in G) to examine the relationship between FA area and cellular forces (graph in H, inset in H shows zoom region of FAs with force vectors indicated location, direction, and magnitude). B-D are adapted from [38] and F-H are adapted from [40]. This figure was published in [94].

2.1.4 Reference-free traction force microscopy

To avoid the challenge of taking an image of the substrate in its undeformed, zero-displacement state as a reference image, a pattern of beads or markers have been used for reference-free traction force microscopy[39] (Figure 3E). Because this method involves the elimination of the reference image, it is termed "reference-free." Rather than generating randomly spaced markers, reference-free traction force microscopy involves creating an orthogonal or hexagonal pattern of beads or visual markers and measuring their displacement from the grid. The pattern reduces the technical challenge of documenting the zero-displacement location of the markers by either 1) imaging the substrate before adding cells or 2) removing cells and re-imaging. This method was used to understand the relationship of focal adhesion size and force generation (Figure 3F-H).[39,40]

2.1.5 Alternative traction force materials: polyacrylamide, native ECM, and engineered gels

After over a decade and a half since the first seminal work using polysiloxane, a new material was advanced to measure cellular forces: polyacrylamide gels.[41,42] Polyacrylamide is a hydrogel polymer composed of acrylamide (-$CH_2CHCONH_2$-) units. The authors of this work chose it because it is elastic over a wide range of cellular forces and its stiffness can be tailored by changing the amount of cross-linker (bis-acrylamide). Similar to polysiloxane, polyacrylamide has optical qualities that permit optical and immunofluorescent microscopy and its surface can be coated with one or more types of ECM proteins to permit cellular adhesion.[42]

Early studies with polyacrylamide found that the stiffness of a substrate can cause a mechanotransduction response in cells that affects the extent to which they are able to spread, how fast they can migrate, and their ability to form focal adhesions that are strong and stable.[41] Initially, non-fluorescent latex beads were embedded into the polyacrylamide gels and used to measure cellular forces[42], and later fluorescent beads were used.[43] Reference-free traction force microscopy, which overcomes the computational challenge of imaging twice and back calculating deformation, was first conducted on polysiloxane[39] and can also be employed on polyacrylamide.[44] In addition to patterning latex markers, adhesion molecules on the surface can be controlled by patterning extracellular matrix proteins to simultaneously measure cellular forces while also characterizing the effect of adhesion molecules on cellular forces.[45,46] To increase throughput, markers can be spaced such that the cell binds to a location over two markers, pulling them together, and simplifying the analysis to increase throughput.[47] Ultimately, polyacrylamide deformation for traction force microscopy has been used for a variety of applications and for a variety of cell types[48–58] and many would agree that it is currently the most widely used traction force microscopy method.

Since cells live in a 3D environment *in vivo*, there is a strong interest in the use of deformable materials that can be used for measuring cellular forces and within which cells can be cultured. Materials derived from native ECM such as collagen can be used to make a hydrogel. Unlike polysiloxane or polyacrylamide, these native ECM gels permit the diffusion of gas and nutrients for cell survival. For example, epithelial

cells and tissues were embedded in type I collagen with fluorescent markers.[59] Cellular forces were inferred from bead displacement to find that single cells generate tension (pulling) in 3D and that multicellular tissues can cause compression (pushing).[59] Additionally, biopolymer gels composed of collagen, fibrin, or matrigel were used to measure cellular forces in 3D and to show that breast carcinoma cells generate constant force during exposure to varying collagen concentrations and matrix stiffnesses.[60] This somewhat contradicts findings on 2D platforms in which stiffer substrates induced more cell spreading and more mature (spread and organized) focal adhesions.[61,62]

While ECM proteins provide a physiologically relevant environment to cells, they often behave in a non-elastic manner, making them mechanically complex. Additionally, seeded cells may degrade, synthesize, and/or remodel native proteins, leading to unclear interpretations about how material deformation relates to cellular force. To avoid these complications, engineered synthetic gels were created that are mechanically stable (mechanical properties are minimally by cells) but that also promote cell adhesion. As an example, a polyethylene glycol (PEG)-based hydrogel with proteolytically degradable domains and adhesive domains to facilitate cell invasion and spreading was used to measure cellular forces in 3D.[63] This showed that cells in 3D probe the extracellular environment with long, slender cellular extensions that produce large tractions.[63] Using a similar PEG hydrogel functionalized with arginine-glycine-aspartic acid-serine (RGDS)[64], cellular force measurements were conducted where cells are seeded on top of a substrate (such that the cell is in a 2D, not fully encapsulated environment) and displacement of markers is measured in 3D (to reveal 3D cellular forces); this is referred to as 2.5D.[65] This revealed out-of-plane forces at the focal adhesions, which have not been observed in 2D measurements.[65]

2.1.6 Deformable structures to measure cell forces: microposts or nanoposts

A deformable material can be used to craft a deformable structure, commonly shaped as a beam or cantilever. When a cell applies a force on the structure, it causes the structure to bend or deflect, which results in a visible displacement at the point where the force is applied. According to Hooke's law, the displacement (δ) can be used to measure the amount of force (F) by

$$F = k\,\delta \qquad \text{(Equation 1)}$$

where the spring constant (k) of the structure is empirically tested or mathematically determined by the geometry of the structure and the modulus of elasticity of its material. Deformable structures have been constructed with a range of different shapes and size in order to suit a particular application or type of cell; these devices include posts, silicon cantilevers, tissue posts, and fibrous matrices.[66]

Microposts are an array of cantilevers made from polydimethylsiloxane (PDMS) that can be used to measure cellular forces by quantifying their deflections (Figure 4A).[67] Based on the close spacing between the posts, a cell can spread out and attach to the tips of multiple posts, allowing one to measure its forces at several locations simultaneously since microposts are able to deflect independently from their neighbors.[68] Based upon the amount of deflection at the tip of a micropost and its direction, one can calculate the force generated by a cell using Hooke's law (Equation 1), where the spring constant is $k = 3\pi E d^4/64L^3$, E is the modulus of elasticity of PDMS, d is the diameter, and L is the length of the post (Figure 4B). Notably, this method is a direct calculation of force and overcomes some of the mathematical challenges associated with measuring forces using traction force microscopy.[69,70]

Microposts are manufactured using photolithography to build a master structure and soft lithography to produce the final structures in PDMS (Figure 4C). Multiple PDMS substrates can be generated from the same master with sequential casting of negative PDMS molds, which ensures that the dimensions of the microposts are similar between experiments (Figure 4D). Alternatively, PDMS microposts can be created by directly casting from a silicon master that has holes instead of posts.[71] After casting, the spring constant of the microposts can be estimated by the length and diameter of the final structures and the modulus of elasticity of PDMS.[72,73] Calibrating the spring constant can also be determined empirically, e.g. using atomic force microscopy (AFM), but often these direct measurements are difficult to perform due to the size and scale of the microposts.[73]

To quantify cell forces, one typically confines the adhesion of the cells to the tips of the microposts. Arrays of microposts are prepared for cell seeding by stamping fibronectin or another ECM protein on the tips of the posts to support the formation of focal adhesions. The sides of each post are typically treated with Pluronic F-127 to prevent protein adsorption and thereby limit adhesion. Depending on the application, alternative techniques have been used to encourage cell adhesion, such as gold-tipped microposts[74] or sacrificial layers.[75] Using optical or fluorescence microscopy approaches, the deflection of the micropost can be recorded for fixed and stained samples (Figure 4E) or with live-cell imaging (Figure 5A). Image analysis routines are used to track the distance between the centroid of each micropost and its undeflected position (Figure 5B) in order to determine its deflection (Figure 5C).[71] In this manner, it is possible to measure the magnitude and direction of the force at each post by equation 1 for a single image (Figure 4E) or a series of images taken over time (Figure 5D).[76]

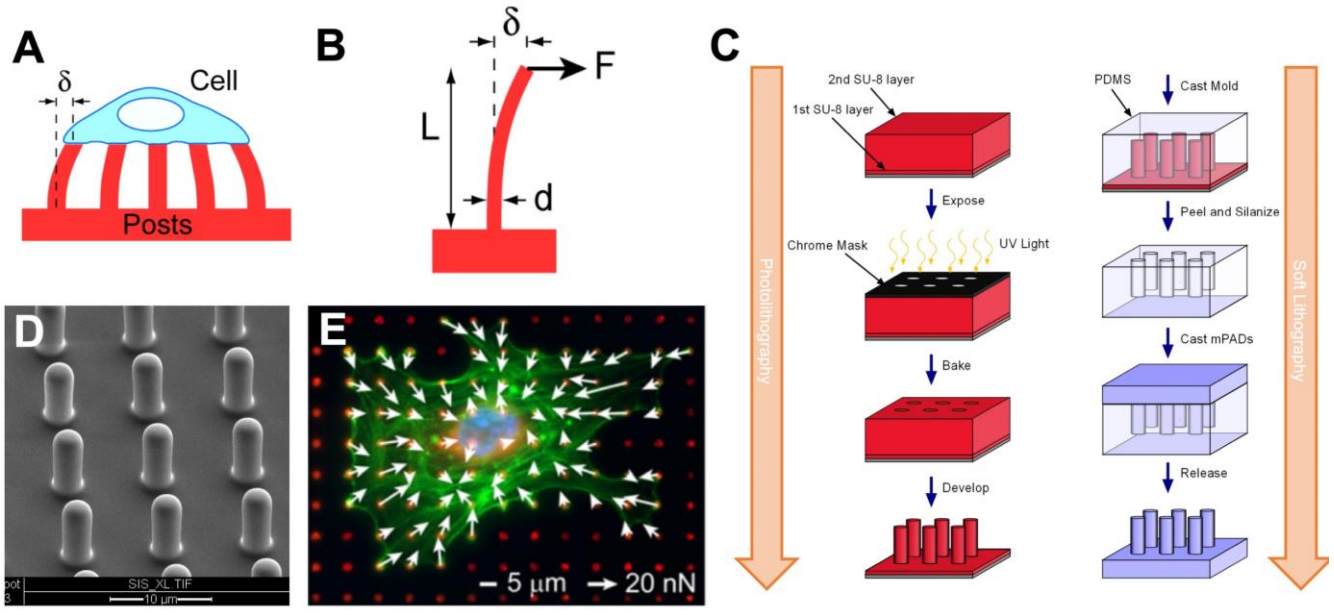

Figure 4 – Cellular forces can be measured by the deflection of posts.
(A) Cells deflect the microposts as they contract and the amount of force can be calculated from the deflection of the posts (δ). (B) Each post is a cantilever beam of length (*L*) and diameter (*d*) that deflects in proportion to the force applied at its tip (*F*). (C) Using photolithography techniques, a master structure of the microposts is made using SU-8 photoresist on a silicon wafer by exposing it to UV light through a chrome mask, baking it to crosslink the SU-8, and then using a solvent to develop the final master structure by removing the unexposed SU-8. Next, soft lithography techniques are used create a negative mold of the microposts by casting them in PDMS, then fluorosilanizing the mold and using it to cast the final PDMS structure. (D) An array of PDMS microposts imaged by scanning electron microscopy. (E) Cellular forces are measured by quantifying the defection of the posts which have been labeled with a fluorescent dye (red). White arrows indicate direction and magnitude of the forces, green is F-actin staining, and blue marks the nucleus. C is adapted with permission from [141]. This figure was published in [94].

Nanoposts are smaller versions of microposts; they allow for higher spatial resolution of cell forces because there are more posts under each cell. However, fabrication of posts at a nanoscale level has its challenges, such as surface cracking on negative molds[77].

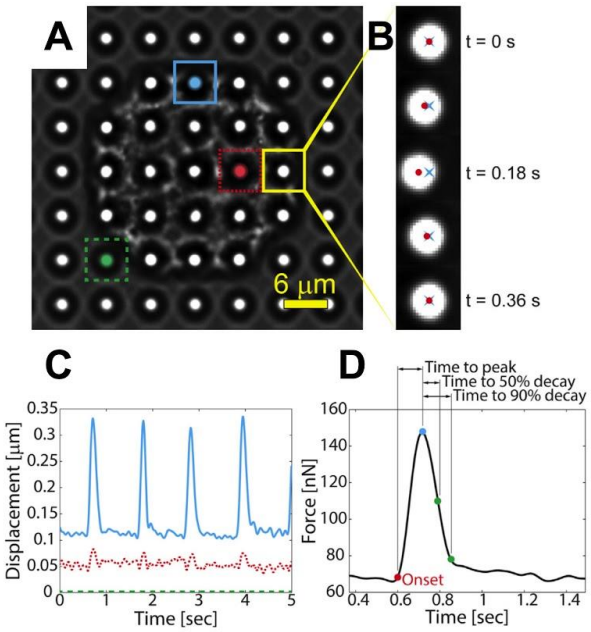

Figure 5 – Quantification of cellular forces by tracking the displacement of microposts.
Quantification of cellular forces by tracking the displacement of the microposts. (A) A single cardiomyocyte is shown on microposts. (B) The displacement of a post is tracked over time by determining the distance from the centroid of the tip of the post (red dot) to its undeflected position (blue "x"). (C) The dynamics if a cell's contractile forces can be monitored as shown by the displacement vs. time and (D) force vs. time graphs. Posts near the boundary of the cell (blue) tend to deflect more than posts near the center of the cell (red), while posts where the cell is not attached do not deflect (green). Reproduced with permission.[142] This figure was published in [94].

2.1.7 Deformable structures to measure cell forces: silicon cantilevers

Microelectromechanical systems (MEMS) are microscale devices composed of electrical and mechanical elements that include sensors and/or actuators.[78] They consist typically of structures made from crystalline silicon material due to its advantageous mechanical properties[79,80] and its compatibility with micromachining techniques that can deposit, pattern, or etch this material with nanoscale precision.[81] MEMS was used as one of the first approaches to measure cellular forces with a deformable structure.[82] Specifically, a device was fabricated with a multitude of cantilevers on a silicon wafer. Each cantilever was horizontal in orientation and was contained within its own cavity underneath the surface of the wafer, but with the tip of the cantilever extending out to the surface through an opening. As a cell crawled across the

surface of the device, it made contact with the tip of the cantilever and displaced it, which was measured optically.[82] In this manner, it was found that migrating cells not only generate forces at their leading edge, but have substantially larger, retrograde forces at their trailing edge. MEMS devices have also measured cell forces in embryonic *Drosophia* axons by measuring deflection of cantilevers optically relative to a fixed reference beam.[83] This MEMS device is a series of flexible silicon beams attached to a rigid probe which can be inserted into a biological environment to simultaneously exert forces and measure biological response. Using this system, it was observed that after release of externally applied tension to the *Drosophia* neurons, the cells contracted and generated forces to restore tension, demonstrating an influence of mechanical tension to neuronal behavior.[83]

Atomic force microscopy (AFM) is a versatile experimental technique used to push and pull on molecules, cells, tissues, or other materials on the nanoscale. Cantilever deflection is measured from laser deflection onto a photosensitive detector. Similar to aforementioned deformable structures, force is calculated from deflection, the cantilever dimensions, and the known stiffness of the cantilever. On the cellular scale, AFM can be used to measure mechanics such as cell stiffness or cellular response to force by pushing on the cell with an AFM cantilever.[84–86] More similar to aforementioned measurements examining forces exerted by cells (as opposed to externally exerting forces on cells), it is also possible to adhere cells between a surface and an AFM cantilever and measure cell contraction (the cell pulling the cantilever toward the surface).[87] In a system with an AFM combined with a “side-view” microscope, contraction of human bone osteosarcoma epithelial single cells was examined. It was observed that cells contract laterally at the midpoint before contracting vertically, suggesting directional cytoskeletal remodeling or contraction.[87] AFM cantilevers are often composed of silicon, usually silicon or silicon nitride. Similar to MEMS, these materials are used because they are mechanically well-characterized and structures with micron dimensional tolerances can be created using micromachining.[88] After being machined from silicon, cantilevers are often coated with thin metal layers such as gold for the purposes of functionalization and/or increased reflectance for deflection measurements.[89,90] A similar AFM method was used to measure mechanics and contraction

dynamics of individual platelets. This work found that platelets contract immediately after binding to fibrinogen and complete contraction within 15 minutes, generating higher forces in stiffer microenvironments.[91] While this technique is challenging in throughput (one cell measured at a time) and cost (both the high cost of the AFM and the disposable cantilevers), it is capable of providing cell contraction forces temporarily and cell adhesion forces with simultaneous cell visualization in a variety of microenvironments.

2.1.8 Summary and future outlook on the measurement of single-cell forces

Cellular forces can be measured using deformable materials and deformable structures. Through all these techniques, deformation (material or structural) is measured and used to calculate force from the known properties such as material stiffness and/or structural dimensions. Over the last three decades, approaches to measure cellular forces have been invented and improved, facilitating characterization of the strength of cellular forces directionally and temporarily during cell processes such as migration or maturation, in healthy or diseased states, and in the presence or absence of key cellular markers or external stimuli. Using different approaches to measure force and a wide variety of cell types can help to elucidate the common features in cell mechanics and increase our confidence in establishing robust biomechanical relationships for cells. For example, the effect of stiffness on cellular force generation has been examined by measuring bead displacement on multiple materials[38,41] as well as on structures.[67] Additionally, the observation that cellular forces increase as function of focal adhesion size has been corroborated with multiple methods.[39,40,67] While each method has its strengths and drawbacks, collectively these methods work symbiotically to elucidate biophysical relationships and increase confidence that these relationships are not an artifact of the observation method.

Despite the improvement in these techniques and the vast knowledge gained from them, some challenges prevent accessibility of these techniques to all fields and research groups. Material wrinkling, the earliest method to characterize cell forces, facilitated the first method to comparison of cell forces but are ultimately non-quantitative.[29,30] Later methods facilitated quantification and the first force maps indicating cell force

magnitude and direction[35,36] but are challenging and time-consuming because they require cell removal to obtain a reference image. Others do not require a reference image, but the manufacturing of each substrate requires clean room preparation[39] or individual printing of each reference point.[40] Ultimately this means that each technique has one or more challenges including high cost (particularly start-up cost), manufacturing complexity or difficulty, imaging temporal limitations, quantification or computational analysis challenges, and/or throughput. Traction force microscopy methods can also be confounded by other variables; for example, substrate topography and microenvironmental stiffness that affect cell function.

Looking to the future, an ideal system may increase throughput and decrease technical challenges involved in system manufacturing, data collection, and/or data analysis. This system may involve techniques in which system manufacturing is less expensive, increased throughput (i.e. more cells measured per unit or reduced manufacturing time per unit), and/or requires only widely available, inexpensive equipment. It would also be desirable to use simple image acquisition approaches to capture material or structural deformation and fast computational tools to measure cellular forces with accuracy. Additionally, a system should be versatile to a variety of cell types (varied sizes, strengths, functions) and compatible with other cellular assays, i.e. immunofluorescence microscopy, RNA-seq, etc., to understand how cell mechanics relates to cell function. Finally, an ideal system could both measure cellular forces and not inadvertently affect their behavior, unless by intention, in order to facilitate our understanding of mechanobiology.

2.2 Platelets and the measurement of their force generation

2.2.1 Introduction: platelets and the role of their force generation

Platelets are blood cells responsible for forming a hemostatic plug to stop bleeding. Upon vascular injury, subendothelial collagen is exposed and von Willebrand Factor (VWF), a blood glycoprotein, binds to the exposed collagen. Platelets bind to VWF through platelet glycoprotein Ib (GPIb) binding to the VWF A1

domain as well as via platelet integrin $\alpha_{IIb}\beta_3$ binding to RGD (Arg-Gly-Asp) on the VWF C1 domain. Platelets ultimately bind, spread, and contract for the secession of bleeding and reestablishment of blood flow.

2.2.2 Measurement of single platelet forces

Single-platelet forces were first measured by Lam et al. 2010 using atomic force microscopy by seeding platelets between a fibrinogen-coated AFM cantilever and a fibrinogen-coated surface[91]. Platelets rapidly contracted over 4 minutes, until reaching and maintaining a maximum contraction force around 10-15 minutes. The maximum force per platelet reached ranged from 1.5 to 79 nN of force, with an average maximum force per platelet of 19 nN. Additionally, platelets on a stiffer cantilever produced more force than platelets on a softer cantilever. This trailblazing platelet study provided the first measurement of platelet forces. However, to our knowledge, measuring platelet forces with an AFM has not be repeated by the authors of this work or by others, likely due to the high cost and low yield of AFM. These limitations led to only 1-4 platelets measured per donor and 30 platelets total included in this study[91].

Traction force microscopy has also been modified for the small size of platelets and applied to measure single platelet forces[3,6,7]. This was first conducted by Henriques et al. 2012 who embedded fluorescent beads into a fibrinogen-coated polyacrylamide gel and imaged over time, providing the first subcellular spatial data of platelet forces[6]. After measuring the forces of 14 platelets, Henriques et al. found that platelet area correlates with platelet force and that platelets produce the highest forces at the cell periphery contracting toward the center of the cell[6]. Follow-up studies from the same lab, including Hanke & Probst et al. 2018[7] and Hanke et al. 2019[3] found that platelets have unique force time behaviors: plateau (increase to maximum force and hold steady), relaxing (increase to maximum force, then decrease), and oscillating (increase and decrease repeatedly). In contradiction to Lam et al. 2010[91], Hanke & Probst et al. 2018 found that platelet force is stiffness independent. Notably, Hanke & Probst et al. 2018 included approximately 20-30 platelets per condition and 225 conditions total, which is an order of magnitude more cells than the initial platelet TFM work by Henriques et al. 2016. Finally, Hanke et al. 2019[3] conducted TFM on platelets

under flow and found that the platelet contraction angle is dependent on flow rate wherein platelets contract perpendicular to the direction of flow at higher flow rates[3].

Feghhi et al. 2016 used VWF-treated nanoposts to measure platelet forces and found that GPIb transmits cytoskeletal force and that blocking GPIb or blocking VWF A1 reduces platelet force by 20%. Additionally, blocking $\alpha_{IIb}\beta_3$ reduces platelet force by 50%. Notably, this work was the first to measure single-platelet forces on posts and it measured forces of an order of magnitude more platelets than what had been previously reported at the time including 7-20 platelets per donor, 74-103 platelets per condition, and 336 total platelets in the study.

Reference-free TFM on platelets was first conducted by Myers et al. 2017 in which platelets bind between two dots of fluorescent fibrinogen patterned onto a polyacrylamide surface[2]. Myers et al. 2017 finds that thrombin concentration and substrate stiffness synergistically increase platelet force and that blocking ROCK attenuates the stiffness response. Additionally, platelets from donors with Wiskott-Aldrich syndrome and May-Hegglin disorder have significantly less force than healthy controls and some patients with bleeding diatheses (that have normal results for all clinically available bleeding tests) show significantly lower single platelet forces and are missing a subpopulation of highly contractile platelets[2]. Using the same technique, Oshinowo et al. 2021[8] measures single-platelet forces of humans, mice, pigs, sheep, and dogs and finds that mice and pigs produce significantly less force per platelet than humans while dogs produce significantly more force per platelet. In binding between two dots, this reference-free technique directs platelet size and shape while greatly increases yield to measure 84-88 platelets per donor and 818-2888 platelets per study.

Ultimately, measurement of single platelet forces has methodologically improved and revealed key information about spatial and temporal platelet force generation, mechanical and chemical cues that alter force generation magnitude and direction, receptors and signaling pathways involved in force transmission,

and force generation in platelets of healthy humans, humans with bleeding disorders, and non-human species. These studies are summarized in more detail in Table 1.

Table 1 – Review of platelet single-cell force studies.
A summary of papers that measure single platelet forces including the study (lead author(s), year, and citation), methodology, forces observed per platelet (mean, standard deviation (SD), and range observed), major findings, and the number of platelets measured (per condition, per donor in each condition, and total). Asterisks (*) indicates that values were approximated from manuscript figures or tables because exact values were not reported.

Study	Methodology	Force per platelet	Major findings	Number of platelets measured
Lam et al. 2010[91]	Atomic force microscopy using 12 kPa or 29 kPa cantilevers treated with fibrinogen and a fibrinogen-coated glass surface	Mean ± SD: 19 ± 18 nN Range: 1.5 – 79 nN	• Rapid contraction over 4 minutes, increased contraction until reaching a steady state around 10-15 mins. • Stiffer cantilevers result in more maximum force per platelet. 12 kPa = *8 nN, 29 kPa = *15 nN, infinite stiffness (isometric clamp) = *20 nN. • Elasticity of contracted platelet is 9.85 kPa. Adhesion force of platelet is 69 nN.	Per condition: 30 Per donor: 1-4 Total: 30
Henriques et al. 2012[6]	Traction force microscopy using a fibrinogen-coated polyacrylamide gel (4 kPa) with embedded fluorescent beads	Mean ± SD*: 34 ± 21 nN Range*: 12-78 nN	• Contraction over 25 minutes, until reaching a steady state • Forces are nearly isotropic and are strongest at the platelet edge, pointing inward to the center of the cell. • Platelet area correlates with maximum platelet force.	Per condition: 14 Per donor: unknown Total: 14
Feghhi et al. 2016[5]	Nanoposts made of PDMS with a VWF-coating (15.7 kPa due to fabrication from 3.2 MPa PDMS and dimensions of posts: 850 nm diameter, 3.5 μm height, and 2 μm spacing)	Mean ± SD*: 49 ± 34 nN Range: unknown	• GPIb transmits cytoskeletal force; blocking GPIb or blocking A1 reduces platelet force by 20%, blocking $\alpha_{IIb}\beta_3$ reduces platelet force by 50% • The binding interaction between GPIb and Filamin A is involved in force generation.	Per condition: 74-103 Per donor: 7-20 Total: 336
Myers et al. 2017[2]	Reference-free traction force microscopy in which platelets bind between two fibrinogen dots microcontact-printed onto a polyacrylamide gel (25-100 kPa)	Mean ± SD*: 38 ± 20 nN Range*: 0-120 nN	• Thrombin concentration and substrate stiffness synergistically increase platelet forces. • Rho/ROCK, but not MLCK, signaling is important in mechanosensing; when ROCK is blocked with Y27623, stiffness response is attenuated. • Some patients with bleeding diatheses that have normal results for all clinically available bleeding tests show significantly lower single platelet forces and are missing a subpopulation of highly contractile platelets. Platelets from donors with Wiskott-Aldrich syndrome and May-Hegglin disorder have significantly less force than healthy controls.	Per condition: 31-368 Per donor: ~84 Total: 818
Hanke & Probst et al. 2018[7]	Traction force microscopy similar to Henriques et al. 2012 except on 19-83 kPa	Mean* ± SD*: 150 ± 90 nN Range*:	• Platelets have three unique force-time behaviors: plateau, relaxing, and oscillating. • Platelet force correlates with spread area and is stiffness independent.	Per condition*: 20-30 Per donor:

	gels.	25-600 nN	• Maximum platelet area is reached in 10 minutes, maximum platelet force is reached after 30 minutes. • Force is exerted slightly anisotropically.	unknown Total*: 225
Hanke et al. 2019[3]	Traction force microscopy similar to Henriques et al. 2012 and Hanke & Probst et al. 2018 except measurement occurs under flow comparable to larger human veins (0, 300, 400, and 700 μL/hour) and on 41 kPa gels.	Mean* ± SD*: 150 ± 90 nN Range*: 60-500 nN	• Magnitude of force and dipole ratio (degree of anisotropy) is flow rate independent. • Angle between flow and contraction varies with flow rate; platelets contract perpendicular to the direction of flow at higher flow rates.	Per condition: 22 Per donor: unknown Total: 88
Oshinowo et al. 2021[8]	Reference-free traction force microscopy similar to Myers et al. 2018 except on 75 kPa gels	Mean* ± SD*: 39 ± 20 nN Range*: 0-100 nN	• Compared to human single platelets, mice and pigs produce significantly less force per platelet while dogs produce significantly more force per platelet. Sheep platelets do not produce statistically different forces than human platelets. • Compared to human platelets, normalized platelet area is significantly higher in sheep platelets on fibrinogen and collagen. Dog platelets normalized spread is significantly less on collagen. • Compared to humans, pig platelets bind significantly more to collagen. • Contraction volume is not significantly different for any species.	Per condition: 245-763 Per donor: ~88 Total: 2888

Chapter III: Black Dots To Measure Single Platelet Forces and Investigate Heterogeneity of Platelet Forces

3.1 Introduction

Cells use forces to migrate, contract, and probe their physical environment[22,92]. These forces arise from interactions of cytoskeletal proteins, which transmit cellular forces to the extracellular matrix. The cellular forces can ultimately cause deformation of the surrounding environment. By measuring the deformation of the underlying substrate, cellular forces can be estimated. This principle has been used to develop techniques such as membrane wrinkling, traction force microscopy, and microposts, among many others to measure single-cell forces[55,85,93,94]. However, existing methods have several drawbacks including the limited number of cells that can be measured per experiment or inadvertent impact on cell functions by strictly constraining cell size and shape.

Traction force microscopy (TFM) is one of the most widely used techniques for measuring forces from single cells. In TFM, cellular forces are determined from the displacement of fluorescent particles embedded within a flexible substrate[95–97]. Often, a pair or series of images are required to track a cell's forces: a reference image of the undeformed substrate and one or more images of the displacements caused by the cells. For this reason, TFM is a relatively low-yield assay and is incompatible with immunofluorescent staining. To side-step the requirement of multiple images, reference-free TFM approaches have been developed where markers are fabricated on a substrate in a pattern instead of being distributed randomly[40]. Since only a single image is required for the measurement of traction forces, reference-free TFM is compatible with fixed samples and immunofluorescent staining because the cells do not need to be detached. While reference-free TFM can increase the number of cells that can be efficiently analyzed, many of the existing methods provide a large degree of constraint on the adhesion and spreading of a cell, impacting their physiological significance[44,47,98,99].

Platelets use their traction forces to adhere and form a hemostatic plug that stops bleeding[100–102]. During this process, the actin cytoskeleton of a platelet drives its shape change, spreading, and production of traction forces. Measuring these forces for individual platelets is challenging due to their small size (2-5 μm in diameter)[103], their ability to produce strong forces[6], and their sensitivity to collection and handling techniques[104]. It has been shown that the spread area of platelets correlated with the overall magnitude of their traction forces[7,105]. While time-dependent changes in platelet shape and cytoskeletal structure have also been observed[19,20], it is not known how these factors impact traction forces in platelets. Moreover, these factors may be interrelated because the actin cytoskeleton underlies changes in shape and spreading. Previous measurements of platelet forces have used atomic force microscopy[91], classical TFM[6,7,105], reference-free TFM[47], and nanoposts[5] to elucidate properties of single platelets such as their temporal and directional contraction dynamics, the function of platelet mechanoreceptors, and the influence of biochemical and mechanical cues on platelet contraction. While these existing methods have allowed for understanding of important biophysical properties of platelets, they have been hampered by constraints on the shape or spreading of platelets and/or their low yield, often analyzing fewer than thirty platelets per condition.

Here, we present a microcontact-printed, reference-free TFM technique for measuring single-cell forces without constraining cell shape and size. Our method relies on microcontact printing to deposit a grid of fluorescently labeled bovine serum albumin (BSA) onto a flexible polydimethylsiloxane (PDMS) substrate. This procedure results in a fluorescent surface with a pattern of circular islands that are non-fluorescent (Figure 6A), hence the technique is termed ‘black dots.’ The black dots technique offers several advantages over existing methods for measuring single-cell forces: 1) it is high-yield due to the ability to measure force with a single image, 2) it is compatible with immunofluorescent staining so that traction forces can be measured alongside analysis of structure and/or localization, and 3) it does not constrain cell shape and size due to the substrate containing a contiguous adhesive protein. With this approach, we characterized forces, cytoskeletal structures, and geometric properties of more than five hundred human

platelets for linear mixed-effects modeling and K-means clustering, from which we identified that platelet size, shape, and cytoskeletal structure have both independent and cooperative contributions to platelet force.

3.2 Materials and Methods

3.2.1 Microfabrication of patterned stamp

First, a silicon master mold with an array of vertical pillars was created with the desired pattern size by photolithography as described previously[5]. Briefly, photoresist was spun onto a silicon wafer and an e-beam lithography system was used to pattern circles of the desired diameter and center-to-center spacing. The photoresist was then developed and etched to create a master containing an array of vertical silicon pillars. For cells as small as platelets, we used a pattern with a diameter of 850 nm and center-to-center spacing of 2 μm, and the final etched pattern had a height of 3.5 μm. Larger cell types are amenable to larger pattern sizes which can be easier to image.

To generate the stamps for patterning the fluorescent protein, PDMS (Sylgard 184, Dow Corning) at a 10:1 base to curing agent ratio is poured onto the master mold and cured in a 110 °C oven for 20 minutes. The cured PDMS is peeled from the master mold, revealing a negative version of the original pattern: a grid of holes instead of pillars. Edges of the stamp were trimmed with sharp razors and stored in enclosed petri dishes prior to use.

3.2.2 Sacrificial PVA film production

Poly(vinyl alcohol) (PVA) films for transferring the fluorescent pattern were made following previously described protocols with some modifications[106,107]. A mixture of 0.55 g PVA powder (Sigma) was mixed with 15 mL DI water and heated for 30 minutes at 110 °C until the powder fully dissolved. A standard 10 cm Petri dish was plasma treated for 10 seconds to help the final film remain attached to the dish. After cooling down to room temperature, the liquid PVA mixture was poured into the plasma-treated dish. The dish was left uncovered in a 65 °C oven overnight to allow the liquid to completely evaporate. The next

day, the dish was removed from the oven revealing a thin, dried PVA film loosely attached to the bottom of the Petri dish. The film was cut into appropriate sized pieces and used as needed, or the dish was covered and sealed with parafilm for longer term storage.

3.2.3 Flexible PDMS substrate preparation

Flexible 13.5 kPa substrates were manufactured as previously published[108,109]. Soft PDMS (Sylgard 527, 1:1 ratio of parts A and B, Dow Corning) and normal PDMS (Sylgard 184, 10:1 ratio of base to curing agent) were first prepared separately and allowed to degas for at least 20 minutes under vacuum. The two types of PDMS were then mixed to form a mixture of 5% Sylgard 184 and 95% Sylgard 527 by weight, and the mixture was degassed for 20 minutes under vacuum. Round glass coverslips (25 mm diameter, #1 thickness, VWR) were plasma treated for 30 seconds (Plasma Prep II, SPI Supplies) and a 100-130 µL droplet of the PDMS mixture was placed onto each of the plasma-treated glass coverslips. The PDMS droplets were allowed to spread across the glass coverslips on a level countertop for at least 30 minutes, resulting in a PDMS layer that is approximately 250 µm in height. The PDMS-coated coverslips were degassed for 30 minutes before transferring to a 65 °C oven overnight to cure. The following day, the PDMS substrates were removed from the oven and cooled at room temperature. To extract unpolymerized monomers, the PDMS substrates were submerged in 100% ethanol for at least 3 hours, followed by multiple rinses with DI water before drying in a 65 °C oven overnight.

3.2.4 Microcontact printing and functionalization of black dots

The patterned PDMS stamps and PVA film were used to deposit a layer of fluorescent protein onto the flexible PDMS substrates similar to previously published techniques[108,109] (Figure 6B). All steps were performed at room temperature and preferably in a standard tissue culture hood. First, Alexa-Fluor 488, 594, or 647-conjugated-BSA (5 mg/mL, Life Technologies) was diluted 1:2000 in PBS (1X without calcium or magnesium, Life Technologies), and a 400 µL droplet was gently placed onto a patterned stamp (about 1 cm^2 area) within a petri dish. The droplet was left on the stamp for 30 minutes to allow the fluorescent BSA to adsorb onto the surface. Fresh PBS was slowly added to the petri dish until the liquid level rose

above the stamp. The stamp was removed from the PBS and rinsed 3 times in fresh PBS dishes by gently submerging the stamp. After the final rinse, the stamp was dried with a gentle stream of nitrogen gas.

Next, the PVA film was used to transfer the fluorescent pattern from the stamp to the flexible substrate. A PVA film was trimmed to a size slightly larger than the stamp. The film was plasma treated for 60 seconds to facilitate protein transfer from the stamp. Using a pair of tweezers, the film was then lowered onto the dried stamp. The film was gently pressed onto the stamp using rounded-tip tweezers to remove any air gaps, and a thin piece of glass slide was placed on top of the film. A 50-gram weight was placed onto the glass slide to maintain close contact between the film and stamp. After 20 minutes, the weight and glass slide were removed and the PVA film was gently peeled from the stamp and transferred to the flexible PDMS substrate. Again, rounded-tip tweezers were used to gently press the film onto the substrate and remove any air gaps. The film was left on the flexible PDMS substrate for 20 minutes. The substrate was then submerged in PBS for up to 5 minutes, causing the film to rehydrate and float away from the surface where it can be discarded. The final substrate containing the pattern of fluorescent BSA, dubbed “black dots,” was stored in PBS overnight at 4 °C before cell seeding and can be stored for at least 1 week.

On the day of cell seeding, von Willebrand Factor (VWF) (Haematologic Technologies) was diluted in PBS to 5 µg/mL and was pipetted onto the black dots. To encourage droplet spreading over the black dot surface, a glass coverslip was gently placed on top of the droplet. The von Willebrand Factor was incubated for 1-1.5 hours at room temperature before the coverslip was removed. To block the surface, the substrate was then submerged in a 0.2% Pluronic F-127 (BASF) in PBS for 30 minutes. The substrate was finally submerged into PBS and stored until platelet seeding.

To quantify VWF adsorption onto the surface, black dots with and without VWF treatment were blocked with 10% goat serum (Life Technologies, diluted in PBS) for 1 hour and then incubated with a FITC-labeled anti-von Willebrand Factor antibody (Abcam, ab8822) for 1 hour). Substrates were mounted onto glass coverslips using Fluoromount-G mounting medium (Life Technologies) for confocal microscopy. Images

collected with the same settings were quantified using MATLAB to characterize FITC fluorescence (and therefore VWF adsorption) on the fluorescent BSA and the non-fluorescent black dots for substrates with and without VWF treatment.

3.2.5 Platelet isolation and seeding

Platelet-rich plasma (PRP) was collected from consenting research participants by plateletpheresis using the Trima Accel® automated collection system. Research participants were healthy and not taking any platelet inhibiting medications. Platelets were isolated from plasma by platelet centrifugation washing modified from previously described protocols[104]. Platelets were pelleted at 1000 g and resuspended in HEN Buffer, pH 6.5 containing 10 mM HEPES (Sigma), 1 mM EDTA (Corning), and 150 mM NaCl (Fisher Scientific) and supplemented with 0.5 µM prostacyclin (PGI_2) (Sigma). To prevent activation, platelets were incubated for 10 minutes at room-temperature and then repeat treated with 0.5 µM PGI_2 and pelleted via centrifugation at 800 g. Platelets were resuspended and diluted to $3{\cdot}10^8$ platelets/mL with modified Tyrode's buffer, pH 7.3 containing 5 mM HEPES (Sigma), 137 mM NaCl (Fisher Scientific), 5.5 mM glucose (Fisher Scientific), 12 mM $NaHCO_3$ (Sigma), 0.3 mM NaH_2PO_4 (Sigma), 2 mM KCl (JT Baker), 1 mM $MgCl_2$ (Sigma), and 2 mM $CaCl_2$ (Macron Fine Chemicals) and supplemented with 0.35% (w/v) human serum albumin and 0.02 U/mL apyrase.

Immediately before seeding the washed, isolated platelets onto the black dots, the platelets were further diluted to $2.5{\cdot}10^7$/mL in Tyrode's buffer, pH 7.5 containing 10 mM HEPES (Fisher Scientific), 138 mM NaCl (JT Baker), 5.5 mM glucose (ACROS Organics), 12 mM $NaHCO_3$ (Sigma), 0.36 mM NaH_2PO_4 (Sigma), 2.9 mM KCl (VWR), 0.4 mM $MgCl_2$ (Fisher Scientific), and 0.8 mM $CaCl_2$ (VWR International). After dilution, 10 million platelets were seeded onto each black dot substrate. To allow time for initial platelet binding onto the black dots, platelets were incubated at room-temperature for 10 minutes. To remove unattached platelets, black dots were then gently dipped in PBS and then immediately submerged in fresh Tyrode's buffer. To allow time for platelet adhesion and contraction on the black dots, the platelets were incubated for an additional 30 minutes at room-temperature. Incubation times were selected to reduce temporal

differences in platelet contraction by 1) preventing new platelet binding after 10 minutes, such that all platelets were on the surface for 30-40 minutes and 2) allowing platelet binding and contraction for 30 minutes so that platelets reach a maximum contraction[6,7,91].

3.2.6 Immunocytochemistry

Platelets were fixed with 4% paraformaldehyde for 20 minutes, permeabilized with 0.1% Triton X-100 for 10 minutes at room temperature, and blocked with 10% goat serum (Life Technologies, diluted in PBS) for 1 hour. Platelet F-actin was labeled with phalloidin 488 (Life Technologies), and platelet GPIb was labeled with a CD42b monoclonal antibody, clone SZ2 (Life Technologies) and a goat anti-mouse IgG secondary antibody (Life Technologies). Substrates were mounted onto glass coverslips using Fluoromount-G mounting medium (Life Technologies) for confocal microscopy.

3.2.7 Imaging and image analysis

Fixed and stained platelets were imaged on a Nikon A1R or a Leica SP8 confocal microscope with a 60x oil objective (NA = 1.4). Images of platelets were taken with a large enough field of view to ensure several black dots with no deformation surrounded each platelet.

To quantify the deformation of the black dots, we modified a previously existing method for tracking objects[110]. The fluorescent image of the black dots was first run through a spatial bandpass filter with a characteristic noise length scale of 1 pixel. The dots were identified with a peak finding algorithm using a peak threshold value of 0.15. For each dot, the centroid was then found to subpixel accuracy. To calculate the displacement of each dot, the zero-displacement state of the black dots must be determined. The dots in the image were organized into a rectangular array of rows and columns. For each row and column, a line was fit through four of the dots near the edges of the image. We assume that the dots near the edge of the image have little or no displacement and can therefore be used as reference for the highly displaced dots near the cell. The lines fit through the rows intersect with lines fit through the columns, and the

intersection points were used as the zero-displacement state. From here, the displacement of each dot was calculated by subtracting the zero-displacement position from the deformed position.

3.2.8 Force calculation

Traction forces are calculated from the surface displacements using regularized Fourier Transform Traction Cytometry (FTTC)[70,111]. FTTC requires a rectangular grid of displacements which is obtained trivially by our black dots pattern without any interpolation. Briefly, displacements (u) at points (r) are related to traction forces (t) at points (r') in the domain Ω by equation 2:

$$u(r) = \int G(r,r')t(r')d\Omega(\mathrm{r}) \qquad \text{(Equation 2)}$$

In equation 2, $G(r,r')$ are the simplified Boussinesq Green's functions defined in Equation 3. In this equation, E is the Young's modulus and ν is the Poisson's ratio of the substrate.

$$G(r,r') = \frac{(1+\nu)}{\pi E}\begin{bmatrix}(1-\nu)|r|^2 + \nu u_x^2 & \nu u_x u_y \\ \nu u_x u_y & (1-\nu)|r|^2 + \nu u_y^2\end{bmatrix} \qquad \text{(Equation 3)}$$

Equation 2 must be inverted to calculate traction forces (t) from measured displacements (u). A Fourier Transform can be applied to Equations 2 and 3 to make the inversion easier and resulting in Equation 4:

$$\tilde{t} = \tilde{G}^{-1}\tilde{u} \qquad \text{(Equation 4)}$$

A regularization scheme ($\tilde{H}$) was applied to account for noise and a regularization coefficient (λ) of $5 \cdot 10^{-8}$ was used, resulting in Equation 5:

$$\tilde{t} = (\tilde{G}^T\tilde{G} - \lambda^2\tilde{H})^{-1}\tilde{G}^T\tilde{u} \qquad \text{(Equation 5)}$$

To assess whole-cell contractility, we calculate the total force and net force for each cell. Total force is calculated by summing the force magnitudes from each dot underneath the cell. Net force is similarly calculated by simply adding the force vectors from each dot together; the cell is assumed to be in static

equilibrium, so the net force should tend towards 0. Because the cell can adhere to spaces between black dots, we consider all black dots within the cell boundary and within 1 dot spacing outside the cell boundary for these calculations.

3.2.9 Area and circularity calculations

The cell boundary and area were determined in MATLAB using a user-adjusted threshold and shape fill on the fluorescent F-actin image. We also tested determining the cell boundary using the GPIb fluorescent image and no difference in cell boundary was observed. Circularity was calculated from the cell boundary using: $C = 4\pi A/P^2$, where C is the circularity, A is the area, and P is the perimeter[112]. Circularity values can range from 0 to 1, where a value of 1 indicates a perfect circle.

3.2.10 F-actin dispersion calculation

A K-means clustering analysis was utilized to separate the data into clusters in an unbiased way. First, the area, circularity, and F-actin dispersion data were normalized. The built-in MATLAB function “kmeans” was used to cluster the data based on the area, circularity, and F-actin dispersion. Cell force was not included for purposes of clustering. To determine the optimal number of clusters, the built-in MATLAB function “evalclusters” was employed for up to 6 clusters using either Silhouette or Gap evaluation criteria with default settings. The optimal number of clusters is defined as the one with the highest Silhouette value or as the lowest number of clusters such that the mean Gap value for the next highest number of clusters falls within the standard error of the previous one. Silhouette and Gap values were evaluated for up to 6 clusters, and both criteria suggest that 2 clusters is optimal for our data set (Manuscript supplement, Figure 20).

3.2.11 K-means clustering

A K-means clustering analysis was utilized to separate the data into clusters in an unbiased way. First, the area, circularity, and F-actin dispersion data were normalized. The built-in MATLAB function “kmeans” was used to cluster the data based on the area, circularity, and F-actin dispersion. Cell force was not included

for purposes of clustering. To determine the optimal number of clusters, the built-in MATLAB function "evalclusters" was employed for up to 6 clusters using either Silhouette or Gap evaluation criteria with default settings. The optimal number of clusters is defined as the one with the highest Silhouette value or as the lowest number of clusters such that the mean Gap value for the next highest number of clusters falls within the standard error of the previous one. Silhouette and Gap values were evaluated for up to 6 clusters, and both criteria suggest that 2 clusters is optimal for our data set (Manuscript supplement, Figure 20).

3.2.12 Statistics

To compare donor to donor variability, a one-way ANOVA and Tukey's post hoc test was used to determine whether differences in the means between donors were statistically significantly significant.

To examine effects of area, circularity, and F-actin dispersion on force, each covariate was centered at its mean and circularity and F-actin dispersion were transformed to a 0-100 scale. This transformation does not affect the results. A multivariate mixed effects model with random donor effects was used to analyze the centered data and determine the influence of individual covariates and interactions between covariates.

To determine if forces of platelets in cluster 1 and cluster 2 (as determined by the K-means clustering analysis) were significantly different from each other, a student's t-test was used. For all tests, significance is considered $p < 0.05$.

3.2.13 Cell exclusion considerations

To reduce systematic error in our data, we have several considerations for excluding cells from the analysis. Our analysis requires all black dots near the edge of the cell field of view to be undeformed; any cells within close proximity of each other will disrupt this requirement. Therefore, cells which are close in proximity to other cells are automatically disregarded from all analysis; close proximity is defined here as two neighboring cell boundaries coming within 2 μm of each other. Another exclusion criterion are high net forces which are indicative of irregular patterning or mounting issues. We chose a cutoff of 10 nN and

excluded all cells exhibiting net forces higher than this cutoff from our data sets. Additionally, we excluded platelets that did not spread by excluding platelets < 10 μm^2 that had no filopodial or lamellipodial protrusions. Finally, fluorescence from F-actin staining was observed to be highly variable in some cells; we tuned the exposure time to the best of our abilities but for some cells it was difficult to completely eliminate image saturation. Therefore, we excluded cells that had greater than 1% saturated pixels within the cell boundary from the analysis shown in Figure 8, Figure 9, and Figure 10.

3.3 Results

3.3.1 Microcontact printing of black dots with uniformity in size, spacing, and shape

Black dots were manufactured, coated with extracellular matrix protein (ECM), and seeded with platelets (Figure 6B). In this work, the VWF was chosen as the ECM to facilitate platelet adhesion. Using a fluorescent anti-VWF antibody, we visualized VWF adsorption on the surface and found that VWF is adsorbed contiguously across the surface, with some preference for binding to the fluorescent BSA (Manuscript supplement, Figure 11A-G). Additionally, we have coated the black dots with other ECM such as fibrinogen (Manuscript supplement, Figure 11H-J) and laminin (Manuscript supplement, Figure 11K-M), so many cell types can be studied with this technique.

Once the black dots technique is optimized, it provides a consistent pattern and can be tailored to suit the nature of the cells. We created black dots with BSA conjugated with Alexa Fluor 488, 594, and 647 to demonstrate the versatility in the fluorescent coatings that are possible (Figure

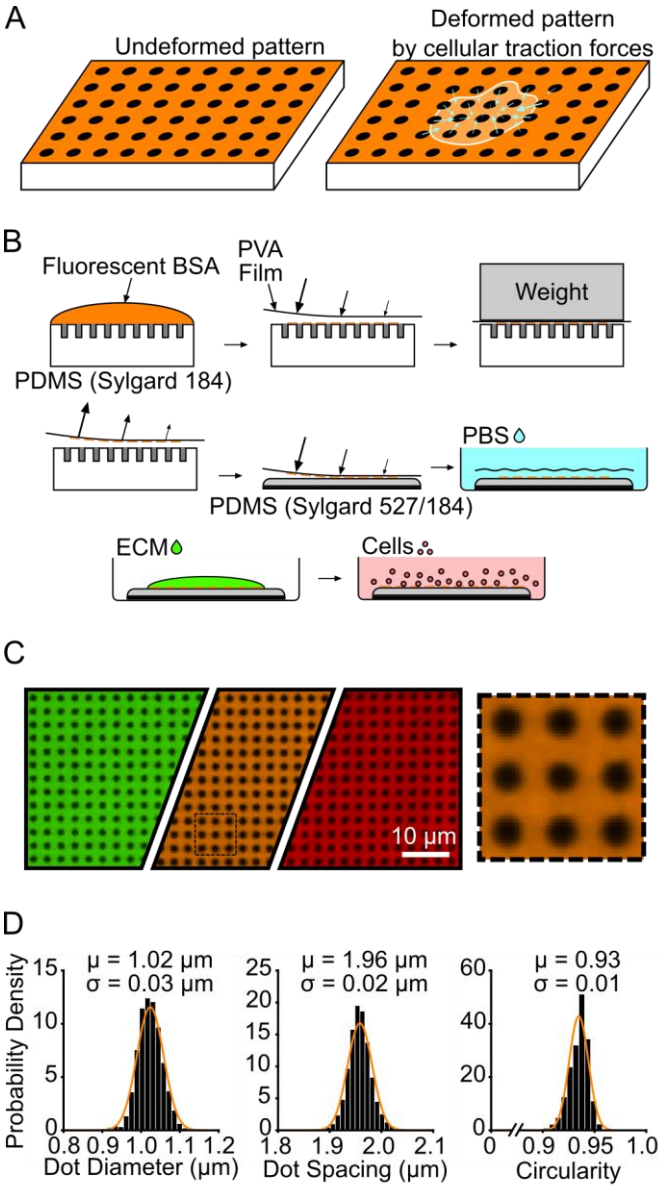

Figure 6 – Black dots overview, manufacturing, and characterization.
(A) Principle of black dots, where tension from an adhered cell causes the pattern of dots to displace. (B) Manufacturing black dots substrates using microcontact printing and a sacrificial PVA film to transfer an array of fiducial markers from a patterned stamp to a soft substrate. (C) Example of final manufactured substrate that can be made in the desired fluorescent channel using different fluorescent BSA such as BSA-Alexa Fluor 488 (green), BSA-Alexa Fluor 594 (orange), and BSA-Alexa Fluor 647 (red). The black dotted line area is shown on the right, scaled up 4X larger. (D) Characterization of diameter, center-center spacing, and circularity of black dots. μ = mean, σ = standard deviation. Data from 25,081 individual dots from 2 substrates. Y-axis is Probability Density for all three plots. Normal Gaussian probability density functions are overlayed.

6C). Through quantitative image analysis, the black dots were found to be uniform in size (1.02 ± 0.03 μm diameter), spacing (1.96 ± 0.02 μm center-to-center), and shape (0.93 ± 0.01 circularity) (Figure 6D). This pattern uniformity is critical for obtaining accurate results from image analysis and force calculations.

The soft PDMS we used resulted in a substrate with a stiffness of 13.5 kPa and was selected because it was physiologically relevant for platelets[113,114]. We tested softer and stiffer mixtures of Sylgard 527 and 184, but they were not optimal for traction force measurements with platelets because the resulting deformations of a subset of platelets were too large or too small to measure accurately (Manuscript supplement, Figure 12). For measurements with other cell types, the ratio of PDMS mixtures can be adjusted to match their level of contractility.

We have found that microcontact printing for the black dots can be a sensitive process, so care must be taken in preparing and storing the substrates. We have provided helpful tips and avoidable pitfalls for others to refer to in adopting the technique (Supplementary Note). Using our protocol, we typically print areas of black dots of 1 cm^2, but we have printed areas up to nearly 10 cm^2 with a larger PDMS stamp (Manuscript supplement, Figure 13). The black dots approach could potentially be scaled to larger culture dishes for even higher throughput in measurements. Overall, we have shown that the microcontact printing and sacrificial film technique can deposit fluorescent BSA patterns of black dots with regular size, spacing, and shape that cover a large surface area for experiments with cells.

3.3.2 Reference-free traction force microscopy with black dots

To demonstrate the black dots approach, we seeded human platelets and measured their traction forces. Washed platelets were seeded onto VWF-coated black dots for 10 minutes to allow them to adhere and then rinsed gently to remove unbound platelets. We waited an additional 30 minutes to allow the platelets to spread and contract before fixing the samples. This timing for platelet binding and contraction was selected based on dynamics of platelet force generation[6,7,19,47]. With immunofluorescence staining and confocal microscopy, many platelets can be captured in a single image (Figure 7A and manuscript

supplement, Figure 14). We note that the platelets had various shapes and sizes similar to previous observations on glass substrates[19,115]. Platelets were also seeded onto black dots without VWF and we observed that platelets did not bind and spread, demonstrating that the platelet adhesion is VWF-specific.

Individual platelets within an image are cropped and analyzed separately (Figure 7B). The centroid of each black dot is identified using automated detection (Figure 7C). Black dots at the edge of the region are used to form a grid of best-fit lines whose intersections denote the undeformed position of each black dot (Figure 7D). For each black dot, the distance from its centroid to its respective intersection in the zero-displacement grid (Figure 7D inset) is used to calculate the magnitude and direction of the forces using regularized Fourier Transform Traction Cytometry (FTTC) (Figure 7E)[70,111]. The black dot technique is suited well for FTTC, which requires the measured displacements to be on a regular grid. The total force for each platelet is calculated by summing the force magnitudes of each dot under the cell. All data plotted in this work is the total force of single platelets.

The total contractile forces of platelets from six healthy donors were analyzed (Figure 7F). The mean force measured by black dots was 24.1 nN, which is similar to other methods that have reported forces between 19 and 200 nN for individual platelets[5,7,47,91]. We also noted a wide range of forces, from 3.5 to 98.7 nN (28-fold difference) with a standard deviation of 14.7 nN. This observation agrees with other studies; atomic force microscopy found that platelet forces varied from 1.5 to 79 nN[91] (more than 50-fold difference), and subsequent work using TFM and nanoposts have also observed heterogeneity in platelet forces[5,7]. We observed heterogeneity both within and between donors, including a standard deviation of 13.7 nN among platelets from the same donor as well as statistically significant differences between mean platelet force from different donors (lines in Figure 7F). Our results show that platelet forces measured with black dots are similar in magnitude to previous measurements and indicate that populations of platelets produce a wide range of forces.

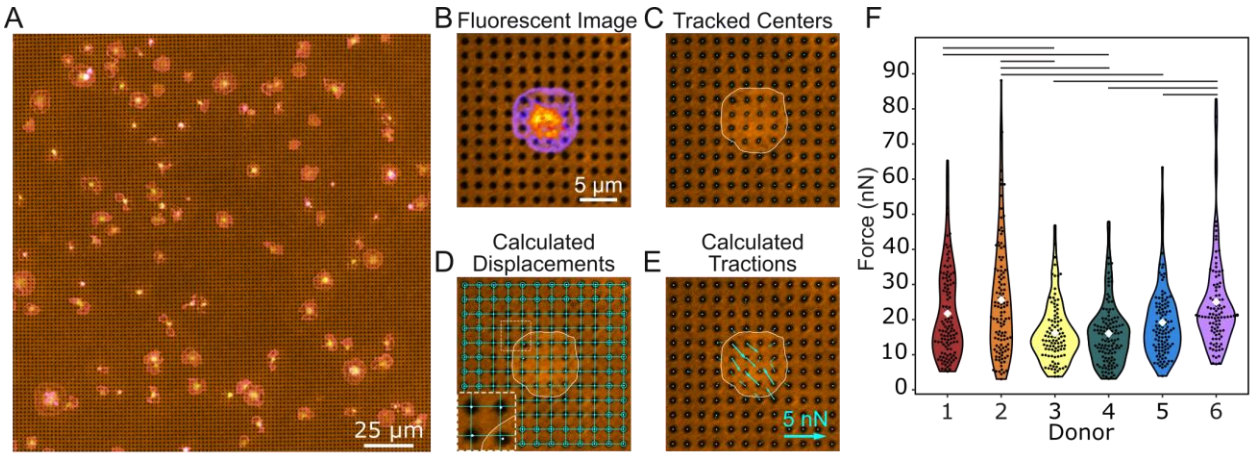

Figure 7 – Black dots offer a higher yield way to measure forces.
(A) Example of a field of view containing many platelets adhered to and contracting on the black dots. Here, platelets are stained for both F-actin (green) and GPIb (magenta). (B) A fluorescence image of deformed substrate with platelet stained for F-actin (pixel intensity scaled from purple to yellow). (C) The black dots pattern is binarized and the centroid of each dot is found using automated detection. (D) Undeformed dots near the edges (circled) are used to fit horizontal and vertical lines throughout the entire field of view. The intersection of these lines marks the zero-displacement state of each dot. Inset is 2x magnified. (E) Forces are calculated from the displacement of each dot relative to its zero-displacement (undeformed) location. (F) Forces from at least 100 platelets from 6 donors show high variability within each donor and between donors. Lines indicate significant differences in donor forces ($p < 0.05$ when tested with a one-way ANOVA and Tukey's post hoc test). Number of cells analyzed for donors 1, 2, 3, 4, 5, and 6 are n = 111, 117, 100, 120, 112, and 100, respectively.

3.3.3 Platelet forces correlate with spread area, circularity, and F-actin dispersion

We questioned whether the heterogeneity in total platelet forces could be attributed to their size, shape, and/or cytoskeletal structure. Platelets typically bind to a surface, increase their spread area approximately 5-fold over about 10 minutes, and then sustain their maximum spread area[7,19,20]. In our experiments, platelets were allowed to adhere and spread for 30-40 minutes after attachment to allow them to reach their maximum area. We examined spread area as a factor influencing the overall magnitude of traction forces in platelets as it has been observed previously[7,105] as well as in many other cell types[48,116,117]. We find that the spread area of platelets ranged from 8.7 to 205.5 µm^2, with a mean and standard deviation of 43.5 ± 22.4 µm^2. We observed a positive relationship between force and area, having a best-fit slope of 0.53 nN/µm^2 (R^2 = 0.49) (Figure 8A-C). This force-area relationship is maintained in all six donors, with some minor differences between them (Manuscript supplement, Figure 15). While our results indicate a strong force-area relationship in platelets, we do find a degree of heterogeneity in our results. For example, platelets with a spread area of 50-55 µm^2 exerted forces from 14.3 to 71.0 nN, with a mean and standard

deviation of 31.8 ± 13.3 nN. Although spread area has a strong correlation with platelet forces, it does not fully account for their contractile output.

Another aspect we considered was the dramatic shape changes of platelets such as their transition from discoid to spherical shape upon activation and their extension of filopodial protrusions in the early stages of platelet spreading[17,20]. Because these shape changes are important to platelet function, we investigated whether platelet shape correlates with force. We observed that adherent platelets on the black dots adopt a variety of different shapes, ranging from stellate to circular. We used an image analysis metric of circularity to quantitatively assess these different shapes (Figure 8D-E). We find that more circular platelets generate larger forces than ones that are stellate and less circular ones (Figure 8F). However, the best-fit slope of this relationship is 0.33 nN/0.01 circularity units (R^2 = 0.20) so it is not as correlative as the force-area relationship. All six donors showed similar force-circularity behavior (Manuscript supplement, Figure 16). These results indicate that circularity has a moderate correlation with force.

Due to the underlying role of actin remodeling in initiating platelet shape changes and generating cellular forces[17,20], we used black dots to determine whether actin arrangement correlates with platelet forces. When we stained the platelets to view their F-actin network on black dots, we observed a cortical actin ring around the cell boundary of most platelets. However, there were some distinct differences in the F-actin structure in their interior, ranging from punctate to dispersed (Figure 8G-H). The amount of F-actin dispersion was quantified and plotted against force. We found that platelets with more dispersed F-actin structure typically generated higher forces and the best-fit slope of this relationship is 0.21 nN/0.01 F-actin dispersion units (R^2 = 0.10) (Figure 8I). All six donors exhibited a similar force-F-actin dispersion relationship (Manuscript supplement, Figure 17). Collectively, we find that area has a strong correlation with force, and that circularity and F-actin dispersion moderately correlate with force.

3.3.4 Multivariate mixed effects modeling reveals cooperative effects between F-actin dispersion and circularity and between F-actin dispersion and spread area

Because platelet size, shape, and cytoskeletal organization change concurrently during platelet adhesion[20], we also investigated whether area, circularity, F-actin dispersion correlate with each other (Figure 9A, D, H). For area and circularity, we observed a moderate correlation (R^2 = 0.26) (Figure 8A). To visualize the combined relationship of circularity and area with increasing force, platelets were split into four equally sized groups by force, i.e., quartiles. Notably, low-force platelets had small areas, but also had a wide range of circularities. On the other hand, high-force platelets almost exclusively had high area and high circularity (Figure 9B and manuscript supplement, Figure 18 to see graphs with all points). By plotting the median of each quartile, we observed that circularity and area increase together with increasing force (Figure 9C). Similarly, area and F-actin dispersion (Figure 9D-F) as well as F-actin dispersion and circularity (Figure 9G-I) increase together with each force quartile. The particularly extreme shift observed in the circularity versus F-actin dispersion contour plots is somewhat surprising, given that each of these factors only moderately correlate with force. These results indicate that there are some correlations between platelet area, circularity, and F-actin dispersion and that

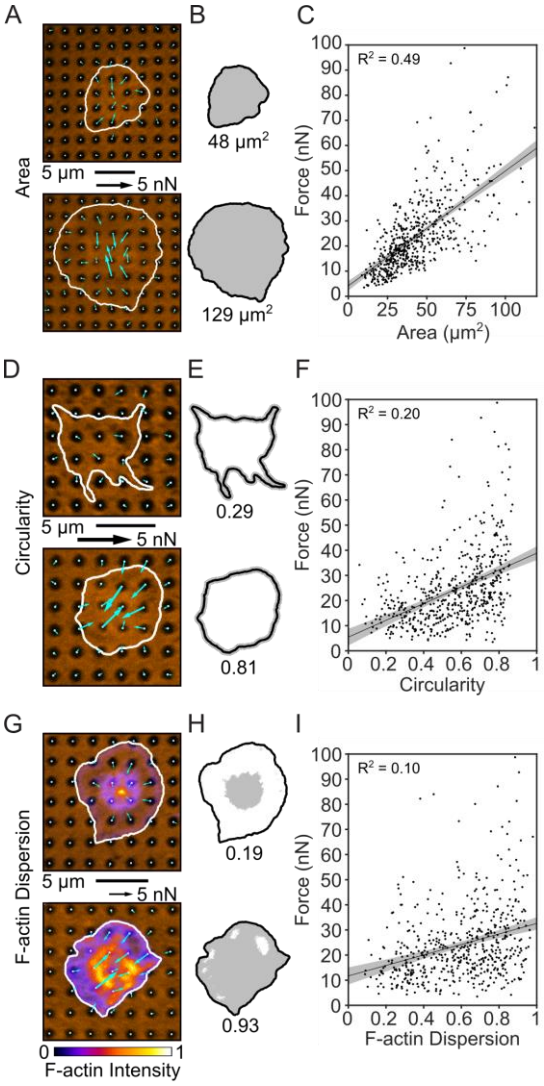

Figure 8 – Platelet size, shape, and structure correlate with platelet force.
(A) Two examples of platelets with small and large areas. (B) Cell boundary and area measured from (A). (C) Platelet forces and area are linearly related. Note that in this panel, the x-axis maximum is zoomed to better view the data. Due to this axis zoom, two points (0.37% of the data) are not shown, but all points are included within all analyses (including the fit line calculation). (D) Two examples of platelets with low and high circularity. (E) Cell boundary and circularity measured from (D). (F) Platelet force and circularity show a moderate positive relationship. (G) Two examples of platelets with low and high F-actin dispersion. Color bar indicates fluorescence intensity which has been normalized to calculate F-actin dispersion. (H) Cell boundary and F-actin dispersion measured from (G). (I) F-actin dispersion is moderately positively correlated with platelet force. Shaded regions of fit lines indicate 95% prediction interval for the data.

together, they have strong effects on force. We next turned to a more robust approach to assess interaction effects between these factors.

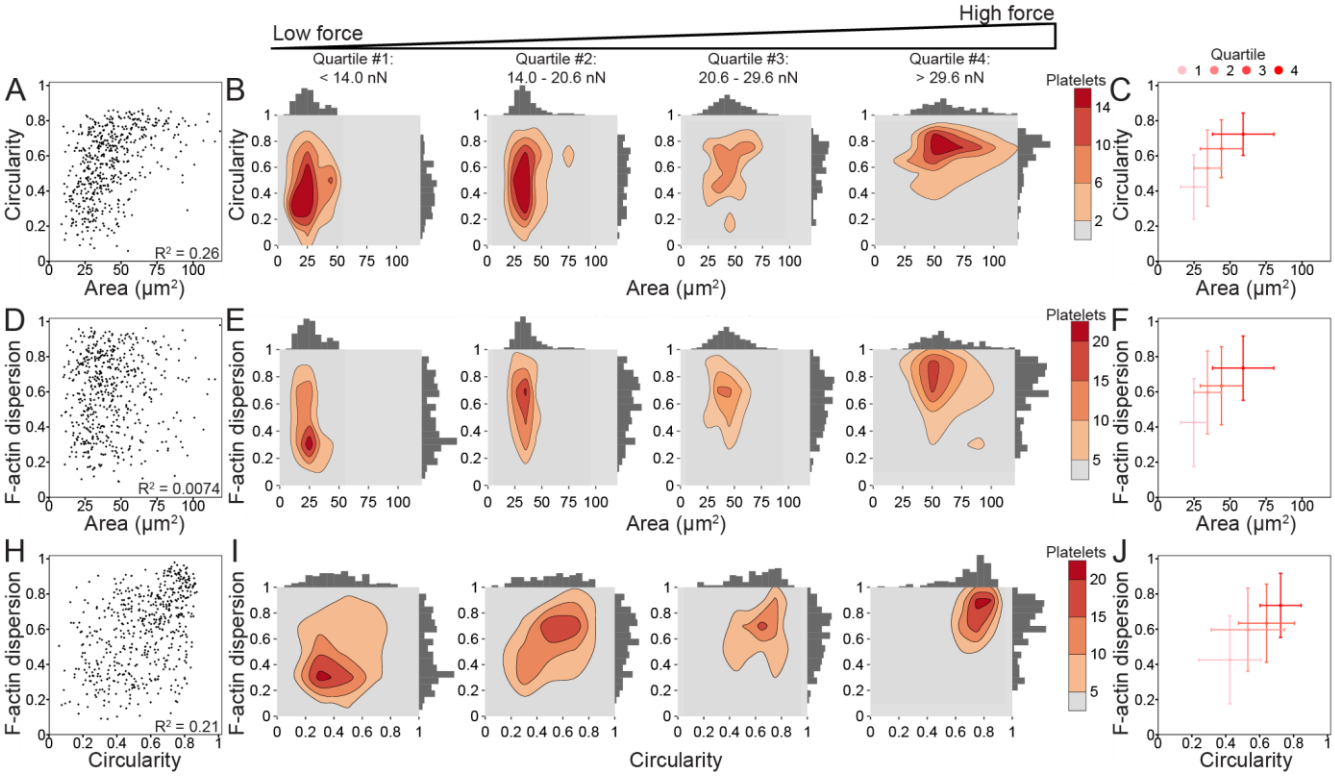

Figure 9 – Platelet size, shape, and structure do not strongly correlate with each other, but increase together with force.
(A) Area and circularity moderately correlate (R^2 = 0.26) when plotting platelets of all forces (n = 540). (B) To examine the relationship of circularity and area with increasing force, platelets are split into four quartiles (n = 135 in each quartile) by force, where the lowest force quartile (quartile #1) includes platelets generating less than 14.0 nN force, quartile #2 contains platelets generating 14.0-20.6 nN force, quartile #3 contains platelets generating 20.6-29.6 nN force, and the highest force quartile (quartile #4) contains platelets generating greater than 29.6 nN force. Contour density plots and histograms of area and circularity at each force quartile show that quartile #1 (low-force platelets) have low area and a large range of circularity, while quartile #4 (high-force platelets) tend to have both higher area and high circularity. (C) The median and median standard deviation show that circularity and area increase together with each force quartile. (D) F-actin dispersion and area do not correlate (R^2 = 0.0074), (E-F) but show a similar trend when examining force quartiles. (H) F-actin dispersion and circularity moderately correlate (R^2 = 0.21) and (I-J) show a shift from low-force platelets having large ranges of circularity and F-actin dispersion to high-force platelets have high circularity and high F-actin dispersion. Note that in A-F, the x-axis maximum is zoomed to better view the data. Due to this axis zoom, two points (0.37% of the data) are not shown, but all points are included within all analyses.

To further investigate how F-actin dispersion, circularity, and area affect force in different but overlapping ways, we used R Studio to create a multivariate mixed effects model allowing for 2-way interactions between each of the factors (Table 2). The mixed effects model shows that across donors, the difference in force between two platelets that differ in area by 1 μm^2 (while other factors remain constant) is 0.41 nN

(95% CI: 0.37, 0.45) on average, with the larger platelet generating more force (Table 2). Similarly, when holding other factors constant, two platelets that differ in circularity or F-actin dispersion by 0.01 will respectively differ in force by 0.069 nN (95% CI: 0.02, 0.11) and 0.15 nN (95% CI: 0.11, 0.19), on average. From estimates and standard errors in Table 2, p-values are calculated to determine what factors and interactions have a significant ($p < 0.05$) effect on force. All individual factors (area, circularity, and F-actin dispersion) significantly contribute to force when controlling for the other factors. In addition to these main effects, two interaction terms were significant at the $p < 0.05$ level: F-actin dispersion interacting with area and F-actin dispersion interacting with circularity, each of which is a positive, cooperative effect. For example, when circularity is average, F-actin dispersion and force have a positive relationship with a slope of 0.069 nN/0.01 F-actin dispersion units. When circularity is one standard deviation above average, the relationship between F-actin dispersion and circularity is stronger and has a slope of 0.12 nN/0.01 F-actin dispersion units (75% increase). Conversely, when circularity is one standard deviation below average, the relationship between F-actin dispersion and circularity is weaker and has a slope of 0.017 nN/0.01 F-actin dispersion units (75% decrease) (Manuscript supplement, Figure 19E and Figure 19 for all other interaction plots). Area interacting with circularity has a p-value of 0.2079 and is not significant at the $p < 0.05$ level. This multivariate mixed effects model supports the contribution of area, circularity, and F-actin dispersion to force and suggests a complex relationship between these factors. Additionally, this analysis reveals significant cooperative effects between F-actin dispersion and circularity and between F-actin dispersion and area.

Table 2 – Multivariate mixed effects model summary shows significant interaction effects.
The estimate column indicates the expected increase in force (in nN) if the variable in that row increases by 1 μm^2 (area) and/or 0.01 units of circularity or F-actin dispersion while all other factors remain constant. The standard error column indicates the error of that estimate. From these estimates and standard errors, p-values are calculated to determine what factors and interactions have a significant ($p < 0.05$) effect on force. In addition to these individual effects, pairs of effects were tested for interactions, where a positive value in the estimate column indicates a cooperative effect and a negative value an antagonistic effect.

	Estimate	Std. Error	p-value
Area [nN/μm^2]	0.4100	0.0209	< 0.001
Circularity [nN/0.01 units]	0.0687	0.0247	0.0053
F-actin dispersion [nN/0.01 units]	0.1488	0.0187	< 0.001
Circularity : F-actin dispersion [nN/(0.01 units*0.01 units)]	0.0024	0.0010	0.0134
Area : F-actin dispersion [nN/(μm^2*0.01 units)]	0.0024	0.0008	0.0028
Area : Circularity [nN/(μm^2*0.01 units)]	-0.0012	0.0009	0.2079

3.3.5 Unbiased clustering supports relationship between spread area, circularity, F-actin dispersion, and platelet force

Big data analyses are powerful tools that can help extract significant information in data sets that are large and unwieldy. In our population of platelets, we observed a large range of shapes, sizes, and structures, so we wanted to investigate whether there are clusters or subpopulations of platelets in our data set. We performed an unbiased K-means clustering analysis on platelet area, circularity, and F-actin dispersion to locate possible clusters, and to see if the relationships we observed between these factors and force could be explained by distinct clusters or subpopulations of platelets. Two clusters arose from this analysis: cluster 1 is generally characterized by low spread area, circularity, and F-actin dispersion while cluster 2 is high spread

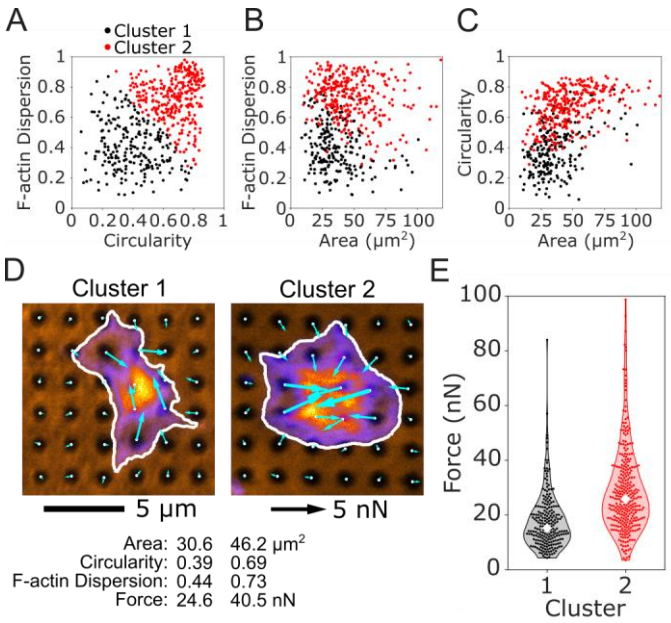

Figure 10 – K-means clustering of platelet size, shape, and structure predict differences in force.
An unbiased K-means clustering approach based on platelet area, circularity, and F-actin dispersion separated the population of platelets into 2 clusters. The two clusters are shown for (A) F-actin dispersion and circularity, (B) F-actin dispersion and area, and (C) circularity and area. (D) The most representative platelet from each cluster is shown. Platelets from cluster 1 have smaller area, lower circularity, and lower F-actin dispersion than cluster 2. (E) Forces from cluster 2 are significantly higher than cluster 1, even though force was not used to determine the clusters.

area, circularity, and F-actin dispersion (Figure 10A-D and manuscript supplement, Figure 20A-D). We also performed the clustering analysis on each donor individually; each donor generally formed two clusters that were similar to the two clusters in the overall data set (Manuscript supplement, Figure 20E-J). For this clustering analysis, we intentionally did not include the force data; despite this agnostic approach to platelet force, we find that cluster 2 has significantly higher forces than cluster 1 using a student's t-test (Figure 10E), supporting our earlier findings.

K-means clustering was chosen here due to its simplicity and widespread use, although other clustering methods may be more appropriate depending on the data set. By eye, the two clusters in our data set tend to lie on a continuum rather than distinct clusters with no overlap. This could indicate that the two clusters do not originate from distinct sources, but instead emerge from a single gradient such as platelet age in circulation, where older platelets tend to have less spread area, less circularity, and less dispersed F-actin. The physiological origin and significance of these clusters will be further investigated in future studies. Ultimately, this clustering analysis serves as a demonstration of big data analyses that are made possible by data from hundreds of cells collected with a high-yield method.

3.4 Discussion

Here, we showed how the black dots approach is used to measure traction forces in platelets. The black dots were coated with VWF, an adhesive blood protein that mediates platelet adhesion. The choice of ECM depends on the cell type being studied, so we demonstrated that black dots could instead be coated with fibrinogen or laminin which are commonly used for many cell types. Additionally, the substrate stiffness of 13.5 kPa was selected because it was physiologically relevant for platelets[113,114]. Other cell types may be more suited to a different stiffness; our platform utilizes a mixture of two types of PDMS which can be adjusted to change the final substrate stiffness[108]. Overall, the black dots approach may be useful to measure traction forces for many cell types, and not only platelets.

We used the black dots technique to characterize the relationship of force with platelet size, shape, and cytoskeletal structure. We measured forces of more than 500 platelets, which is five times more than previous studies[6,7,105] and is on par with existing high-yield methods that directly control cell shape and area[47]. The magnitude of forces from our technique is similar to other methods that have reported forces for individual platelets[5,7,47,91]. For the first time, we were able to correlate platelet forces to platelet circularity and F-actin dispersion. This was only possible with the black dots technique because it does not constrain platelet shape or size and is compatible with the immunofluorescent techniques necessary to study the cytoskeleton. We found significant associations between spread area, circularity, F-actin dispersion, and force, as well as interactions between these factors that significantly contribute to platelet force generation. When the independent effects are determined with a multivariate mixed effects model, F-actin dispersion associates more strongly with force than circularity, because it is less correlated with area. Moreover, cooperative interactions between F-actin dispersion and both area and circularity further highlight the importance of F-actin structure in generating contractile forces and provide new insight into the large heterogeneity of observed platelet forces.

Beyond the measures of area, circularity, and F-actin dispersion, the amount of contractile force a cell can generate likely depends on several factors that we have not measured here, including activation of the actomyosin network by phosphorylation, amount and organization of the contractile fibers, genetic differences between donors, and disease states. We anticipate that the black dots platform may be used in conjunction with detailed fluorescent staining, western-blotting, or genetic screening to further enhance the understanding of force generation of platelets and other cells.

3.5 Conclusion

The black dots approach is a high-yield single-cell force measurement platform that is compatible with fixed cells without constraining cell shape and size. It relies on microcontact-printing and algorithms from reference-free traction force microscopy to measure traction forces of individual cells. We demonstrate the

technique's benefits by measuring forces of more than 500 platelets, a high yield for traction force measurements. Using this approach, we were able to correlate platelet forces to platelet circularity and F-actin dispersion, revealing cooperative effects. By tuning the substrate stiffness, extracellular matrix protein, and BSA fluorescence, the black dots approach may be useful to measure the forces in many cell types beyond platelets.

3.6 Supplementary information

3.6.1 Supplementary Note

Throughout the development of the black dots method, we encountered steps several steps in the manufacturing process that required optimization. Here are some tips that increased the reliability when manufacturing black dots:

Master mold

For platelets, the master contained a designed pattern of round dots with a nominal diameter of 1 µm and spacing of 2 µm. The actual spacing between dots on the SU-8 master mold was found to be 1.99 µm measured by widefield microscopy (data not shown here). The final fluorescent pattern of black dots were measured to have a mean diameter of 1.02 µm and mean spacing of 1.96 µm as shown in Figure 1D, suggesting that the negative PDMS stamp had some shrinkage during the manufacturing steps.

Soft PDMS substrates

When making the soft PDMS coverslips, keeping the platform flat to ensure even spreading of PDMS was important to reduce tilt when imaging. We found that placing the coverslips onto the inside of the top lid of a petri dish, rather than the bottom, provided a more consistent flat surface when baking at 65 ^{o}C.

It is very important that the soft PDMS substrates remain as clean as possible after creation; keeping them stored in a parafilm-closed petri dish and only opening the dish in a TC hood are useful for preventing dust buildup.

PVA film

When making the PVA film, the PVA powder will only form a solution when heated. We preferred to heat the mixture in a 110 ^{o}C oven for 30 minutes rather than using a microwave, as other literature suggests, in order to prevent boiling and loss of liquid. Filtering the liquid PVA was also useful for ensuring a homogeneous and flat film.

Plasma-treating the petri dish before pouring in the liquid PVA ensured that the film remained attached to the petri dish and did not lift off prematurely.

Stamping

When coating the PDMS stamp with fluorescent BSA, special care should be taken when rinsing the stamp with PBS. Remove the stamp from the PBS slowly and at an angle to ensure that as much liquid as possible is removed from the stamp. When PBS dries, it tends to leave behind salt crystals which can disrupt the pattern if it is allowed to dry on top of the stamp.

If the concentration of BSA is too high, the pattern features may get filled in with fluorescence and result in a poor-looking pattern when transferred. Avoid too small features or too high concentration of BSA.

When drying the stamp with Nitrogen gas after the final PBS rinse, use a low velocity stream as the fluorescent BSA layer can be fragile.

When placing the PVA film onto the stamp, use a pair of tweezers to gently push on the film from the center outwards to eliminate bubbles between the two surfaces.

3.6.2 Supplementary Methods

PDMS stiffness measurements

Dog bone-shaped samples of mixtures of PDMS (Sylgard 527 and 184) were created to measure their stiffness. Mixtures of 2.5%, 5%, and 10% ratios of Sylgard 184 to Sylgard 527 were poured into molds and cured at 65 ^{o}C overnight. After curing, two spots used for measuring strain were drawn in the neck region

of the sample. Several loads were hanged from a sample and imaged with a typical phone camera to evaluate the resulting engineering stress and strain for each load (Manuscript supplement, Figure 12A). Stress was calculated by dividing the applied weight by the minimum cross-sectional area of the sample (measured by analog calipers), and strain was calculated by measuring the distance between the two spots drawn previously. When plotted, the data points form a straight line where the slope of the line is the stiffness or Young's modulus. We measured stiffness on 3 separate samples for each PDMS mixture.

Our measurements found that mixtures containing 2.5%, 5%, and 10% Sylgard 184 results in stiffnesses or Young's modulus of 7.7, 13.5, and 46.7 kPa (Manuscript supplement, Figure 12B). These measurements agree closely with prior literature[108].

Fibrinogen treatment of black dots

Fibrinogen from human plasma that is conjugated to Alexa Fluor-488 (Life Technologies) was diluted to 0.15 mg/mL and incubated on the black dots for 1 hour. Substrates were mounted onto glass coverslips using Fluoromount-G mounting medium (Life Technologies) and imaged with confocal microscopy (Manuscript supplement, Figure 11H-J).

Laminin treatment of black dots

Mouse laminin (Life Technologies, 23017015) was diluted to 10 μg/mL and incubated directly onto black dots for 1 hour. Laminin was then labeled with a rabbit anti-laminin antibody (Millipore Sigma, L9393) and a goat anti-mouse IgG secondary antibody conjugated to Alexa Fluor 488 (Life Technologies, A-11008). The labeled substrate was then imaged by widefield microscopy (Manuscript supplement, Figure 11K-M).

3.6.3 Donor Specific Results

Force-Area, Force-Circularity, and Force-F-actin Dispersion Relationships

Figure 15-Figure 17 show the Force-Area, Force-Circularity, and Force-F-actin dispersion results for each donor. Fit lines through the data were constrained to pass through the origin for Force-Area, but not for Force-Circularity or Force-F-actin dispersion. The slopes of these lines indicates the strength of the

relationships, which is slightly different for each donor as shown in panel C of Figure 15-Figure 17. An ANOCOVA with Tukey's post hoc test was used find significance between slopes.

K-means Clustering

The manuscript supplement Figure 20 shows the K-means clustering performed for each donor separately. All 6 donors exhibited similar patterns when separated into two clusters, although donor 4 tends to cluster more strongly by area than other donors.

3.6.4 Technique Resolution, Yield, Sensitivity, and Traction Reconstruction Considerations

Technique resolution

Each black dot is 1.02 μm in diameter and has center-to-center spacing of 1.96 μm (Figure 6D), resulting in approximately 30 markers per 100 μm^2 and displacement of 25 dots, on average, included in the force calculation of each platelet. This force resolution is higher than some methods to measure single-cell forces, and lower than others. For example, alternative methods to measure single-platelet forces include a standard TFM approach measuring bead displacement[6,7,105], nanoposts[5], and a two-dot reference-free TFM method[47]. Roughly estimating from images and videos within these studies[6,7,105], the standard TFM method has roughly 120 markers randomly dispersed per 100 μm^2. Nanoposts are spaced similarly to black dots[5] and consequently have equal force resolution. The two-dot reference-free TFM method spaces ~1 μm diameter dots ~4 μm center-to-center and spaces dot pairs sufficiently apart such that cell forces are always measured from the displacement of two markers per platelet[47]. Ultimately, the resolution of black dots is approximately 10-fold higher than some methods[47], equal to other methods[5], and approximately 4-fold lower than other methods[6,7,105].

Technique yield

This study measured the forces of 660 platelets from 6 donors. Black dots yield is comparable with the two-dot TFM method that measured approximately 84 platelets per donor and a total of 818 platelet forces [47]. Black dots yield is higher than standard TFM approaches that measured as low as 14 or as many as

approximately 225 platelets per study [6,7,105]. Ultimately the yield of black dots is higher than comparable approaches that do not restrain cell size and shape [6,7,105] while being comparable to high-yield, reference-free methods that do restrain cell size and shape [47].

Technique sensitivity

The sensitivity of black dots was investigated by measuring the effect of dot spacing on force estimation. Different pattern spacing was simulated by skipping rows and columns from the existing displacement measurements (Manuscript supplement, Figure 21A). For example, the pattern used in this study had a nominal dot spacing of 2 µm. By using only the displacements from every other dot, we effectively simulate a dot spacing of 4 µm. Using every third or every fourth dot, a spacing of 6 µm or 8 µm is achieved. The average number of dots within each platelet was 24.9, 6.2, 2.8, and 1.5 for dot spacings of 2, 4, 6, and 8 µm, respectively. Total force was estimated for each of these different simulated dot spacings for all platelets in this study (Manuscript supplement, Figure 21B). No significant difference was detected for estimated platelet force between 2, 4, and 6 µm. Force estimated from a dot spacing of 8 µm was significantly lower than the other tested dot spacings ($p < 0.05$ when tested with paired t-tests). A dot spacing of 8 µm is likely too large for these cells as indicated by the large number of cells exhibiting no force; these cells had no dots beneath them to measure displacement or force. Overall, this data suggests that the 2 µm spacing used in this study is sufficiently small enough to accurately estimate force. While force on the 6 µm spacing is not significantly different than on the 2 µm spacing, the higher resolution in displacement measurements offered by lower spacing is important for ensuring each platelet has a sufficient number of dots to measure displacement.

Traction reconstruction considerations

FTTC requires input of displacements in a regular grid. In a system that uses randomly dispersed markers, like traditional TFM, interpolation is required to obtain displacements in a regular grid. This interpolation can introduce inaccuracies especially if the marker beads are not homogeneously distributed. Using black dots, wherein markers are already in a regular grid, no interpolation is required.

Because platelets in this study are stationary and are assumed to be in static equilibrium, net forces should tend towards 0. Median net forces of cells included in this study were 2.75 nN. Cells exhibiting large net forces (> 11.25 nN) were excluded from this work.

3.6.4 Supplementary Figures

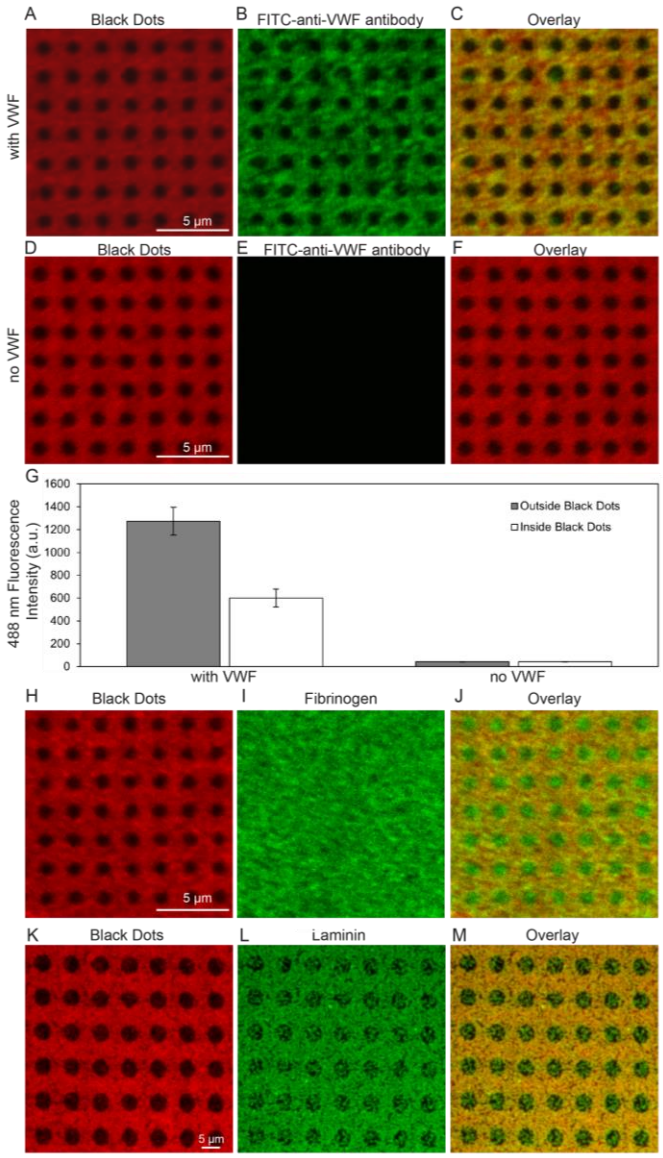

Figure 11 – ECM treatment of black dots.
(A-C) VWF-treated black dots with fluorescent BSA shown in red (A), VWF labeled with a FITC-anti-VWF antibody shown in green (B), and an overlay (C). Qualitatively, VWF is bound to both the fluorescent-BSA (orange in C) as well as the non-fluorescent black dots (green in C). (D-F) Black dots without VWF treatment with fluorescent BSA shown in red (D), VWF labeled with a FITC-anti-VWF antibody shown in green (E), and an overlay (F). As expected, the FITC-anti-VWF antibody does not bind to the substrate without VWF treatment (E). (G) Quantitatively, substrates with VWF have VWF bound both outside the black dots (gray bar) and inside the black dots (white bar), with higher fluorescent intensity outside the black dots. As expected, substrates without VWF have negligible 488 fluorescence both inside and outside the black dots. (H-I) Black dots can also be treated with fluorescent-fibrinogen, which binds uniformly across the surface, or (K-M) laminin, which has some preference for binding outside the black dots. Note that because we typically use laminin with larger cells (not platelets), its binding was characterized on black dots with a larger diameter. In this figure, the black dots are shown in red instead of orange because the red/green overlay is easier to interpret than the orange/green overlay.

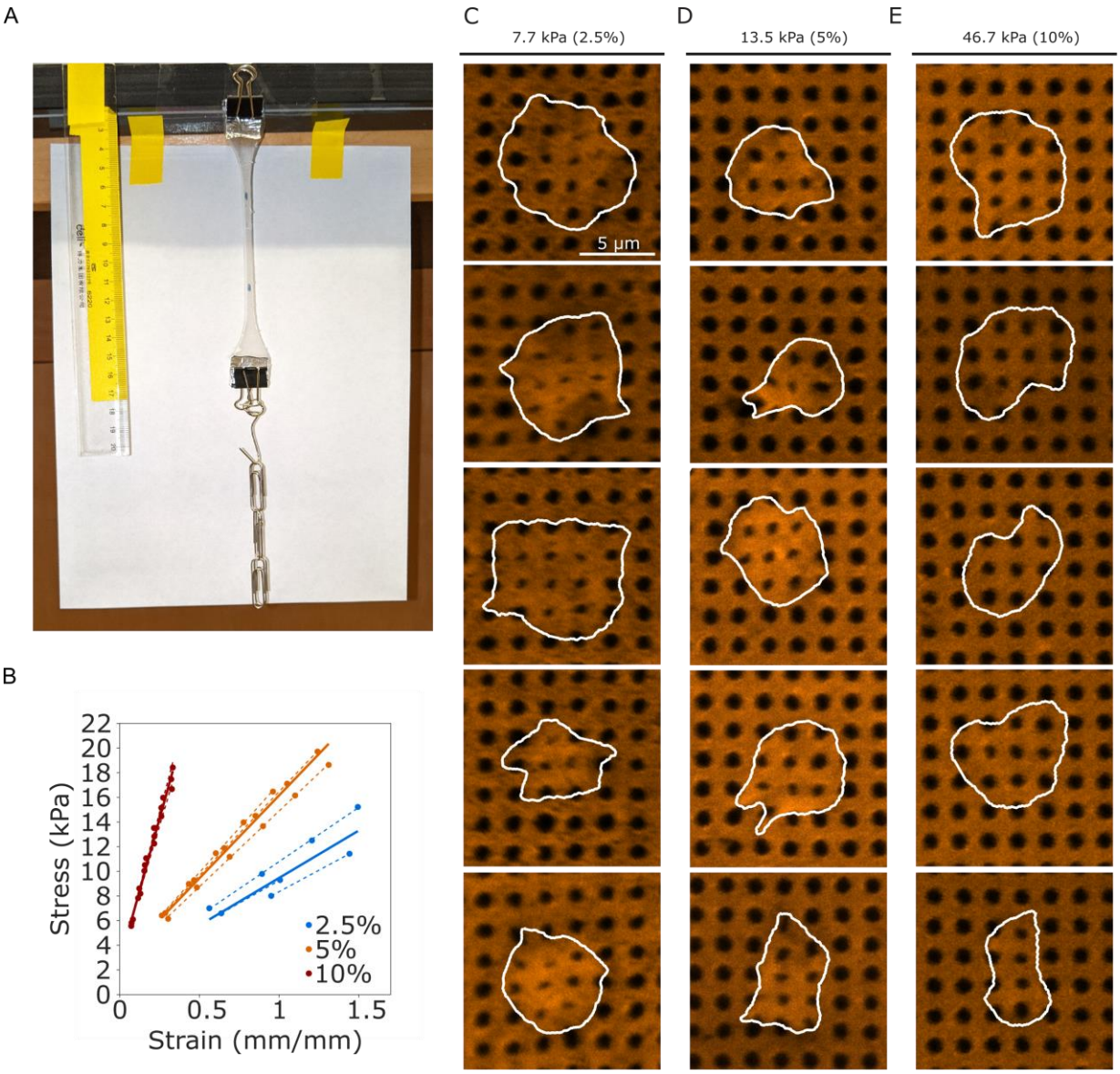

Figure 12 – Selection of substrate stiffness.
(A) PDMS tensile testing apparatus to measure the Young's modulus of each mixture of PDMS. (B) Measurements of stress and strain from the tensile test. Dotted lines indicate lines of best fit for each experiment. Solid lines are the average slope and intercept for the dashed lines for each given PDMS mixture. (C-E) Examples of platelets attached to black dots for the three different PDMS mixtures. Platelets on low stiffness (C) can distort the dots too much for image detection, while platelets on high stiffness (E) sometimes don't distort the dots beyond noise levels. The stiffness of 13.5 kPa in (D) was chosen for the studies presented in this paper.

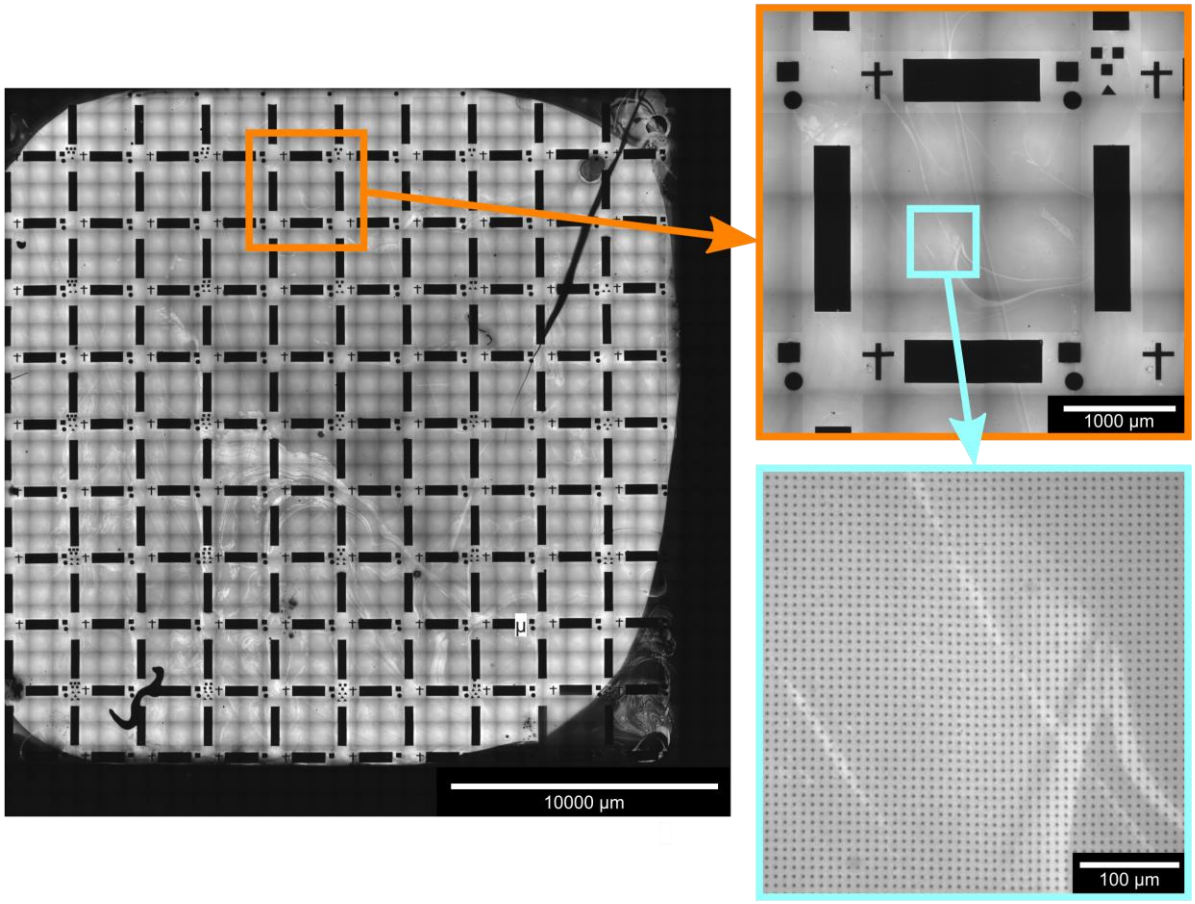

Figure 13 – Black dots can be printed over larger areas.
In this example, black dots have 9 um center-to-center spacing and cover a total physical area of nearly 4 cm^2.

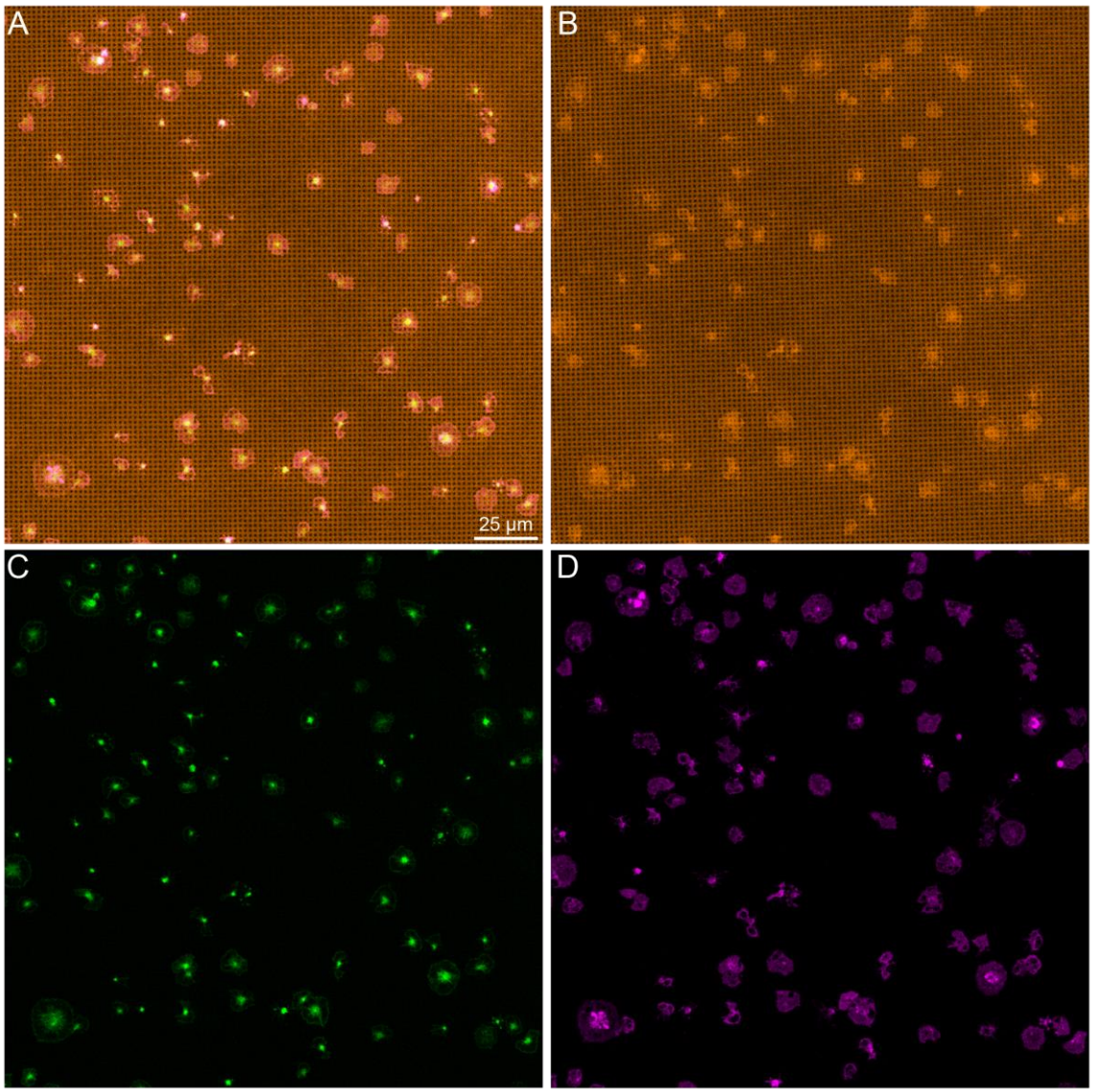

Figure 14 – Field of view containing many platelets adhered to and contracting on the black dots.
This figure shows the same image as Figure 6A, but with each channel shown separately. Here, (A) is an overlay of all channels, (B) is the black dots in orange, (C) is F-actin in green, and (D) is GPIb in magenta.

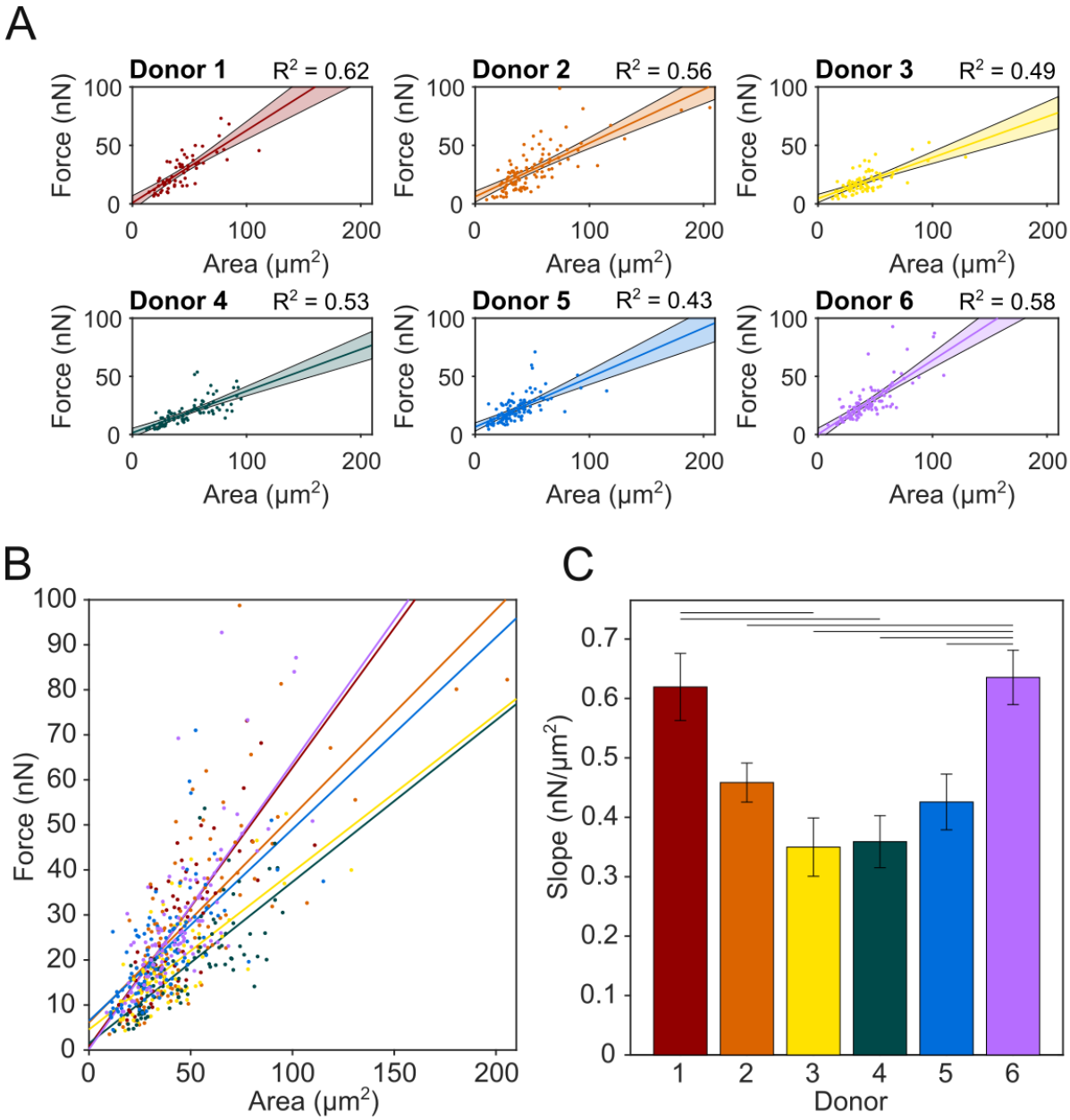

Figure 15 – Force-area relationship by donor.
(A) Force-area data plotted separately for each donor. Solid fit lines are displayed with shaded area that indicates 95% prediction interval for the fits. (B) Overlay of force-area data from all 6 donors with linear fit lines for each donor. (C) Slopes for the fit lines for each donor. Horizontal bars at the top indicate significance ($p < 0.05$ when tested with a one-way ANOCOVA and Tukey's post hoc test).

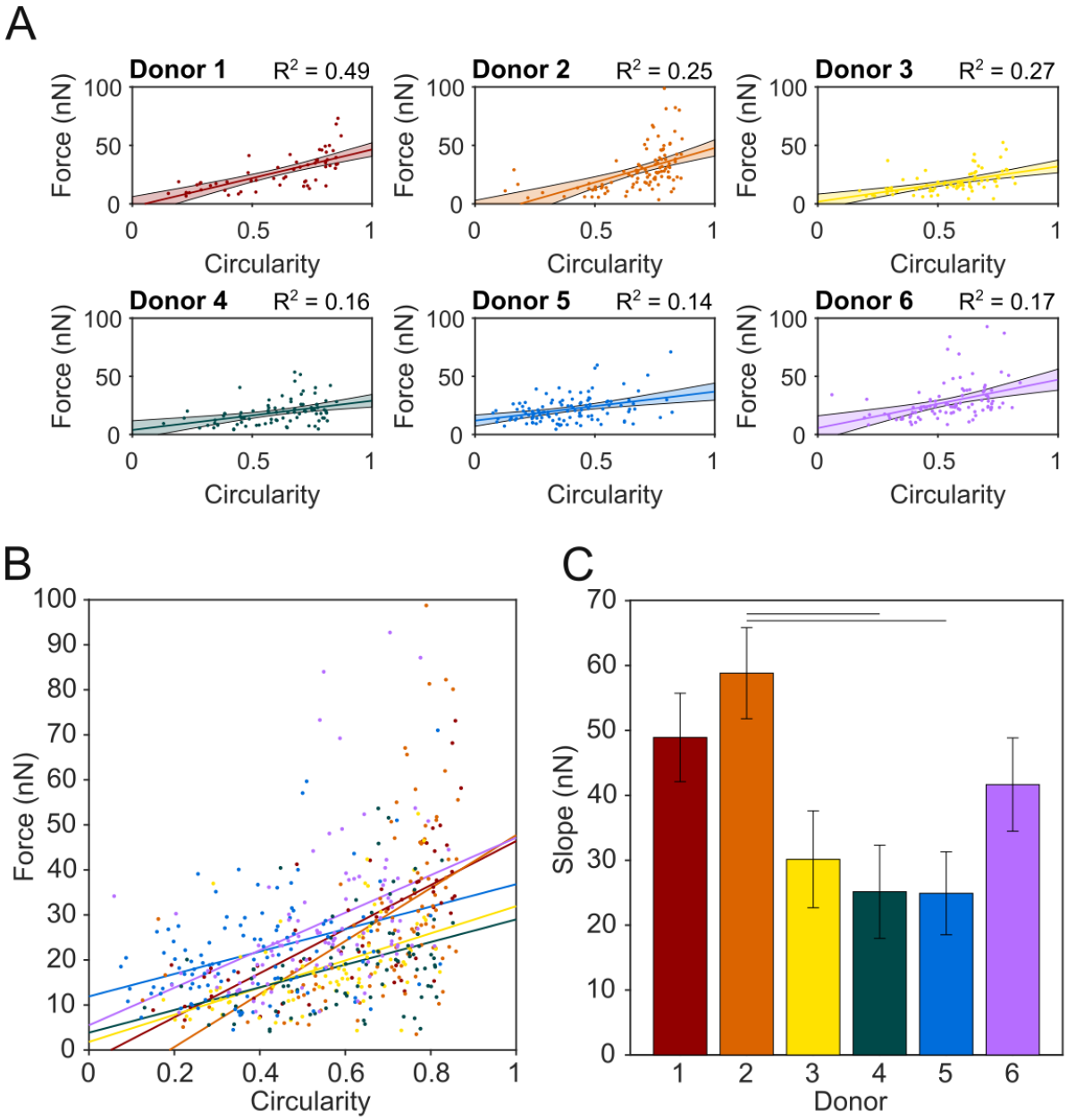

Figure 16 – Force-circularity relationship by donor.
(A) Force-circularity data plotted separately for each donor. Solid fit lines are displayed with shaded area that indicates 95% prediction interval for the fits. (B) Overlay of force-circularity data from all 6 donors with linear fit lines for each donor. (C) Slopes for the fit lines for each donor. Horizontal bars at the top indicate significance ($p < 0.05$ when tested with a one-way ANOCOVA and Tukey's post hoc test).

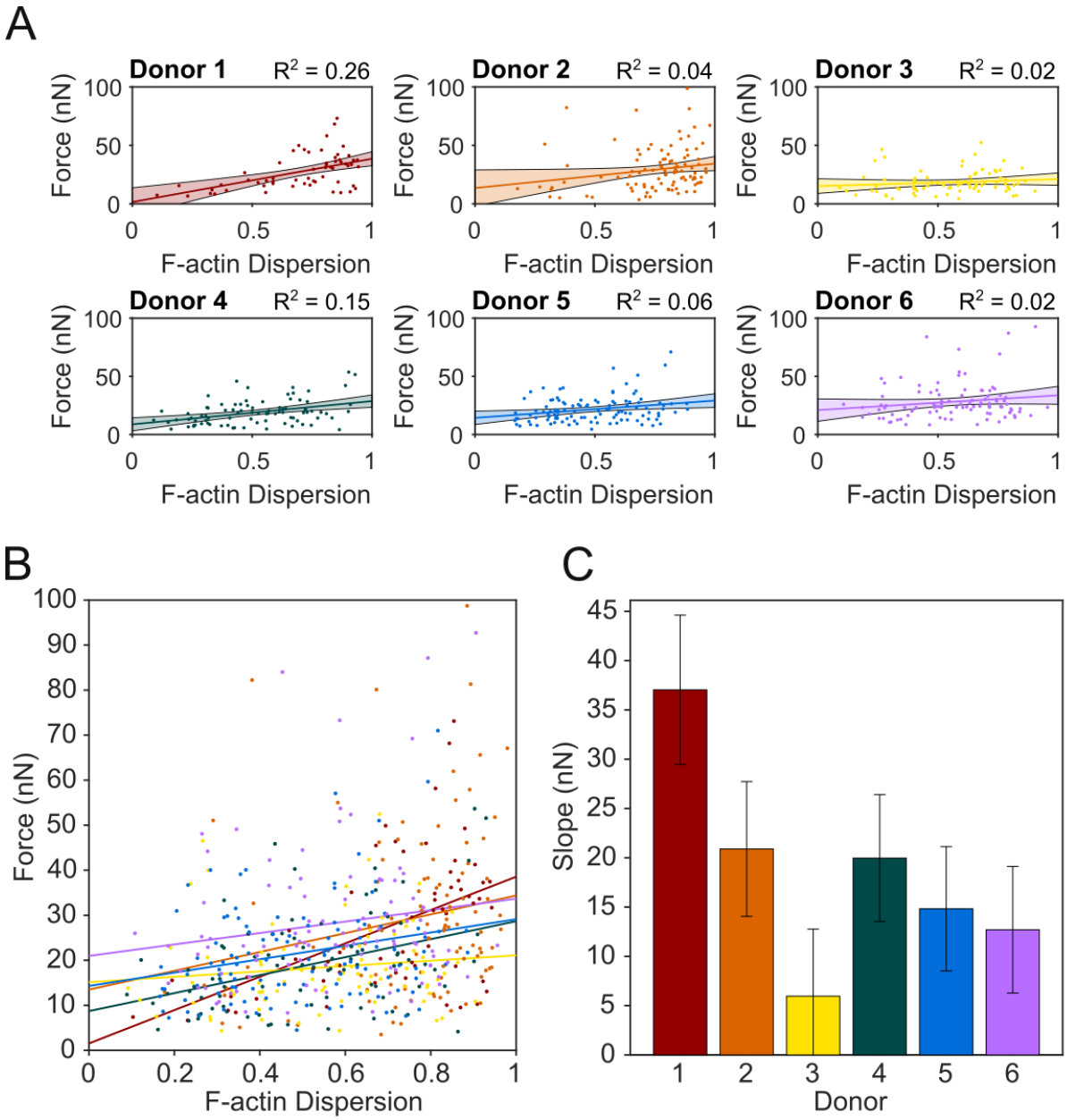

Figure 17 – Force-F-actin dispersion relationship by donor.
A) Force-F-actin dispersion data plotted separately for each donor. Solid fit lines are displayed with shaded area that indicates 95% prediction interval for the fits. (B) Overlay of force-F-actin dispersion data from all 6 donors with linear fit lines for each donor. (C) Slopes for the fit lines for each donor. No significance was detected for the slopes between donors when tested with a one-way ANOCOVA and Tukey's post hoc test.

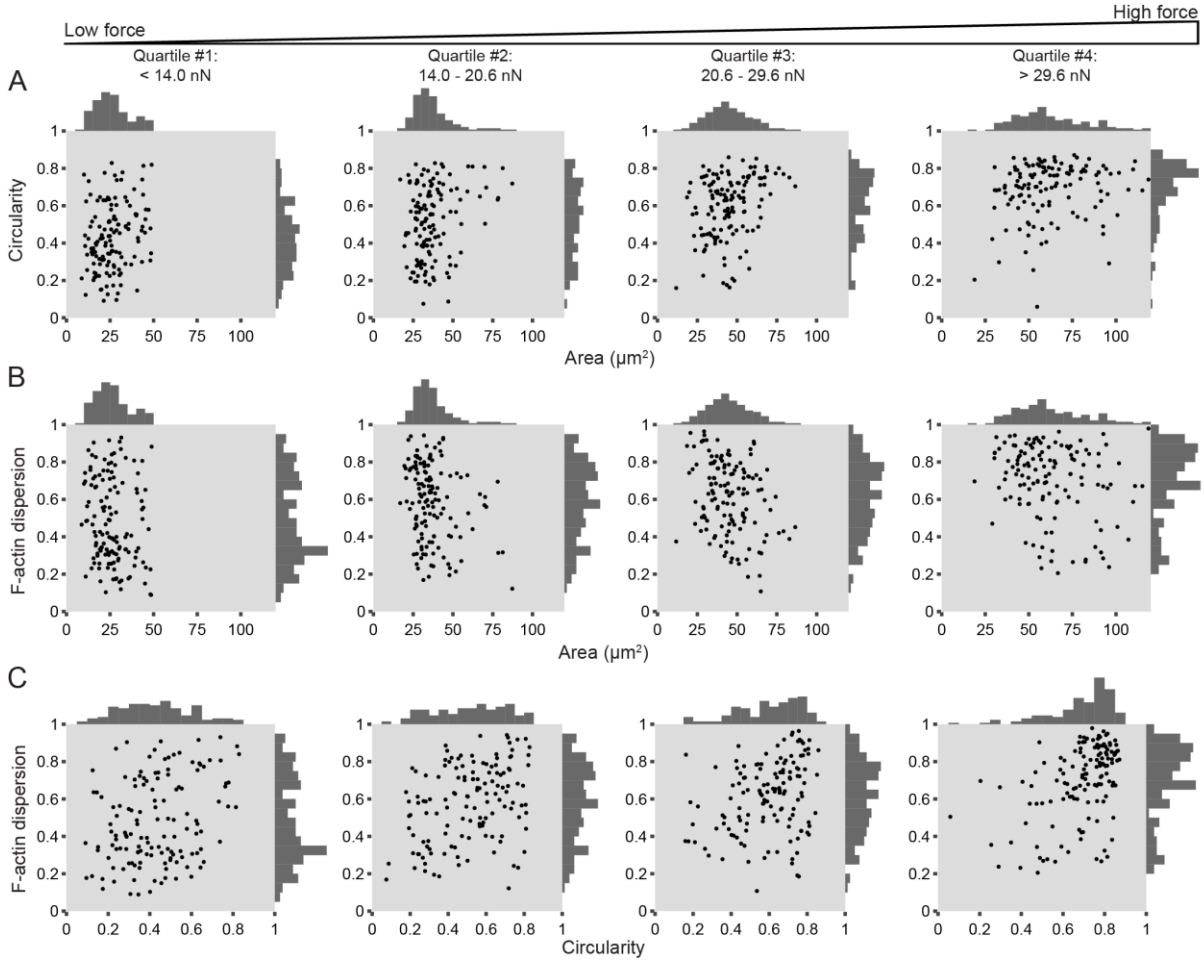

Figure 18 – Platelet size, shape, and structure do not strongly correlate with each other, but increase together with force.
This figure shows the same data as main text Figure 8B, E, and I, but with a scatter plot instead of a contour plot to display all points of data.

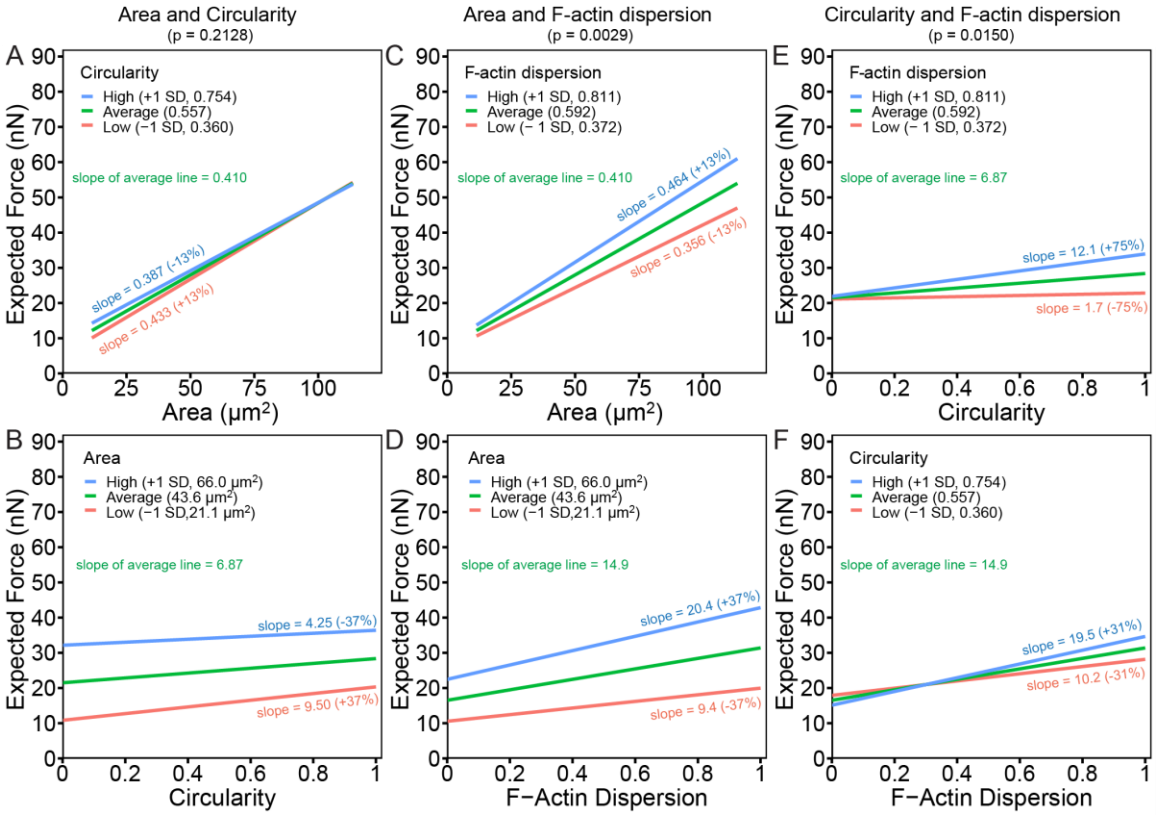

Figure 19 – Interaction plots demonstrate cooperative interactions between F-actin dispersion and circularity as well as F-actin dispersion and area.

These plots are output from the multivariate mixed effects model. They demonstrate the relationship between expected force (y-axis) and the x-axis variable change when another variable is average (green line), high (blue line), or low (red line). Slope differences in these green, blue, and red lines indicate how one variable changing alters the relationship between force and the x-axis variable. (A) For average circularity (circularity = 0.557, green line), the relationship between expected force and area is positive with a slope of 0.410 nN/μm^2. If circularity is one standard deviation above average (circularity = 0.754, blue line), the force-area relationship has a slope of 0.387 nN/μm^2. If circularity is one standard deviation below average (circularity = 0.360, red line), the force-area relationship has a slope of 0.433 nN/μm^2. The interaction between area and circularity is not significant (p = 0.2128) (B) For average area (area = 43.6 μm^2, green line), the relationship between expected force and circularity is positive with a slope of 6.87 nN/1 circularity unit. If area is one standard deviation above average (area = 66.0 μm^2, blue line), the force-circularity relationship has a slope of 4.25 nN/1 circularity unit. If area is one standard deviation below average (area = 21.1 μm^2, red line), the force-circularity relationship has a slope of 9.50 nN/1 circularity unit. The interaction between area and circularity is not significant (p = 0.2128) (C) For average F-actin dispersion (F-actin dispersion = 0.592, blue line), the relationship between expected force and area is positive with a slope of 0.410 nN/μm^2. If F-actin dispersion is one standard deviation above average (F-actin dispersion = 0.811, blue line), the force-area relationship has a slope of 0.464 nN/μm^2. If F-actin dispersion is one standard deviation below average (circularity = 0.372, red line), the force-area relationship has a slope of 0.356 nN/μm^2. The interaction between area and F-actin dispersion is significant (p = 0.0029). (D) For average area (area = 43.6 μm^2, green line), the relationship between expected force and F-actin dispersion is positive with a slope of 14.9 nN/1 F-actin dispersion unit. If area is one standard deviation above average (area = 66.0 μm^2, blue line), the force-F-actin dispersion relationship has a slope of 20.4 nN/1 circularity unit. If area is one standard deviation below average (area = 21.1 μm^2, red line), the force-F-actin dispersion relationship has a slope of 9.4 nN/1 F-actin dispersion unit. This interaction between area and F-actin dispersion is significant (p = 0.0029). (E) For average F-actin dispersion (F-actin dispersion = 0.592, blue line), the relationship between expected force and circularity is positive with a slope of 6.87 nN/1 circularity unit. If F-actin dispersion is one standard deviation above average (F-actin dispersion = 0.811, blue line), the force-circularity relationship has a slope of 12.1 nN/1 circularity unit. If F-actin dispersion is one standard deviation below average (circularity = 0.372, red line), the force-circularity relationship has a slope of 1.7 nN/1 circularity unit The interaction between circularity and F-actin dispersion is significant (p = 0.0150). (F) For average circularity (circularity = 0.557, green line), the relationship between expected force and F-actin dispersion is positive with a slope of 14.9 nN/1 F-actin dispersion unit. If circularity is one standard deviation above average (circularity = 0.754, blue line), the force-F-actin dispersion relationship has a slope of 19.5 nN/1 unity of F-actin dispersion. If circularity is one standard deviation below average (circularity = 0.360, red line), the force-F-actin dispersion relationship has a slope of 10.2 nN/1 unit of F-actin dispersion. The interaction between circularity and F-actin dispersion is significant (p = 0.0150).

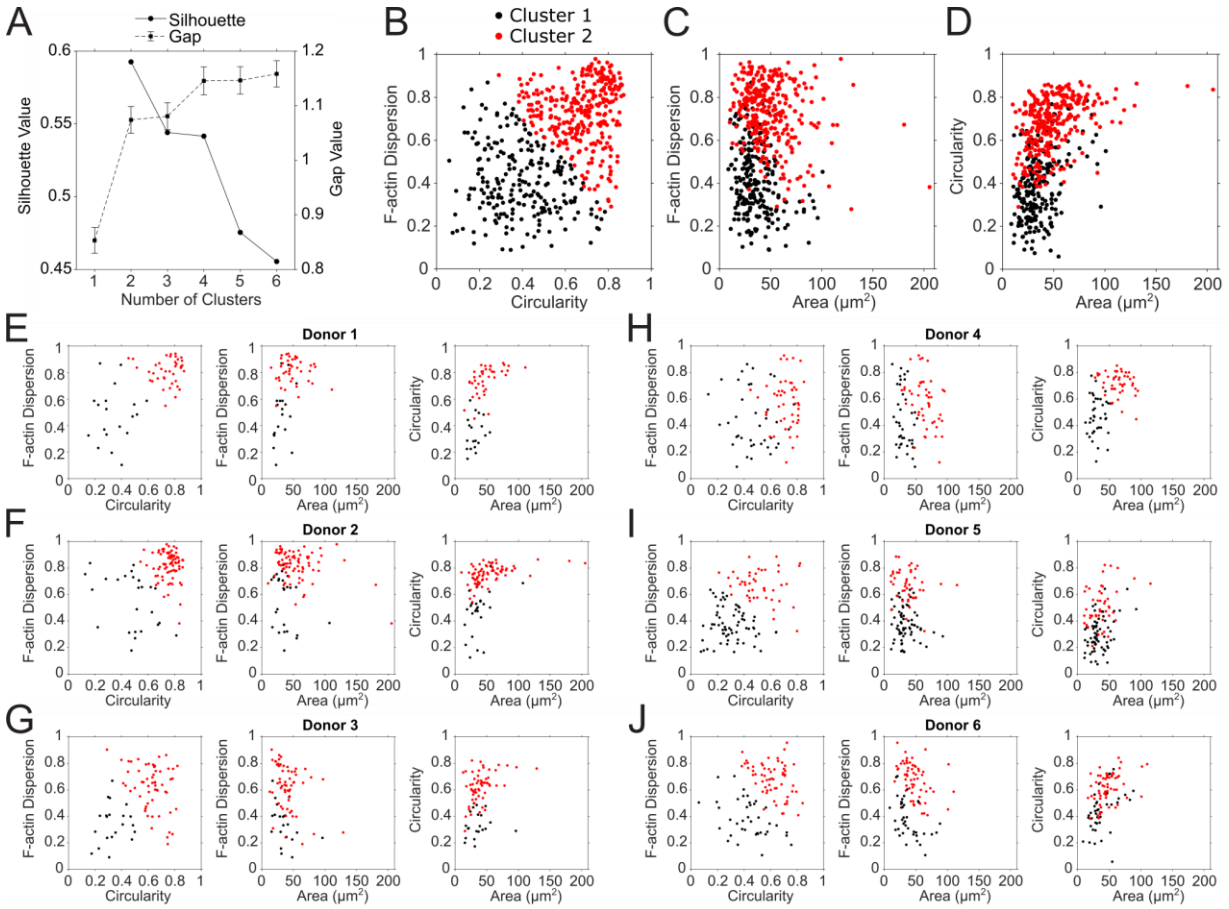

Figure 20 – K-means clustering for each donor.
(A) Silhouette and gap values used to determine the optimal number of clusters. For silhouette, the highest value determines the optimal number of clusters. For gap, the optimal number of clusters is the lowest number where the gap value of the next highest number is within the error of the previous one. In this case, both methods indicate that 2 clusters is optimal. (B, C, D) Same data as shown in the main text Figure 5A, B, and C, except the area axis shows all data points. (E-J) Relationships between area, circularity, and F-actin dispersion for all 6 donors. Here, K-means clustering was performed on each donor separately and generally shows that the platelets separate into two similar clusters for each donor.

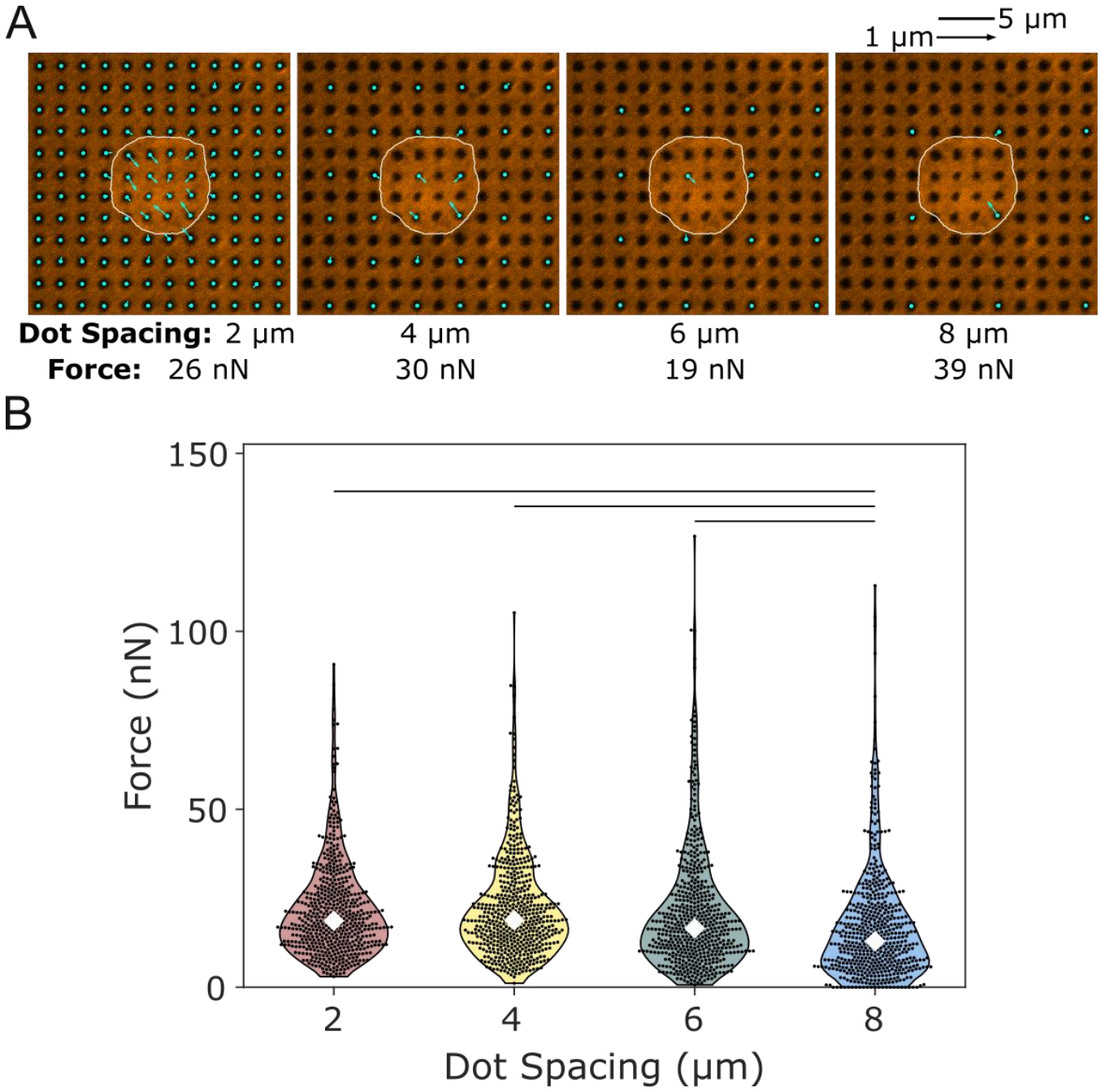

Figure 21 – Effect of pattern size on force estimation.
(A) Example of a platelet with displacement vectors with different pattern spacing simulated by skipping dots. For example, using data from every other dot simulates a pattern spacing of approximately 4 µm. Total force estimated for each pattern spacing is shown underneath each image. (B) Forces from all platelets for different dot spacing, n = 540. For dot spacing of 8 µm, several platelets exhibit no force likely because the dot spacing is too large. Lines indicate significant differences in forces ($p < 0.05$ when tested with paired t-tests).

3.7 Acknowledgements

This work was supported by the National Science Foundation (CMMI-1661730, CMMI-1824792), the National Institutes of Health (EB001650, HL147462, HL149734, GM135806, AR074990, TR003519, DE029827), and the Institute for Stem Cell and Regenerative Medicine Fellows Program. Imaging in this study was completed in the Lynn & Mike Garvey Imaging Core with the helpful guidance of Dale Hailey. The Department of Biostatistics Statistical Consulting Services and Prof. Megan Othus assisted with the statistical analysis for this study. We would also like to thank Robin Zhexuan Yan, Kenia Diaz, Francisco Morales, and Anabela Soto for their assistance testing the robustness of black dot manufacturing and/or the usability of the black dot analysis code.

3.8 Author contributions

This chapter is a manuscript published in *Acta Biomaterialia* in 2021 with authors Kevin M. Beussman*, Molly Y. Mollica*, Andrea Leonard, Jeffrey Miles, John Hocter, Zizhen Song, Moritz Stolla, Sangyoon J. Han, Ashley Emery, Wendy E. Thomas, Nathan J. Sniadecki. *equal contribution.

K.M.B. and M.Y.M. contributed equally to this study. K.M.B., A.L., and N.J.S. conceived of the black dot method. K.M.B., M.Y.M., and A.L. optimized the black dot method. J.M. recruited blood donors, collected, and washed platelets. M.Y.M. performed the platelet force assay. K.M.B., S.J.H., A.H., and N.J.S. determined the model to calculate force from black dot displacement. K.M.B. primarily wrote the analysis code, with contributions from M.Y.M. and Z.S.. M.Y.M. and K.M.B. analyzed the images, plotted the data, and made the figures. J.H., M.Y.M., and K.M.B. conducted the statistical analyses. K.M.B, M.Y.M., W.E.T., and N.J.S. designed the experiments, interpreted the data, and wrote the manuscript. All authors reviewed and edited the manuscript.

Chapter IV: Forces of Stored Platelets

4.1 Introduction

Platelets are transfused to prevent and treat bleeding. Standard platelet storage is limited to 5-7 days at room temperature (20-24°C, RT) to limit the risk of sepsis.[118,119] As a consequence, they require additional labor and costs due to bacterial testing, logistical issues with maintaining an adequate supply, and shortages.

Cold-stored platelets (1-6°C, CSP) were the standard of care in the 1960s and 1970s but were abandoned because the circulation time is severely shortened. Nevertheless, storage of platelets at 4°C has potential advantages including prolonging storage times, preventing bacterial growth, and easier transport and storage. Despite the short circulation time, CSP could be beneficial for actively bleeding trauma or surgery patients, thereby improving the availability of RT-stored platelets (RSP) for hematology and oncology patients. Numerous studies of CSP show better in vitro function than RSP in a wide range of assays.[120–128] Cold exposure also elicits changes to the platelet cytoskeleton, such as actin filament barbed end capping, actin polymerization, and *de novo* nucleation.[129] Increased cytosolic calcium and microtubule disintegration accompany the cytoskeletal changes.[130] Despite decades of studies on the function of cold-stored platelets, it remains unclear whether cold-stored platelets generate forces on the single-cell scale and whether these forces are comparable to RT-stored or fresh platelets.

4.2 Methods

4.2.1 Platelet collection and storage

Apheresis platelets were collected from healthy donors using the Trima Accel Automated Blood Collection System (Terumo BCT, Denver, CO) and stored in ACD-A and plasma. The target platelet yield was 4.5-6.3 X 10^{11}/unit depending on donor's baseline platelet count, and target concentration of ~1.5 x 10^{6} platelets/µL. Each unit had platelet concentrations and volumes within acceptable bag parameters.

Platelets were tested on the day of collection (day 0) and after five days of storage (day 5) at 4 °C without agitation or 22 °C/room temperature (RT) with agitation. On the day of testing and transfusion, the units were allowed to equilibrate to room temperature for one hour before we took a sample for testing. Units were inverted but not otherwise manipulated (e.g., massaged or shaken).

4.2.2 Whole blood collection and preparation for the multi-platelet force assay

On day 0 and on day 5, whole blood was collected from the same healthy donor in 3.2% sodium citrate. Fresh red blood cells (RBCs) with plasma was prepared by centrifuging whole blood at 200 g for 10 minutes and removing the platelet poor plasma (PPP) and buffy coat. After running an RBC fraction on Horiba ABX (Horiba, Kyoto, Japan), fresh RBCs were diluted with PPP to a hematocrit of 57% to yield thrombocytopenic whole blood. Apheresis PRP was diluted to 10^6/µL using PPP derived from the same sample to ensure a consistent platelet count.

4.2.3 Preparation of washed platelets after storage for the single-platelet force assay

Investigation of washed platelets after storage required developing a new protocol based on previously published methods[104,131] Platelets were isolated from plasma by centrifugation. Platelets were pelleted at 1000 g and resuspended in HEN Buffer (10 mM HEPES, 1 mM EDTA, 150 mM NaCl, 6.5 pH) supplemented with 0.5 µM prostacyclin (PGI2). A 10 minute, incubation step at RT helped prevent activation before repeat treatment with 0.5 µM PGI2 and centrifugation at 800 g. Platelets were resuspended and diluted to 3 x 10^8 platelets/mL with modified Tyrode's buffer (137 mmol/L NaCl, 2 mmol/L KCl, 12 mmol/L $NaHCO_3$, 0.3 mmol/L NaH_2PO_4, 1 mmol/L $MgCl_2$, 2 mmol/L $CaCl_2$, 5.5 mmol/L glucose, 5 mmol/L HEPES, 0.35% (w/v) human serum albumin, 7.3 pH) supplemented with 0.02 U/mL apyrase.

4.2.4 Multi-platelet (block and post) force assay

Platelets were removed from whole blood by centrifugation. PPP derived from fresh whole blood was used to dilute the RBC rich sample fraction to yield thrombocytopenic blood. Apheresis PRP from fresh (on day

0) or stored (on day 5 after storage at 4 °C or RT) was added to yield a final target of hematocrit of 40% and platelet count of 3 x 10^5/μL.

Reconstituted blood was perfused through a microfluidic channel made with polydimethylsiloxane (PDMS, Sylgard 184) with embedded microscale blocks and microposts to monitor platelet aggregation and production of multi-platelet contractile forces. Prior to testing, the microchannel were incubated with rat tail collagen type I (200 μg/mL, BD Bioscience) in 0.1 M acetic acid to support the adhesion and activation of platelets. For testing, a blood sample was flowed through the microfluidic device at a shear rate of 16,000 s^{-1} using a syringe pump (Harvard Apparatus). Platelets within the blood sample attached initially to the blocks and then aggregated to form platelet-rich plugs that bridged the 9 μm gap with each post. After 15 seconds of flow, the shear rate decreased to 500 s^{-1} to reduce the rate of aggregation and avoid occluding the microchannel with platelets.

The size of the aggregates and deflection of the post due to platelet forces were recorded every 2 seconds over a period of 5 minutes using phase and fluorescent time-lapse images obtained on a Nikon Eclipse Ti-E inverted microscope with a 40X objective. The images were then quantified post-experiment using custom MATLAB scripts. The force that aggregated platelets produced was calculated using Hooke's law, $F = k\delta$ where F is force, δ is post deflection, $k = 3\pi Ed^4/64L^3$, where E = 2.26 MPa is the modulus of elasticity of PDMS baked at 110 °C for 18 hours, d = 6.1 μm is the diameter of the post, and L = 25 μm is the length of the post. On day 5 of storage, this protocol was repeated with fresh thrombocytopenic whole blood derived from the same donor and PRP from apheresis platelets stored at room temperature or 4 °C.

4.2.5 Single-platelet (black dots) force methodology

Washed apheresis platelets on day 0, day 5 after 4 °C storage, or day 5 after RT storage were diluted in Tyrode's buffer and were seeded at 2.5 x 10^7 platelets/mL onto VWF-coated black dots and at 5 x 10^7 platelets/mL onto fibrinogen-coated black dots to ensure there was separation between the platelets. After 10 minutes of incubation to allow for platelet adhesion, the black dots were gently rinsed with PBS to

remove the unbound platelets. The substrates were then submerged into fresh Tyrode's buffer for 30 minutes to allow platelets to spread and generate traction forces. Platelets on the black dots were fixed with 4% paraformaldehyde for 20 minutes and permeabilized with 0.1% Triton X-100 for 20 minutes. Platelet GPIb was labeled with a CD42b monoclonal antibody, clone SZ2 (Life Technologies), and a goat anti-mouse IgG secondary antibody (Life Technologies). Platelet F-actin was labeled with phalloidin (Life Technologies). Black dots were mounted onto glass coverslips using Fluoromount-G mounting medium (Invitrogen) and imaged with confocal microscopy using a Nikon A1R confocal microscope and a 60x oil objective. Single platelet traction forces were calculated from black dot displacement using regularized Fourier Transform Traction Cytometry. Single platelet forces were measured on N=6 donors on VWF and N=5 donors on fibrinogen. For each donor, each black dot-treatment (VWF and fibrinogen), and each condition (fresh on day 0, 4 °C-stored on day 5, and RT-stored on day 5), an average of n = 88 platelets were measured for a total of n = 2,905 platelets included in this study.

Methods to obtain and wash platelets, manufacture black dots, seed platelets onto black dots, etc. were described in detail in Chapter III. Briefly, a polydimethylsiloxane (PDMS) stamp for microcontact printing was create by casting Sylgard 184 (prepared at a 10:1 ratio) against a silicon master with an array of circular features arranged in an orthogonal lattice. A solution of 2.5 µg/mL Alexa-Fluor 594-conjugated bovine serum albumin (BSA) was pipetted onto the PDMS stamps' surface and allowed to adsorb for one hour. The stamp was then brought into contact with a polyvinyl alcohol (PVA) film to transfer the fluorescent BSA pattern onto the film. Subsequently, the PVA film was applied to a PDMS substrate's surface made with 95% of Sylgard 527 (prepared at a 1:1 ratio) and 5% of Sylgard 184 (prepared at a 10:1 ratio), which produced substrates with a stiffness of 12 kPa. The process of microcontact printing resulted in a flexible substrate with a contiguous fluorescent coating containing an orthogonal array of circular regions that were 1 µm in diameter, 2 µm in spacing, and lacked fluorescence (termed "black dots"). The substrates with black dots were treated with 5 µg/mL VWF (Haematologic Technologies) or 5 mg/mL fibrinogen (Sigma Aldrich) for one hour at RT to promote platelet adhesion.

4.3 Results

4.3.1 Multi-platelet aggregation and force generation

To test what effects platelet storage have on multi-platelet binding and contraction, we utilized a microfluidic, collagen-coated block and post assay to quantify aggregation and contractile force (Figure 22). In this assay, platelets in a small sample of blood are stimulated to attach and aggregate to form a platelet-rich plug by a local gradient in the shear rate caused by the block and post. Within a few seconds, a plug is typically large enough to bridge the gap between the block and post, and hence, the contractile force produced by the platelets can be measured by how far the post is deflected towards the block (Figure 22A). We stored platelets collected by apheresis for five days at RT, as per current clinical practice, or at 4 °C and added them to freshly-drawn RBCs and plasma to reconstitute a whole blood sample. Stored platelets reconstituted in fresh platelet-depleted blood samples adhered readily to the block and post and generated contractile forces that were statistically comparable to samples with freshly-drawn platelet rich plasma or RT-stored platelets (Figure 22B-E). Platelets stored at 4 °C formed significantly larger aggregates than platelets stored at RT at the early time point (60 seconds) (Figure 22B, F-G). However, after 300 seconds, the size of the 4 °C-stored aggregates decreased and were statistically similar to RT-stored (Figure 22B,H). RT-stored samples formed consistently smaller aggregates over time than those from fresh blood samples, and the difference between RSP and fresh was significant at 300 seconds (Figure 22B,H). Platelets stored at 4 °C formed larger aggregates after 60 seconds (Figure 22G), but this did not increase multi-platelet force generation (Figure 22D), suggesting individual 4 °C-stored platelet may generate lower forces per platelet.

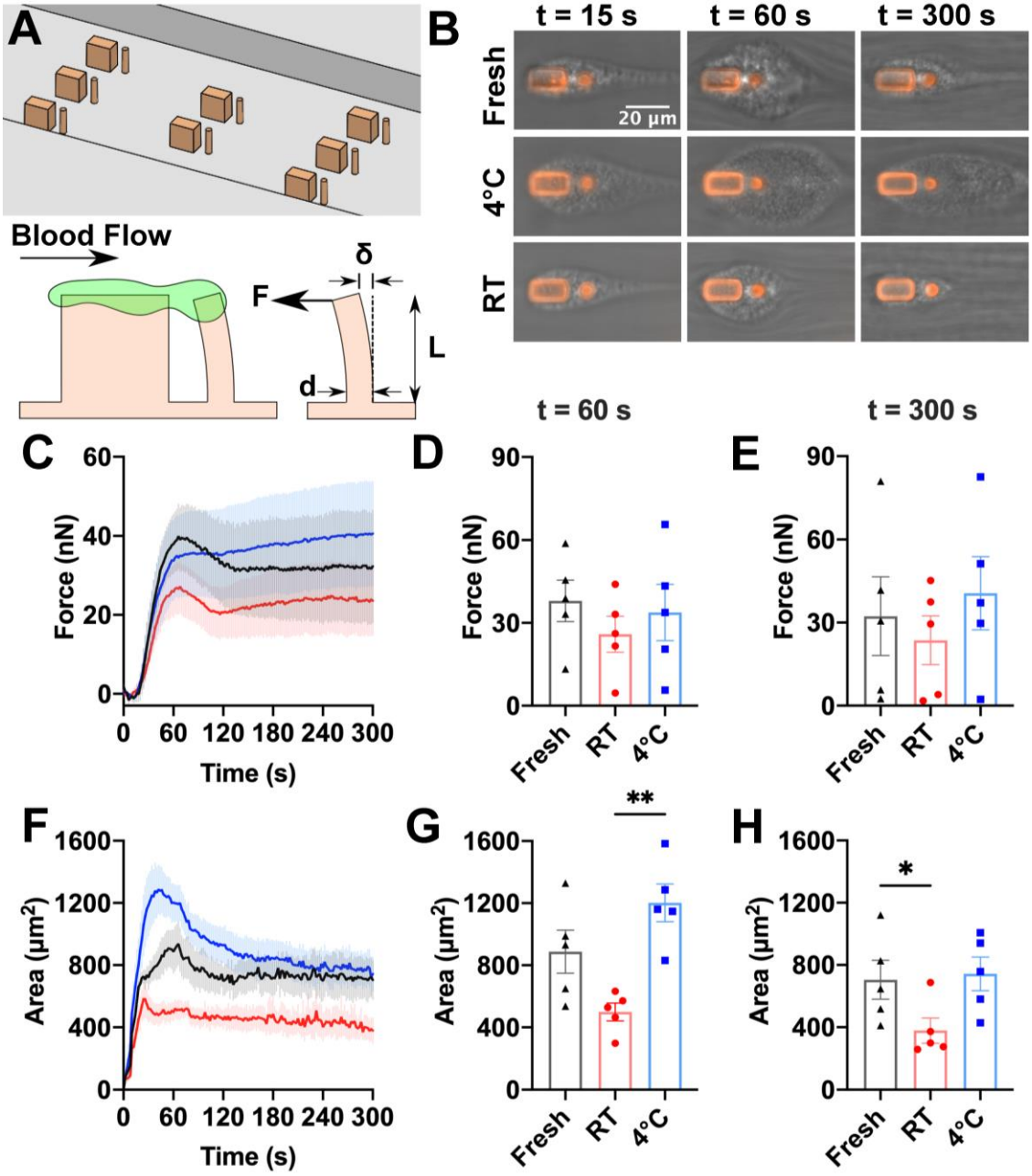

Figure 22 – Platelet aggregate force and area in response to shear flow.
Reconstituted whole blood samples with fresh (black triangle), RT-stored (red circles), or 4°C-stored apheresis platelets were perfused through a microfluidic device to measure the force and area of platelet aggregates formed under shear flow. (***A***) Each microfluidic channel contains multiple sets of block and post force sensors. While under flow, platelets attach and aggregate to form a plug-like structure (green) that encapsulates the block and post. Aggregated platelets are able to produce contractile forces (F) that pull the flexible post towards the rigid block. Force is calculated from displacement of the tip of the post (δ) using Hooke's law: $F = k\,\delta$, where $k = 3\pi\,E\,d^4 / 64\,L^3$, and E is the modulus of elasticity, d is the diameter, and L is the length of the post. (***B***) Representative images of platelet aggregate area 15 sec, 60 sec, and 300 sec after blood enters the channel. (***C***) Mean force of the platelet aggregates over time. N = 5, shaded regions represent SEM. (***D***) Force of the platelet aggregates at 60 seconds shown as the mean ± SEM (N = 5). (***E***) Force of the platelet aggregates at 300 seconds shown as the mean ± SEM (N = 5). (***F***) Mean area of the platelet aggregates overtime. N = 5, shaded regions represent SEM (***G***) Area of the platelet aggregates at 60 seconds shown as the mean ± SEM. N = 5, **p = 0.0032 for 4 °C and RT. (***H***) Area of the platelet aggregates at 300 seconds shown as the mean ± SEM. N = 5, and *p = 0.0103 for fresh and RT.

4.3.2 Single-platelet spreading and force generation

To further evaluate whether individual stored platelets generate significantly different forces, black dots were used to measure single-platelet contractile traction forces (Figure 23). Similar to what was observed in the multi-platelet force measurement, individual platelet forces on VWF or fibrinogen-black dots were statistically similar between freshly-drawn platelets, RT-stored platelets, or 4 °C-stored platelets (Figure 23B-C, E-F). These results indicated that the contractile function of platelets might be independent of the storage condition over five days of storage. We noted that traction forces for freshly-drawn platelets, RT-stored, or 4 °C-stored were more than two-fold higher on VWF-coating versus fibrinogen-coating.

To investigate whether the variation in aggregate size by condition observed in the block and post assay is due to differences in single-platelet spreading, single-platelet spread area was measured for each condition. Platelet spread area on VWF or fibrinogen-black dots were statistically similar between freshly-drawn platelets, RT-stored platelets, or 4 °C-stored platelets.

Taken together, from these results, we concluded that a) 4 °C-stored platelets have a higher propensity for shear-induced aggregation than RT-stored platelets and that b) 4 °C-stored platelets can generate similar contractile forces as freshly-drawn platelets and RT-stored platelets.

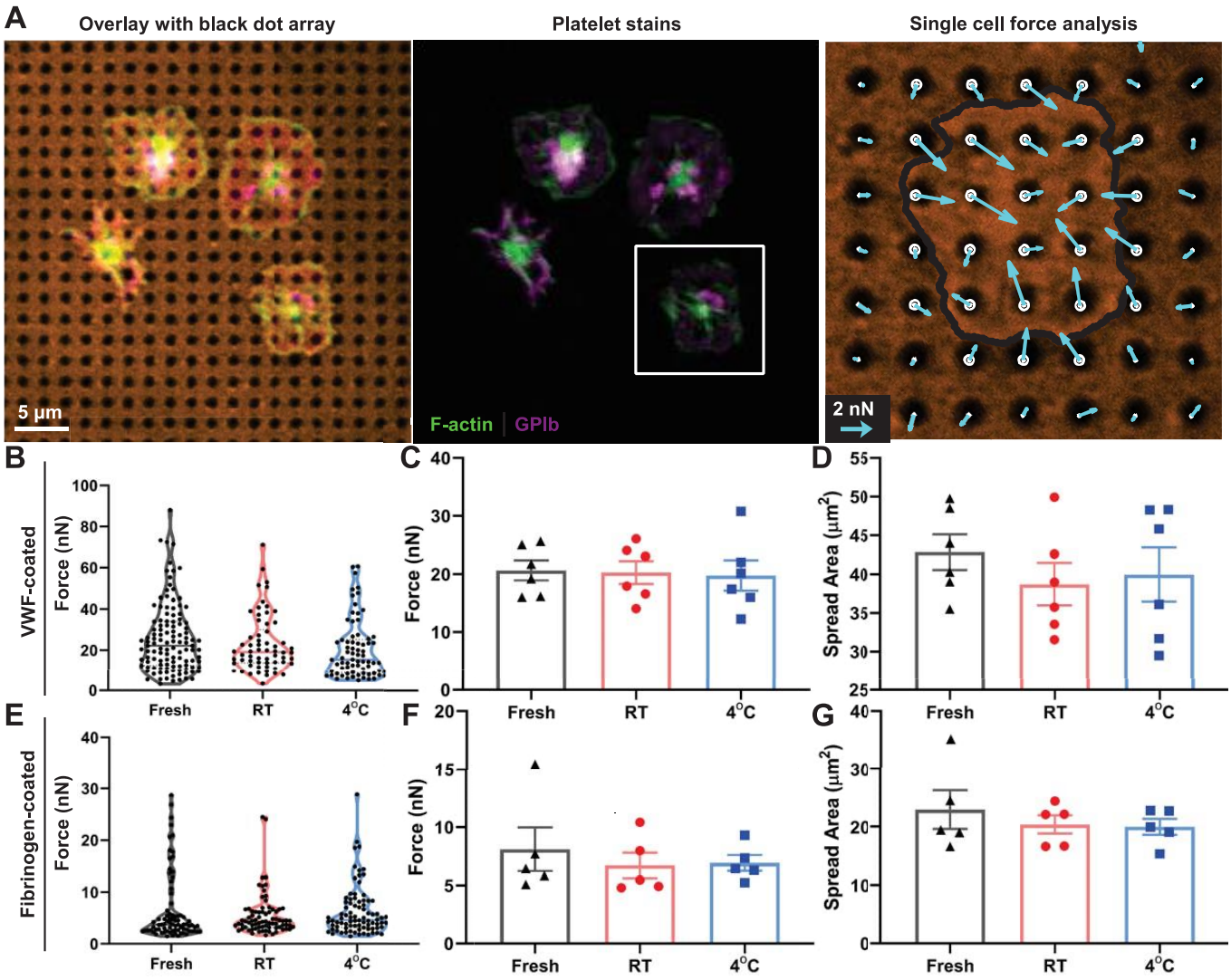

Figure 23 – Single-platelet forces of stored platelets.
Apheresis platelets were washed and seeded onto black dots to measure traction forces and spread area of individual platelets. ***(A)*** Platelets on the black dots (orange) were fixed, stained, and imaged to visualize F-actin (green) and glycoprotein Ib (GPIb) (purple). The magnitude and direction of platelet traction forces (blue arrows) were calculated from the displacements of the dots. ***(B)*** Traction forces were measured for fresh (gray), RT-stored (red), and 4 °C-stored (blue) platelets that were seeded onto black dot substrates coated with VWF. Violin plots show data from a representative donor for which 252 platelets were measured (117 fresh, 73 RT-stored, 62 4 °C-stored). ***(C)*** Average traction forces per platelet was measured for six donors and no statistically significant difference was observed between fresh (black triangles), RT-stored (red circles), and 4 °C-stored (blue squares). ***(D)*** Average spread area of platelets on VWF-coated black dots was measured for each donor and no significant difference was observed between the conditions. ***(E)*** Traction forces were measured for fresh (gray), RT-stored (red), and 4 °C-stored (blue) platelets on fibrinogen-coated black dots. Violin plots show data from a representative donor for which 242 platelets were measured (81 fresh, 84 RT-stored, 77 4 °C-stored). ***(F)*** Average traction forces and (***G***) average spread area of platelets on fibrinogen-coated back dots was measured for five donors and no significant difference was observed between conditions.

4.4 Discussion

Storage of apheresis platelets at 4 °C would reduce bacterial growth, thereby increase the infection risk-limited storage time. Increased platelet storage time would increase access, reduce costs, and assist in limiting platelet shortages. While 4 °C-stored platelets were abandon due to shortened circulation time, they may be beneficial in actively bleeding trauma or surgery platelets.

Our study is the first to assess multi-platelet and single-platelet force generation of stored platelets. Platelets stored at 4 °C for five days showed increased aggregation, but not significantly different multi-platelet force generation, single-platelet force generation, or single-platelet spread area compared to freshly collected platelets or platelets stored at RT for five days.

Ultimately, these force data data support the potential use of 4 °C-stored platelets clinically. Importantly, clinical trials are required to test the efficacy.

4.5 Author contributions

This chapter is a portion of a manuscript published in *Blood Advances* in 2021 with authors Jeffrey Miles, S. Lawrence Bailey, Ava M. Obenaus, Molly Y. Mollica, Chomkan Usaneerungrueng, Daire Byrne, Lydia Fang, Jake R. Flynn, Jill Corson, Barbara Osborne, Katie Houck, Yi Wang, Yu Shen, Xiaoyun Fu, Jing-Fei Dong, Nathan J. Sniadecki, and Moritz Stolla.

Additionally, J.M. recruited subjects, performed apheresis collections, and washed platelets for this study. A.O. and J.R.F. performed the block and post experiments, analyzed the data, and wrote the block and post results. M.Y.M. performed the black dot experiments, analyzed the data, and wrote the black dots results.

Chapter V: Cytoskeletal Morphology and Force of Platelets on VWF versus Fibrinogen

5.1 Introduction

Blood contacting medical devices can trigger thrombosis mediated by biomaterial-adsorbed blood proteins that induce platelet activation. Fibrinogen and von Willebrand Factor (VWF) are key blood proteins each independently capable of mediating platelet activation and binding to integrin $\alpha_{IIb}\beta_3$, and VWF additionally binds to platelets through glycoprotein Ib (GPIb). To stop bleeding after an injury, VWF mediates initial platelet binding to the subendothelium, while fibrinogen mediates platelet-to-platelet interactions as the platelet plug forms on the injury site. Blood contacting medical devices can trigger thrombosis mediated by biomaterial-adsorbed blood proteins that induce platelet activation. Fibrinogen and von Willebrand Factor (VWF) are key blood proteins each independently capable of mediating platelet activation and binding to integrin $\alpha_{IIb}\beta_3$, and VWF additionally binds to platelets through glycoprotein Ib (GPIb). To stop bleeding after an injury, VWF mediates initial platelet binding to the subendothelium, while fibrinogen mediates platelet-to-platelet interactions as the platelet plug forms on the injury site. Upon binding to a surface, the platelet actin cytoskeleton drives platelet spreading and contraction. Platelets adhere to surfaces as 2-5 μm diameter discoids, rapidly (~10 minutes) increase their spread area ~5-fold, and generate traction forces[7,20]. On fibrinogen, early bound platelets form punctate, actin-rich structures called actin nodules. In fully spread, fibrinogen-bound platelets, actin nodules rearrange into actin filaments localized at the platelet periphery, with a prominent absence of actin in the platelet center[12,20] (Figure 24A-D). In the few existing studies of platelets on surface-bound VWF, there appear to be notable differences in F-actin morphology wherein there is 1) an absence of actin nodules in early spreading and 2) an inverse of F-actin localization in spread platelets in which F-actin is localized centrally (Figure 24E-G). To our knowledge, this substantial difference in F-actin morphology on fibrinogen versus VWF has never been measured and compared directly, nor discussed in the literature.

Differences in cytoskeletal morphology may yield functional differences in force generation because cell forces are generated through actin-myosin interactions and because F-actin quantity and localization have been previously shown to correlate with platelet force generation[2,132]. A recent study found that VWF-bound platelets produced more than double the force of fibrinogen-bound platelets[133]. This interestingly suggests that GPIb involvement may mediate significant differences in force generation, but this study was storage conditions-focused and noted this difference without investigating the mechanism, accounting for differences in platelet spreading, or relating force generation with F-actin morphology.

Here, we directly compare platelet F-actin morphology on fibrinogen or VWF-adsorbed surfaces and observe that platelets on VWF form centralized F-actin morphology distinct from actin nodules and hollow F-actin morphology characteristic of platelets on fibrinogen. In addition to yielding a difference in F-actin

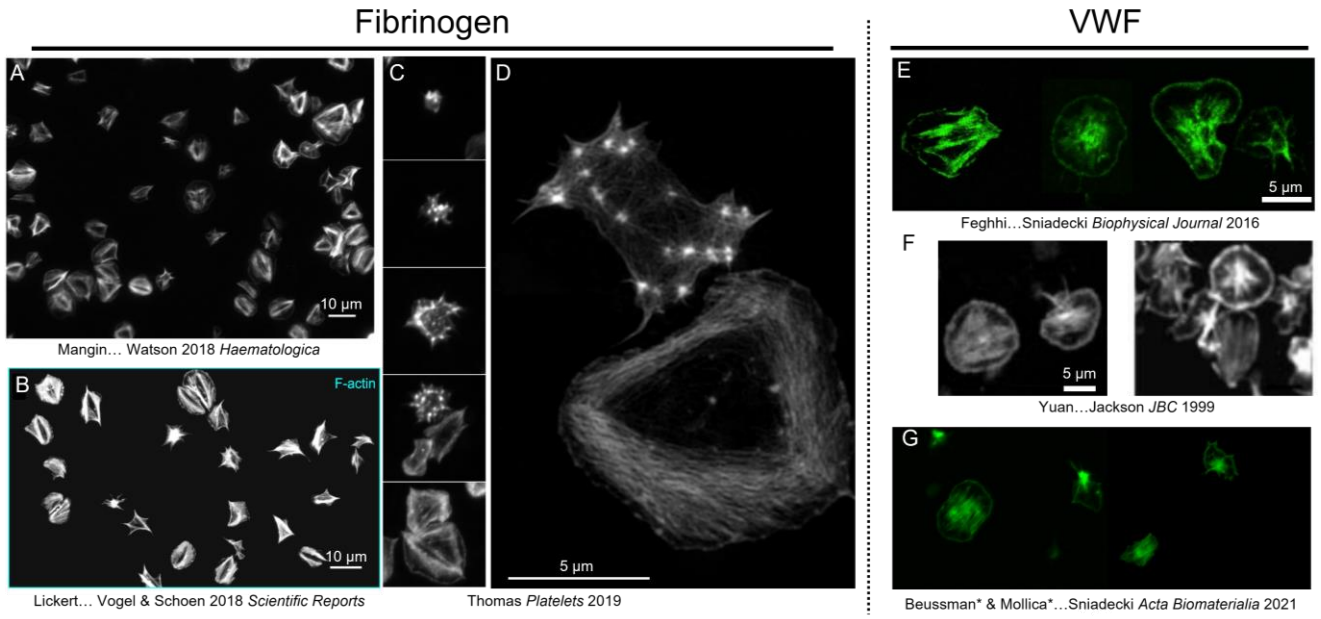

Figure 24 – From the literature: platelet F-actin morphology on fibrinogen and VWF.
(A-D) Platelets seeded and allowed to spread on fibrinogen often have their F-actin in a hollow structure. (C) Platelets spreading on fibrinogen (from top to bottom of panel C) often have punctate F-actin nodules. (D) Structured Illumination Microscopy show the F-actin of a platelet with F-actin nodules (top) and a hollow platelet (bottom) in high-resolution. (E-F) Platelets seeded and allowed to spread on VWF do not commonly have F-actin nodules or hollow platelets. A is from [143], B is from [10], C and D are from [20], E is from [5], F is from [21], and G is from[132].

morphology, we find that platelet force generation is surface protein-dependent, with highest forces generated by platelets on VWF.

5.2 Methods

5.2.1 Blood collection

Washed platelets used in this study were either collected by apheresis or were collected into ACD A tubes as whole blood. When collected by apheresis, they were washed as described in Chapter III. When collected from whole blood, whole blood was centrifuged at 200 g for 20 minutes. Platelet rich plasma was transferred to a fresh tube and centrifuges for at 1000 g for 10 minutes. The platelet pellet was washed in CGS buffer (120 mM NaCl, 13 mM sodium citrate, and 30 mM glucose, pH = 7, filtered with 0.22 μm filter) and platelets centrifuged again at 1000 g for 10 minutes. All centrifugation steps were conducted at room temperature with a brake of 1 and acceleration of 4. Washed platelets were resuspended in Tyrode's buffer (10 mm HEPES, 138 mM NaCl, 5.5 mM glucose, 12 mM $NaHCO_3$, 0.36 mM Na_2HPO_4, 2.9 mM KCl, 0.4 mM $MgCl_2$, 0.8 mM $CaCl_2$, pH = 7.5, filtered with 0.22 μm filter).

5.2.2 Seeding platelets onto fibrinogen or VWF-treated coverslips

Human VWF (Haematologic Technologies) was diluted to 5 μg/mL and incubated glass slides or black dots for 1 hour at room temperature. Human fibrinogen (Sigma) was diluted to 5 mg/mL and incubated on glass slides or black dots for 1 hour at room temperature. Platelets were diluted to half of their physiological concentration before and were seeded onto coverslips treated with either fibrinogen or VWF. Platelets were incubated for 10 minutes, gently rinsed in PBS to remove unbound platelets, and allowed to spread and contract in Tyrode's buffer for 0-90 minutes before fixing.

5.2.3 Black dots methodology

As previously described[132,133], microcontact printing was used to deposit a fluorescent surface with a pattern of non-fluorescent circles onto a flexible, polydimethylsiloxane (PDMS) surface. Briefly, a PDMS microcontact printing stamp was created by casting Sylgard 184 (prepared at a 10:1 ratio) onto a silicon

master structure with an array of circular features arranged in an orthogonal lattice. Fluorescent-bovine serum albumin (BSA) (2.5 µg/mL of Alexa Fluor 594-conjugated) was pipetted onto the PDMS stamps' surface and allowed to adsorb for 40 minutes. The stamp was then brought into contact with a plasma-treated polyvinyl alcohol (PVA) film for 20 minutes to transfer the fluorescent BSA pattern onto the film. Subsequently, the PVA film was applied to a flexible PDMS substrate's surface for 20 minutes. The flexible PDMS substrate was made with 95% of Sylgard 527 (prepared at a 1:1 ratio) and 5% of Sylgard 184 (prepared at a 10:1 ratio), which produced substrates with a stiffness of 13.5 kPa. The process of microcontact printing resulted in a flexible substrate with a contiguous fluorescent coating containing an orthogonal array of circular regions that were 1 µm in diameter, 2 µm in spacing, and lacked fluorescence (termed “black dots”). The substrates with black dots were treated with 5 µg/mL VWF (Haematologic Technologies) or 5 mg/mL fibrinogen (Sigma Aldrich) for one hour at RT.

Washed platelets were seeded onto VWF or fibrinogen-coated black dots. After 10 minutes of incubation to allow for platelet adhesion, the black dots were gently rinsed with PBS to remove the unbound platelets. The substrates were then submerged into fresh Tyrode’s buffer for 30-80 minutes to allow platelets to spread and generate traction forces.

Single platelet forces were calculated from displacements of the black dot centroids using regularized Fourier Transform Traction Cytometry. Total force for a single platelet was calculated by summing the force magnitudes from each dot beneath a cell.

To enable higher resolution, subcellular localization of platelet forces, we measured displacements of the black dots using the shape of the deformed dots. In addition to measuring total platelet force from the displacements of black dot centroids, we measured higher resolution forces by fitting a least-squared elliptical fit to each of the deformed black dots. The fit was performed as follows: First, the local image contrast was normalized with a square structuring element of size 30 pixels (1.55 µm) to avoid microscopy vignette artifact and light intensity variation across dots. The region of interest (ROI) containing the platelets

with dots undergoing deformation was labelled as deformation region and the dots in the same image outside the ROI were labelled as reference region. The reference dots in each frame were binarized with the 'minimum' threshold method and the same threshold was applied to deformed region in that frame to maintain consistency. The least squares fit was performed using the 'Analyze Particles' toolbox in ImageJ with PyImageJ plugin. The undeformed state of the dots was modelled as a circle with radius obtained from averaged elliptical fit to the reference dots.

The affine transformation between a circle and an ellipse is not unique without the presence of discerning circumferential markers. Therefore, the displacement measurement was made as the vectorial difference between the vertices and co-vertices of the fitted ellipse along the principal axes of the deformed ellipse and the corresponding angular location on the undeformed circle.

The in-plane shear stresses exerted by the platelets on the top of an isotropic, elastic half-space was reconstructed using a Bayesian approach. To improve the resolution of the force localization within the cell, the traction stresses were reconstructed on a finer (6X resolved), uniform grid ($\bar{x}' \in \Omega$) given the displacement measurement with elliptical fit on a non-uniform grid ($\bar{x} \in \Omega_{\mathrm{dots}}$) as described above. Here, Ω_{dots} and Ω denote the displacement domain and the domain within the cell contour respectively. The Boussinesq solution in real space was used to relate the displacement field $\overline{U}(\bar{x})$ in a semi-infinite elastic gel as a convolution integral of traction stress field $\overline{T}(\bar{x}')$[134,135].

$$\overline{U} = \int_{\Omega} G(\bar{x} - \bar{x}')\, \overline{T}(\bar{x}')\, d\bar{x}' = \bar{\bar{G}}\, \overline{T}$$

Here $G(\bar{x} - \bar{x}')$ is the Boussinesq Green's function kernel. Inverting this equation is a highly ill-conditioned problem and the increase in the traction degrees of freedom result in an underdetermined problem. The traction forces were approximated to be constant within the uniform solution grid, while the singularity at origin in real space $G(\bar{x} - \bar{x}')$ is dealt with the use of non-collocated, denser grid as well as a truncated $\bar{\bar{G}}$ matrix.

A Bayesian approach building on previous work[135,136] was utilized to perform the traction stress inversion with informative priors. The likelihood distribution for the residual to the Boussinesq solution it was assumed to be distributed as a zero mean, multi-variate normal distribution with precision parameter β,

$$p(\bar{u}|\bar{t}) \propto \exp\left\{-\frac{\beta}{2}\left\|\bar{U} - \bar{\bar{G}}\,\bar{T}\right\|_2\right\}.$$

The following priors were used to elicit physically meaningful traction stresses: a) Regularization prior (R), b) Global force balance prior (B) and c) cell contour prior (C). The priors are modelled as zero-mean Gaussian distributions of the form,

$$p(\bar{T}_i|\alpha_i) \propto \alpha_i^{N_i} \exp\left\{-\frac{1}{2}\,\alpha_i S_i(\bar{T})\right\}.$$

Here, $i \in R, C, B$ each corresponding to the respective priors, N_i is the number of positive eigenvalues of $S_i(\bar{T})$ and α_i are the respective precision parameters. $S_i(\bar{T})$ is a non-negative quadratic loss function encoding the physical constraints. $S_R = \int_\Omega |\bar{T}(\bar{x}')|^2 d\bar{x}'$ is used to regularize the L-2 norm of the solution, $S_B = \left[\int_\Omega \bar{T}(\bar{x}')\, d\bar{x}'\right]^2$to enforce global force balance for isolated platelets, and $S_C = \left[\int_\Omega \mathbb{1}(\bar{x}' \notin \Omega)\, |\bar{T}(\bar{x}')|^2\, d\bar{x}'\right]$ to constrain cell-exerted forces within the cell spread area. The hyper-parameter set is denoted by $\bar{\theta} = \{\beta, \alpha_R, \alpha_B, \alpha_C\}$. The hierarchical Bayesian construction with improper hyper-priors on $\bar{\theta}$ was approximated as:

$$p(\bar{t}|\bar{u}) \propto \int p(\bar{u}\,|\bar{\theta}, \bar{t})\, p(\bar{t}\,|\bar{\theta})\, p(\bar{\theta}|\bar{u})\, d\bar{\theta} \approx p(\bar{u}|\hat{\theta}, \bar{t})\, p(\bar{t}|\hat{\theta}),$$

by assuming a sharply peaked $p(\bar{\theta}|\bar{u})$. We find the optimal hyper-parameters $\hat{\theta} = argmax_{\{\theta\}}\, p(\bar{\theta}|\bar{u})$ as a part of the stress reconstruction process by maximizing the evidence $p(\bar{\theta}|\bar{u})$[137]. This procedure can be interpreted as finding the hyper-parameters that balances the misfit to the Boussinesq equation with that of the level with which the priors are enforced. The final traction stress field is taken as the mode of $p(\bar{t}|\bar{u})$. The ability to automatically select the hyper-parameters for individual cells is necessary to avoid over-

smoothing or over-fitting as the stress magnitude, force localization, displacement noise level and the image quality fluctuates independently over different cells as well as different experimental conditions[135].

5.2.4 Fixing and immunofluorescent staining

Platelets on coverslips or slides were fixed with 4% paraformaldehyde for 20 minutes, permeabilized with 0.1% TritonX-100, and blocked with 10% goat serum for 1 hour. Platelets were stained for F-actin with phalloidin 405 (1:50 dilution) or phalloidin 488 (1:200 dilution). GPIb was labeled using a mouse anti-CD42b antibody (SZ2 clone, 1:100 dilution) and a goat anti-mouse secondary 647 antibody (1:200 dilution). All stains were diluted in 10% goat serum and incubated for 1 hour at room temperature. Samples were mounted using Fluoromount-G.

5.2.5 Imaging via confocal microscopy and structured illumination microscopy

Samples were imaged via confocal microscopy on a Nikon A1R with a 60X objective. Superresolution images were collected with a Zeiss Elyra 7 with Lattice Structured Illumination Microscopy and a 63X objective.

5.2.6 F-actin morphology assessment and machine learning

F-actin morphology was manually assigned (as containing nodules, hollow, or solid morphology) for each platelet. Nodule morphology is defined by containing more than one punctate F-actin assembly, hollow morphology is defined by F-actin being localized at the platelet periphery with a notable absence of F-actin in the platelet center, and solid morphology is defined by centralized and/or homogenously spread F-actin. If platelets exhibited features of multiple categories or if it was unclear which category, the platelet morphology was deemed indeterminable. Manually assessed data was used to train a machine learning model to classify platelet F-actin morphology in high yield without user bias.

To build the platelet image classifier, we used deep learning in the form of a convolutional neural network (ConvNet). We used Python 3.8.10 using TensorFlow 2.7.0 to apply transfer learning to the existing ConvNet *InceptionV3*, which is a model that has previously been shown to perform image classification

using ImageNet data with 1000 classes[138]. We modified the model by replacing the last 1000-class layer with a 3-class layer representing the three F-actin morphologies. A set of 1,598 manually classified platelet F-actin images was split into a training set (80% of images) and a validation set (20% of images). For the 1,280 images in the training set, 340 were hollow, 244 were nodules, and 696 were solid. For the 318 images in the validation set, 85 were hollow, 60 were nodules, and 173 were solid. This uneven class distribution was accounted for by applying a class weighting to the model (i.e. each nodules image can affect the model parameters more strongly than each solid image.) The raw images were cropped around the platelet and were reshaped to a standard 40-by-40 pixel image, compressing the image and allowing the model to be used for platelets of different sizes and images of different resolutions. The images were then normalized and contrast adjusted wherein the lowest 5% of pixels were given a value of 0, the highest 5% of pixels were given a value of 255, and all other pixels were given values between 0-255. The images were then input into *InceptionV3.*

The model was then trained in a series of epochs where in one epoch, each image in the training set is run through the model, its class is predicted by the model, and the model's weights are updated according to how "wrong" the model prediction is using backpropagation. The model weights are updated towards an optimal state following a gradient descent approach (SGD optimizer in TensorFlow), where the learning rate dictates how much the model weights can change in each step. To artificially increase the data set size, the training images are augmented for each epoch by applying a random assortment of: rotation (up to 45°), zoom (up to 10%), translation (up to 5%), and vertical and/or horizontal mirroring; in this way, the model is trained on a large set of images then actually input.

To start, only the final classification layer's model weights were allowed to change with the remaining layers of the *InceptionV3* model frozen. This classification layer was trained for 200 epochs with a learning rate that exponentially decreased from 10^{-2} to 10^{-4} over these 200 epochs. This learning rate approach allows the gradient descent algorithm to take larger steps in the first epochs when the model is poorly optimized, and smaller steps as the model reaches its convergent state. After the classification layer was trained, the

entire *InceptionV3* model was fine-tuned by unfreezing everything and training all the layers for another 200 epochs at a learning rate of 10^{-4}. The model was saved after each epoch if the validation loss (i.e. how far apart the model's predictions are from the true validation classes) decreased from the last saved model. This training was performed on University of Washington's high-performance computing cluster Hyak on a single graphics processor (GPU); GPUs are highly optimized for this training due to the high number of convolutions and matrix algebra.

During training, the model performance is evaluated by predicting the classes of the validation images. Unlike the training images, the validation images are not augmented and are meant to be similar to real images that the model will assess. Under the training scheme outlined here, the validation accuracy converged to 92.3% in the first 200 epochs, when only the final classification layer was allowed to change. After unfreezing all of the layers and training for another 200 epochs, to final model yielded a 97.6% validation accuracy.

5.3 Results

5.3.1 Platelet F-actin morphology differs on fibrinogen and von Willebrand Factor and observed morphologies are detectable via machine learning

After seeding platelets onto fibrinogen-treated or VWF-treated coverslips, we observe unique and significantly different F-actin morphology on each protein (Figure 25). On fibrinogen, there are a fraction of platelets with punctate nodules that are not observed on VWF (Figure 25A-C). Additionally, the majority of platelets on fibrinogen have actin filaments at the periphery with a prominent absence of actin in the platelet center (termed "hollow") (Figure 25A-C). On VWF, hollow platelets account for only 1% of platelets and instead, most platelets have an inverse F-actin morphology with F-actin localized centrally (termed "solid") (Figure 25A-C). To further characterize these F-actin morphologies, we used structured illumination microscopy to obtain superresolution images of each morphology (Figure 25C). After manually classifying the F-actin morphology of platelets on fibrinogen and VWF, we find that the frequencies of these

morphologies are significantly different when tested with a Pearson's Chi-squared ($p < 0.0001$) (Figure 25C). To reduce user bias and increase yield of future F-actin morphology categorizations, the manual classifications were used to train a machine learning model that has 97.6% accuracy, indicating that these unique F-actin morphologies are detectable by machine learning.

5.3.2 Platelets generate more force on VWF than on fibrinogen

Because the F-actin cytoskeleton drives platelet contraction and we previously found that F-actin dispersion throughout the cell significantly associates with force generation[132], we investigated whether the unique F-actin morphologies on VWF and fibrinogen result in differences in force generation. To measure single-platelet forces, we seeded platelets onto fibrinogen- or VWF-coated black dots (Figure 26A-B). Black dots are a fluorescent array with a pattern of non-fluorescent circular dots (hence "black dots") microcontact printed onto a flexible substrate[132]. When platelets bind, spread, and contract on the black dots, they displace the pattern; single-platelet forces are calculated from the displacements (Figure 26C). Black dots is a technique suitable for this study because unlike standard traction force microscopy and many reference-free techniques[94], it is compatable with immunofluorescent staining without constraining cell shape and size, making it possible to co-measure F-actin morphology and force on platelets allowed to spread on a contiguious adhesive surface. On fibrinogen- or VWF-coated black dots, F-actin morphology differences were consistent with those observed on glass coverslips (Figure 26A-B). For all donors, the average platelet force on VWF was higher than on FBN and these differences were significant after 40 minutes and 90 minutes on the substrate (Figure 26D). Additionally, platelets on VWF produce significantly more force per area than platelets on fibrinogen (Figure 26E), indicating that despite the well-established correlation between spread area and force[7,132], this observed difference in force generation is not simply a consequence of differences in spread area.

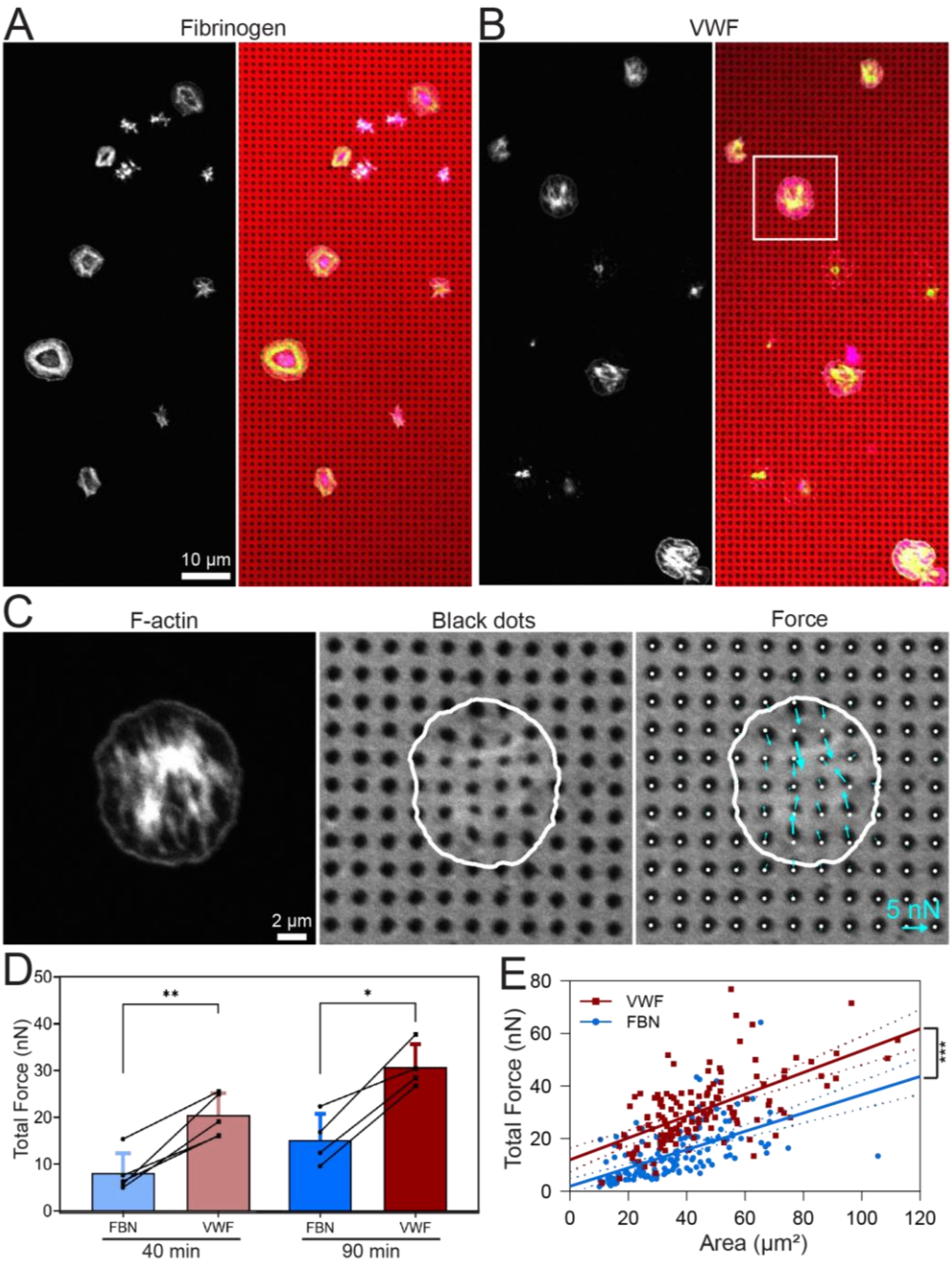

Figure 25 – Platelets on VWF produce more force and more force per area than platelets on fibrinogen.
(A-B) F-actin (white on monochromatic image, green on colorized image)-labeled platelets spreading on fibrinogen-coated black dots (A) or VWF-coated black dots (B). In colorized image, F-actin is green, GPIb is magenta, and black dot array is red. (C, inset white box from B) The dots underneath a platelet are deformed by forces generated by the platelet. Forces (blue arrows) are calculated from the displacement of the dots from their undeformed centroids (white dot). Cell boundary is shown in white in the middle and right panel. (D) Average total cell forces per donor are significantly higher on VWF than FBN at 40 minutes ($p < 0.01$ when tested with a paired t-test) and 90 mins ($p < 0.05$). Lines between dots indicate the same donor. Error bars are standard deviation. (E) Platelets on VWF produce more force per area than platelets on FBN. The best fit line of VWF (red) has a slope of 0.4152 and an intercept of 11.93. The best fit line of FBN (blue) has a slope of 0.3481 and an intercept of 1.87. Dotted lines are the 95% confidence interval. These intercepts are significantly different ($p < 0.001$) when tested with an analysis of covariance.

5.3.3 F-actin structure corresponds to subcellular force localization

In addition to total force generation per platelet, we additionally examined whether F-actin morphologies associate with subcellular localization of forces. To increase the resolution of the platelet forces in order to examine subcellular localization from the raw black dots image (Figure 27A), we made improvements to the analysis including 1) fitting ellipses to the deformed black dots (Figure 27B), which enables four displacement vectors (yellow arrows in Figure 27B) per black dot instead of one (blue arrows in Figure 27B), 2) taking the cell boundary into account (red line in Figure 27C-D) and assuming that forces exerted outside the cell boundary are zero, 3) requiring a force balance (net force = 0), and 4) adding evidence analysis for regularization. These techniques ultimately result in higher resolution platelet force mapping than all previous studies and the first co-measurement of F-actin with high-resolution force mapping (Figure 27C-D). We find that forces correspond to F-actin structure, are the highest at the ends of stress fibers, and are oriented parallel to the stress fibers (Figure 27C-D). The higher forces on solid, VWF-bound platelets suggest that F-actin fibers passing through the center of the platelet is more efficient at generating high-magnitude forces.

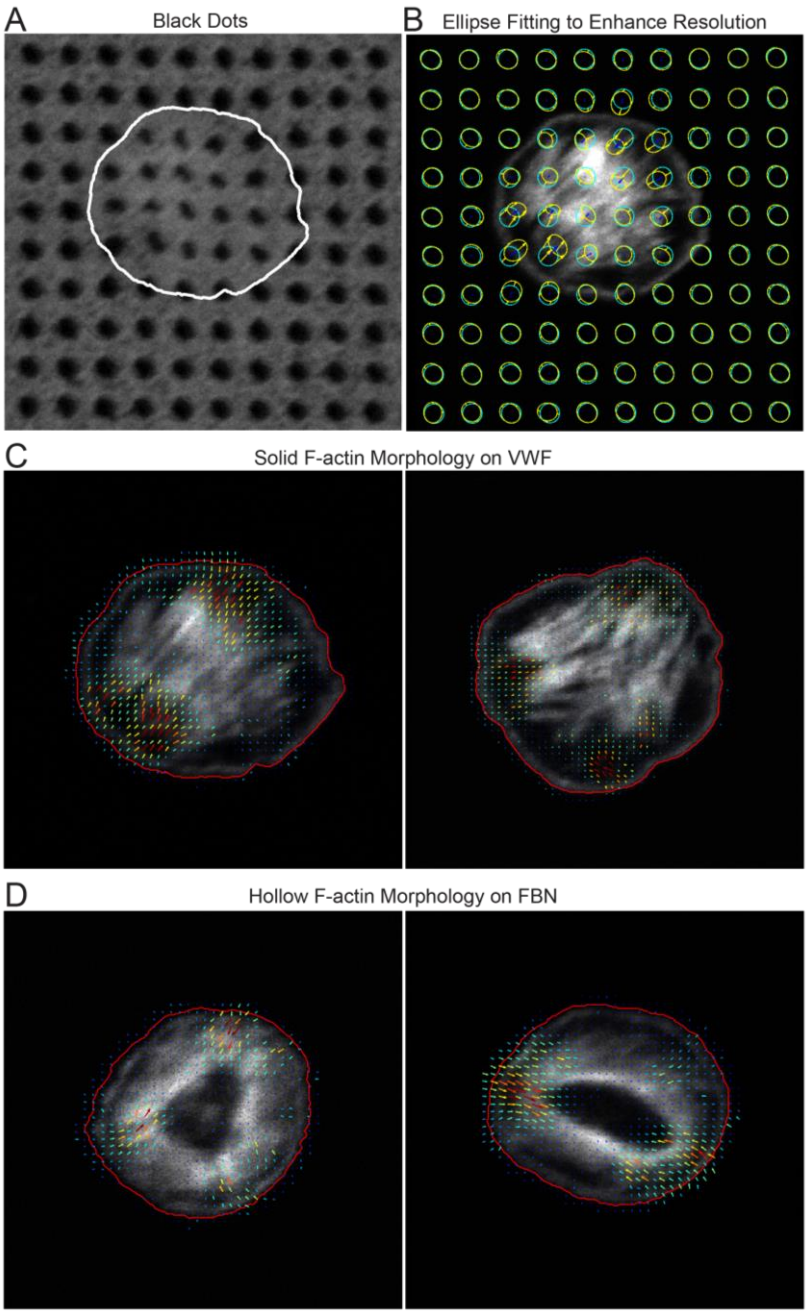

Figure 26 – Higher resolution force analysis reveals correspondence between F-actin structure and subcellular force localization.
(A-B) Dots beneath the platelet (cell boundary shown in white) are deformed in the raw black dots image. (B) Calculation of the deformations was improved upon by ellipses (yellow) to the deformed dots. This results in four displacement vectors per black dot (yellow arrows) instead of one displacement vector at the dot centroid (blue arrows). (C-D) Higher force resolution enabled subcellular mapping of F-actin morphology with force on VWF (C) and fibrinogen (D).

5.4 Discussion

Hollow and nodule platelet F-actin morphologies commonly observed on fibrinogen have been described and characterized[9,10,12,13,19,139,140], leading to understanding of altered cytoskeletal structure in disease states[10,12], dynamics of platelet spreading[10,19], and co-localization of F-actin with cell markers of interest[10,140]. While some previous studies have conducted spreading assays on VWF and published images of platelets with solid F-actin morphology[5,21,132], to our knowledge, differences in F-actin morphology between VWF and fibrinogen have not been measured in side-by-side nor discussed in the literature.

Here, we examined F-actin structure of washed platelets on fibrinogen and VWF and observed unique morphologies that are identifiable via machine learning. Our data agree with previous studies that observe nodules and hollow F-actin morphology on fibrinogen, yet we find that these morphologies are almost completely absent on VWF. Instead, platelets on VWF have an inverse F-actin structure, with F-actin localized in the platelet center. In addition to differences in F-actin structure on fibrinogen and VWF, we observed differences in function, wherein single platelets on VWF produce more force and more force per area than platelets on fibrinogen. Additionally, because black dots enables co-measurement of force generation and immunofluorescent stains, we were able to co-visualize F-actin structure and subcellular force generation, finding that platelet F-actin morphology corresponds with subcellular force localization.

Fibrinogen and VWF both contain the RGD adhesive motif that engages integrin $\alpha_{IIb}\beta_3$. Additionally, VWF contains the A1 domain that binds to GPIb. Due to this additional adhesive motif on VWF, we hypothesize that these differences in cytoskeletal morphology and force generation are GPIb-mediated. Further studies are needed to test this hypothesis.

5.5 Author Contributions

This chapter is a manuscript *in preparation* with authors Molly Y. Mollica, Kevin M. Beussman, Adithan Kandansamy, Junmei Chen, Krithika Manohar, José López, Wendy E. Thomas*, Nathan J. Sniadecki*. *co-corresponding

MYM performed the blood collection, experiments, F-actin morphology and total platelet force analysis, and statistics. K.M.B. and K.M. performed the machine learning methodology. A.K. performed the subcellular force analysis. J.C. and J.L. provided helpful experimental design and feedback. M.Y.M., W.E.T., and N.J.S. designed the experiments, interpreted the data, and wrote the manuscript.

Chapter VI: Discussion and Outlook

Black dots and measuring cellular force generation

Cells produce forces to perform functions such as migration and contraction. Since the first cellular force measurements in the 1980s, methodology has been invented and improved, facilitating quantitative measurements of cellular forces during functions such as maturation or contraction, in healthy and disease states, and in the presence or absence of key cellular markers or external stimuli. Despite the development of these techniques and understanding gained by them, existing techniques have limitations in 1) capabilities, such as yield/throughput (i.e. quantity of cells able to be measured per unit or time) or compatibility with other measurements of interest, 2) manufacturing limitations, such as required clean room preparation, necessary specialized equipment, slow/unscalable manufacturing, or high cost, and/or 3) other technical difficulties, such as challenges in computational analysis or inadvertent impact on cellular functions.

Black dots addresses substantial capability limitations including facilitating higher yields (~5-20X the number of cells/sample included in average studies) and co-measurement of immunofluorescent stains without constraining cell spreading. Ultimately, black dots enabled the first high-yield, high-resolution analysis of platelet force generation, including identification of biophysical factors that associate with force generation, determination of the effects of platelet storage conditions on function, and identification of unique cytoskeletal morphologies induced by different key blood proteins. As a result of the high yield of data obtainable with black dots, approaches including multivariate mixed effects modeling, K-means clustering, and machine learning were able to be used.

While black dots provides substantial improvements in capabilities, its use is not yet wide-spread and future steps would enhance its likelihood of adoption by other research groups. The first black dots manufacturing step requires a single, reusable master structure made in a clean room; all subsequent

steps are performed at the benchtop using standard and relatively inexpensive lab equipment. Looking to the future, manufacturing black dots master structures in bulk and distributing them at cost (approximately $100 each) would enhance the accessibility of this technique, making it possible for labs without clean room access or expertise to perform single-cell force measurements. A follow-up study using black dots to measure single-cell forces of numerous cell types and documenting the optimal conditions and optimization process for each cell type would also support the democratization of the black dots technique. Additionally, improvements in the accessibility of the analysis such as transferring the MATLAB code to a graphical user interface suitable for those without MATLAB experience, would assist in the broad usability of black dots.

An ideal, future system may further increase yield/throughput, spatial resolution, temporal resolution, and other capabilities while simultaneously decreasing cost, manufacturing or complexities, and other technical challenges. In particular, while black dots substantially improves yield and allows for co-measurement of immunofluorescent stains, it does so at the cost of temporal resolution. While it is possible to measure dynamics of force generation by taking images of live cells on the black dots at numerous time points, this substantially decreases the number of cells able to be measured in one experiment. Improvements to black dots may make it possible to measure high-yield, high-spatial resolution, and high-temporal resolution cellular forces without constraining cell shape, allowing for stronger understanding of dynamics of force generation and heterogeneity in force over time. Additionally, an ideal, future single-cell force measurement technique would be versatile to many cell types (of varying size, strength, and functions) and easy to use, making it affordable and accessible to labs with wide-ranging fields and expertise. As improved techniques continue to address limitations, reducing technical challenges and cost, cellular forces could become a clinical measure of cell function in platelets and other cells. In particular, if future studies support platelet forces as an ultrasensitive measure of bleeding and/or thrombosis risk, at-home platelet force measurement systems similar to blood glucose monitors would be of interest.

Platelet forces have basic science and clinical significance

In this work, we identify platelet spread area, shape (circularity), and F-actin dispersion as biophysical factors that independently and cooperatively associate with platelet forces. Additionally, we measure the forces of stored platelets and find that after 5 days of cold storage, platelets produce larger platelet plugs but not significantly different plug or average single-platelet forces. Finally, we characterize unique cytoskeletal structures and significantly different forces induced by key blood proteins. Identifying factors that associate with platelet forces, characterizing effects of storage temperature on platelet force generation, and elucidating platelets' complex reaction to activating proteins has implications in bleeding, clotting, and transfusion medicine.

Future work could directly build upon this by further investigating factors that associate with platelet forces (e.g. quantity or localization of cell markers of interest, circulation time), characterizing storage at additional timepoints or in other storage conditions, and/or identifying the mechanism of the observed cytoskeletal differences. Additional future studies could examine how donor factors (e.g. age, sex), disease states (e.g. diabetes, kidney disease, von Willebrand Disease), or anti-platelet medications associate with platelet binding, spreading, shape, structure, and/or contraction. Toward the use of platelet forces as a clinical measurement, future studies should also investigate how measurements from established clinical assays such as thromboelastography, light transmission platelet aggregation, or PFA-100 compare and contrast with single-platelet forces for healthy donors and disease states. Uniquely, high-yield single-platelet force measurements have the potential to investigate how subsets of high force or low force platelets may contribute to hemostasis and thrombosis. Ultimately, the development of black dots with the ability to co-measure high-yield, high-resolution single-platelet forces and cell markers of interest enables wide-ranging studies with basic science and potential clinical significance.

References

(1) Ting, L. H.; Feghhi, S.; Taparia, N.; Smith, A. O.; Karchin, A.; Lim, E.; John, A. S.; Wang, X.; Rue, T.; White, N. J.; Sniadecki, N. J. Contractile Forces in Platelet Aggregates under Microfluidic Shear Gradients Reflect Platelet Inhibition and Bleeding Risk. *Nat. Commun.* **2019**, *10* (1), 1–10. https://doi.org/10.1038/s41467-019-09150-9.

(2) Myers, D. R.; Qiu, Y.; Fay, M. E.; Tennenbaum, M.; Chester, D.; Cuadrado, J.; Sakurai, Y.; Baek, J.; Tran, R.; Ciciliano, J. C.; Ahn, B.; Mannino, R. G.; Bunting, S. T.; Bennett, C.; Briones, M.; Fernandez-Nieves, A.; Smith, M. L.; Brown, A. C.; Sulchek, T.; Lam, W. A. Single-Platelet Nanomechanics Measured by High-Throughput Cytometry. *Nat. Mater.* **2017**, *16* (2), 230–235. https://doi.org/10.1038/nmat4772.

(3) Hanke, J.; Ranke, C.; Perego, E.; Köster, S. Human Blood Platelets Contract in Perpendicular Direction to Shear Flow. *Soft Matter* **2019**, *15* (9), 2009–2019. https://doi.org/10.1039/C8SM02136H.

(4) Lam, W. A.; Chaudhuri, O.; Crow, A.; Webster, K. D.; Li, T.-D. De; Kita, A.; Huang, J.; Fletcher, D. A. Mechanics and Contraction Dynamics of Single Platelets and Implications for Clot Stiffening. *Nat. Mater.* **2011**, *10* (1), 61–66. https://doi.org/10.1038/nmat2903.

(5) Feghhi, S.; Munday, A. D.; Tooley, W. W.; Rajsekar, S.; Fura, A. M.; Kulman, J. D.; Ló pez, J. A.; Sniadecki, N. J.; López, J. A.; Sniadecki, N. J.; Ló pez, J. A.; Sniadecki, N. J. Glycoprotein Ib-IX-V Complex Transmits Cytoskeletal Forces That Enhance Platelet Adhesion. *Biophys. J.* **2016**, *111* (3), 301–308. https://doi.org/10.1016/j.bpj.2016.06.023.

(6) Schwarz Henriques, S.; Sandmann, R.; Strate, A.; Kö Ster, S. Force Field Evolution during Human Blood Platelet Activation. *J. Cell Sci.* **2012**, *125*, 3914–3920. https://doi.org/10.1242/jcs.108126.

(7) Hanke, J.; Probst, D.; Zemel, A.; Schwarz, U. S.; Kö, S. Dynamics of Force Generation by Spreading Platelets. *Soft Matter* **2018**, *14*, 6571. https://doi.org/10.1039/c8sm00895g.

(8) Oshinowo, O.; Copeland, R.; Sakurai, Y.; Fay, M. E.; Petrich, B. G.; Leong, T.; Brainard, B.; Lam, W. A. Significant Differences in Single-Platelet Biophysics Exist across Species but Attenuate during Clot Formation Key Points. *Blood Adv.* **2021**, *5* (2), 432–437. https://doi.org/10.1182/bloodadvances.2020003755.

(9) CALAMINUS, S. D. J.; THOMAS, S.; McCARTY, O. J. T.; MACHESKY, L. M.; WATSON, S. P. Identification of a Novel, Actin-Rich Structure, the Actin Nodule, in the Early Stages of Platelet Spreading. *J. Thromb. Haemost.* **2008**, *6* (11), 1944–1952. https://doi.org/10.1111/J.1538-7836.2008.03141.X.

(10) Lickert, S.; Sorrentino, S.; Studt, J.-D.; Medalia, O.; Vogel, V.; Schoen, I. Morphometric Analysis of Spread Platelets Identifies Integrin AIIbβ3-Specific Contractile Phenotype. *Sci. Rep.* **2018**, *8* (1), 5428. https://doi.org/10.1038/s41598-018-23684-w.

(11) Thornber, K.; McCarty, O. J. T.; Watson, S. P.; Pears, C. J. Distinct but Critical Roles for Integrin AIIbβ 3 in Platelet Lamellipodia Formation on Fibrinogen, Collagen-Related Peptide and Thrombin. *FEBS J.* **2006**, *273* (22), 5032–5043. https://doi.org/10.1111/j.1742-4658.2006.05500.x.

(12) Poulter, N. S.; Pollitt, A. Y.; Davies, A.; Malinova, D.; Nash, G. B.; Hannon, M. J.; Pikramenou, Z.; Rappoport, J. Z.; Hartwig, J. H.; Owen, D. M.; Thrasher, A. J.; Watson, S. P.; Thomas, S. G. Platelet Actin Nodules Are Podosome-like Structures Dependent on Wiskott-Aldrich Syndrome Protein and ARP2/3 Complex. *Nat. Commun.* **2015**. https://doi.org/10.1038/ncomms8254.

(13) Hagmann, J. Pattern Formation and Handedness in the Cytoskeleton of Human Platelets. *Proc. Natl. Acad. Sci. U. S. A.* **1993**, *90* (8), 3280–3283. https://doi.org/10.1073/pnas.90.8.3280.

(14) Mangin, P.; Yuan, Y.; Goncalves, I.; Eckly, A.; Freund, M.; Cazenave, J. P.; Gachet, C.; Jackson,

S. P.; Lanza, F. Signaling Role for Phospholipase Cγ2 in Platelet Glycoprotein Ibα Calcium Flux and Cytoskeletal Reorganization: Involvement of a Pathway Distinct from FcRγ Chain and FcγRIIA. *J. Biol. Chem.* **2003**, *278* (35), 32880–32891. https://doi.org/10.1074/jbc.M302333200.

(15) Horev, M. B.; Zabary, Y.; Zarka, R.; Sorrentino, S.; Medalia, O.; Zaritsky, A.; Geiger, B. Differential Dynamics of Early Stages of Platelet Adhesion and Spreading on Collagen IV- and Fibrinogen-Coated Surfaces. *F1000Research* **2020**, *9*, 449. https://doi.org/10.12688/f1000research.23598.1.

(16) Schurr, Y.; Sperr, A.; Volz, J.; Beck, S.; Reil, L.; Kusch, C.; Eiring, P.; Bryson, S.; Sauer, M.; Nieswandt, B.; Machesky, L.; Bender, M. Platelet Lamellipodium Formation Is Not Required for Thrombus Formation and Stability. *Blood* **2019**, *134* (25), 2318–2329. https://doi.org/10.1182/BLOOD.2019002105.

(17) Bender, M.; Palankar, R. Platelet Shape Changes during Thrombus Formation: Role of Actin-Based Protrusions. *Hamostaseologie* **2021**, *41* (01), 014–021. https://doi.org/10.1055/a-1325-0993.

(18) Qiu, Y.; Brown, A. C.; Myers, D. R.; Sakurai, Y.; Mannino, R. G.; Tran, R.; Ahn, B.; Hardy, E. T.; Kee, M. F.; Kumar, S.; Bao, G.; Barker, T. H.; Lam, W. A. Platelet Mechanosensing of Substrate Stiffness during Clot Formation Mediates Adhesion, Spreading, and Activation. *Proc. Natl. Acad. Sci. U. S. A.* **2014**, *111* (40), 14430–14435. https://doi.org/10.1073/pnas.1322917111.

(19) Paknikar, A. K.; Eltzner, B.; Köster, S. Direct Characterization of Cytoskeletal Reorganization during Blood Platelet Spreading. *Prog. Biophys. Mol. Biol.* **2019**, *144*, 166–176. https://doi.org/10.1016/j.pbiomolbio.2018.05.001.

(20) Thomas, S. G. *The Structure of Resting and Activated Platelets*; 2019. https://doi.org/10.1016/B978-0-12-813456-6.00003-5.

(21) Yuan, Y.; Kulkarni, S.; Ulsemer, P.; Cranmer, S. L.; Yap, C. L.; Nesbitt, W. S.; Harper, I.; Mistry, N.; Dopheide, S. M.; Hughan, S. C.; Williamson, D.; De La Salle, C.; Salem, H. H.; Lanza, F.; Jackson,

S. P. The von Willebrand Factor-Glycoprotein Ib/V/IX Interaction Induces Actin Polymerization and Cytoskeletal Reorganization in Rolling Platelets and Glycoprotein Ib/V/IX-Transfected Cells. *J. Biol. Chem.* **1999**, *274*, 36241–36251. https://doi.org/10.1074/jbc.274.51.36241.

(22) Fletcher, D. A.; Mullins, R. D. Cell Mechanics and the Cytoskeleton. *Nature*. Nature Publishing Group January 2010, pp 485–492. https://doi.org/10.1038/nature08908.

(23) Janmey, P. A.; McCulloch, C. A. Cell Mechanics: Integrating Cell Responses to Mechanical Stimuli. *Annu. Rev. Biomed. Eng.* **2007**, *9* (1), 1–34. https://doi.org/10.1146/annurev.bioeng.9.060906.151927.

(24) Guck, J.; Lautenschläger, F.; Paschke, S.; Beil, M. Critical Review: Cellular Mechanobiology and Amoeboid Migration. *Integr. Biol.* **2010**, *2* (11–12), 575–583. https://doi.org/10.1039/c0ib00050g.

(25) Miller, C. J.; Davidson, L. A. The Interplay between Cell Signalling and Mechanics in Developmental Processes. *Nat. Rev. Genet.* **2013**, *14* (10), 733–744. https://doi.org/10.1038/nrg3513.

(26) Kai, F. B.; Laklai, H.; Weaver, V. M. Force Matters: Biomechanical Regulation of Cell Invasion and Migration in Disease. *Trends Cell Biol.* **2016**, *26* (7), 486–497. https://doi.org/10.1016/j.tcb.2016.03.007.

(27) Murrell, M.; Oakes, P. W.; Lenz, M.; Gardel, M. L. Forcing Cells into Shape: The Mechanics of Actomyosin Contractility. *Nat. Rev. Mol. Cell Biol.* **2015**, *16* (8), 486–498. https://doi.org/10.1038/nrm4012.

(28) Katta, S.; Krieg, M.; Goodman, M. B. Feeling Force: Physical and Physiological Principles Enabling Sensory Mechanotransduction. *Annu. Rev. Cell Dev. Biol.* **2015**, *31* (1), 347–371. https://doi.org/10.1146/annurev-cellbio-100913-013426.

(29) Harris, A. K.; Wild, P.; Stopak, D. Silicone Rubber Substrata: A New Wrinkle in the Study of Cell

Locomotion Author(s): Albert K. Harris, Patricia Wild and David Stopak Source: *Science (80-.).* **1980**, *208* (4440), 177–179.

(30) Harris, A. K.; Stopak, D.; Wild, P. Fibroblast Traction as a Mechanism for Collagen Morphogenesis. *Nature* **1981**, *290* (March).

(31) Burton, K.; Taylor, D. L. Traction Forces of Cytokinesis Measured with Optically Modified Elastic Substrata. *Lett. to Nat.* **1997**, *385*, 450–454.

(32) Burton, K.; Park, J. H.; Taylor, D. L. Keratocytes Generate Traction Forces in Two Phases. *Mol. Biol. Cell* **1999**, *10* (11), 3745–3769. https://doi.org/10.1091/mbc.10.11.3745.

(33) Helfman, D. M.; Levy, E. T.; Berthier, C.; Shtutman, M.; Riveline, D.; Grosheva, I.; Lachish-Zalait, A.; Elbaum, M.; Bershadsky, A. D. Caldesmon Inhibits Nonmuscle Cell Contractility and Interferes with the Formation of Focal Adhesions. *Mol. Biol. Cell* **1999**, *10* (10), 3097–3112. https://doi.org/10.1091/mbc.10.10.3097.

(34) Hinz, B.; Celetta, G.; Tomasek, J. J.; Gabbiani, G.; Chaponnier, C. Alpha-Smooth Muscle Actin Expression Upregulates Fibroblast Contractile Activity. *Mol. Biol. Cell* **2001**, *12* (9), 2730–2741. https://doi.org/10.1091/mbc.12.9.2730.

(35) Lee, J.; Leonard, M.; Oliver, T.; Ishihara, A.; Jacobson, K. Traction Forces Generated by Locomoting Keratocytes. *J. Cell Biol.* **1994**, *127* (6 II), 1957–1964. https://doi.org/10.1083/jcb.127.6.1957.

(36) Oliver, T.; Dembo, M.; Jacobson, K. Traction Forces in Locomoting Cells. *Cell Motil. Cytoskeleton* **1995**, 225–240. https://doi.org/10.1108/eb025354.

(37) Dembo, M.; Oliver, T.; Ishihara, A.; Jacobson, K. Imaging the Traction Stresses Exerted by Locomoting Cells with the Elastic Substratum Method. *Biophys. J.* **1996**, *70* (4), 2008–2022. https://doi.org/10.1016/S0006-3495(96)79767-9.

(38) Gutierrez, E.; Tkachenko, E.; Besser, A.; Sundd, P.; Ley, K.; Danuser, G.; Ginsberg, M. H.; Groisman, A. High Refractive Index Silicone Gels for Simultaneous Total Internal Reflection Fluorescence and Traction Force Microscopy of Adherent Cells. *PLoS One* **2011**, *6* (9), 1–5. https://doi.org/10.1371/journal.pone.0023807.

(39) Balaban, N. Q.; Schwarz, U. S.; Riveline, D.; Goichberg, P.; Tzur, G.; Sabanay, I.; Mahalu, D.; Safran, S.; Bershadsky, A.; Addadi, L.; Geiger, B. Force and Focal Adhesion Assembly: A Close Relationship Studied Using Elastic Micropatterned Substrates. *Nat. Cell Biol.* **2001**, *3* (5), 466–472. https://doi.org/10.1038/35074532.

(40) Bergert, M.; Lendenmann, T.; Zündel, M.; Ehret, A. E.; Panozzo, D.; Richner, P.; Kim, D. K.; Kress, S. J. P.; Norris, D. J.; Sorkine-Hornung, O.; Mazza, E.; Poulikakos, D.; Ferrari, A. Confocal Reference Free Traction Force Microscopy. *Nat. Commun.* **2016**, *7*. https://doi.org/10.1038/ncomms12814.

(41) Pelham, R.; Wang, L.-L. Cell Locomotion and Focal Adhesions Are Regulated by Substrate Flexibility. *Proc. Natl. Acad. Sci. U. S. A.* **1997**, *94*, 13661–13665.

(42) Wang, Y.-L.; PELHAM, R. J. Preparation of a Flexible, Porous Polyacrylamide Substrate for Mechanical Studies of Cultured Cells. *Methods Enzymol.* **1998**, *298* (1995), 489–496.

(43) Munevar, S.; Wang, Y. L.; Dembo, M. Traction Force Microscopy of Migrating Normal and H-Ras Transformed 3T3 Fibroblasts. *Biophys. J.* **2001**, *80* (4), 1744–1757. https://doi.org/10.1016/S0006-3495(01)76145-0.

(44) Polio, S. R.; Rothenberg, K. E.; Stamenović, D.; Smith, M. L. A Micropatterning and Image Processing Approach to Simplify Measurement of Cellular Traction Forces. *Acta Biomater.* **2012**, *8* (1), 82–88. https://doi.org/10.1016/j.actbio.2011.08.013.

(45) Polio, S. R.; Parameswaran, H.; Canović, E. P.; Gaut, C. M.; Aksyonova, D.; Stamenović, D.; Smith,

M. L. Topographical Control of Multiple Cell Adhesion Molecules for Traction Force Microscopy. *Integr. Biol. (United Kingdom)* **2014**, *6* (3), 357–365. https://doi.org/10.1039/c3ib40127h.

(46) Tseng, P.; Di Carlo, D. Substrates with Patterned Extracellular Matrix and Subcellular Stiffness Gradients Reveal Local Biomechanical Responses. *Adv. Mater.* **2014**, *26* (8), 1242–1247. https://doi.org/10.1002/adma.201304607.

(47) Myers, D. R.; Qiu, Y.; Fay, M. E.; Tennenbaum, M.; Chester, D.; Cuadrado, J.; Sakurai, Y.; Baek, J.; Tran, R.; Ciciliano, J. C.; Ahn, B.; Mannino, R. G.; Bunting, S. T.; Bennett, C.; Briones, M.; Fernandez-Nieves, A.; Smith, M. L.; Brown, A. C.; Sulchek, T.; Lam, W. A. Single-Platelet Nanomechanics Measured by High-Throughput Cytometry. *Nat. Mater.* **2017**. https://doi.org/10.1038/nmat4772.

(48) Califano, J. P.; Reinhart-King, C. A. Substrate Stiffness and Cell Area Predict Cellular Traction Stresses in Single Cells and Cells in Contact. *Cell. Mol. Bioeng.* **2010**, *3* (1), 68–75. https://doi.org/10.1007/s12195-010-0102-6.

(49) Kandow, C. E.; Georges, P. C.; Janmey, P. A.; Beningo, K. A. Polyacrylamide Hydrogels for Cell Mechanics: Steps Toward Optimization and Alternative Uses. *Methods Cell Biol.* **2007**, *83* (07), 29–46. https://doi.org/10.1016/S0091-679X(07)83002-0.

(50) Wang, H. B.; Dembo, M.; Hanks, S. K.; Wang, Y. L. Focal Adhesion Kinase Is Involved in Mechanosensing during Fibroblast Migration. *Proc. Natl. Acad. Sci. U. S. A.* **2001**, *98* (20), 11295–11300. https://doi.org/10.1073/pnas.201201198.

(51) Maskarinec, S. A.; Franck, C.; Tirrell, D. A.; Ravichandran, G. Quantifying Cellular Traction Forces in Three Dimensions. *Proc. Natl. Acad. Sci. U. S. A.* **2009**, *106* (52), 22108–22113. https://doi.org/10.1073/pnas.0904565106.

(52) Oakes, P. W.; Patel, D. C.; Morin, N. A.; Zitterbart, D. P.; Fabry, B.; Reichner, J. S.; Tang, J. X.

Neutrophil Morphology and Migration Are Affected by Substrate Elasticity. *Blood* **2009**, *114* (7), 1387–1395. https://doi.org/10.1182/blood-2008-11-191445.

(53) Rape, A. D.; Guo, W.; Wang, Y. The Regulation of Traction Force in Relation to Cell Shape and Focal Adhesions. *Biomaterials* **2011**, *32* (8), 2043–2051. https://doi.org/10.1016/j.biomaterials.2010.11.044.

(54) Reinhart-King, C. A.; Dembo, M.; Hammer, D. A. The Dynamics and Mechanics of Endothelial Cell Spreading. *Biophys. J.* **2005**, *89* (1), 676–689. https://doi.org/10.1529/biophysj.104.054320.

(55) Ribeiro, A. J. S.; Denisin, A. K.; Wilson, R. E.; Pruitt, B. L. For Whom the Cells Pull: Hydrogel and Micropost Devices for Measuring Traction Forces. *Methods* **2016**, *94*, 51–64. https://doi.org/10.1016/j.ymeth.2015.08.005.

(56) Shiu, Y. T.; Li, S.; Marganski, W. A.; Usami, S.; Schwartz, M. A.; Wang, Y. L.; Dembo, M.; Chien, S. Rho Mediates the Shear-Enhancement of Endothelial Cell Migration and Traction Force Generation. *Biophys. J.* **2004**, *86* (4), 2558–2565. https://doi.org/10.1016/S0006-3495(04)74311-8.

(57) Stroka, K. M.; Aranda-Espinoza, H. Neutrophils Display Biphasic Relationship between Migration and Substrate Stiffness. *Cell Motil. Cytoskeleton* **2009**, *66* (6), 328–341. https://doi.org/10.1002/cm.20363.

(58) Tay, C. Y.; Wu, Y. L.; Cai, P.; Tan, N. S.; Venkatraman, S. S.; Chen, X.; Tan, L. P. Bio-Inspired Micropatterned Hydrogel to Direct and Deconstruct Hierarchical Processing of Geometry-Force Signals by Human Mesenchymal Stem Cells during Smooth Muscle Cell Differentiation. *NPG Asia Mater.* **2015**, *7* (7), 1–11. https://doi.org/10.1038/am.2015.66.

(59) Gjorevski, N.; Nelson, C. M. Mapping of Mechanical Strains and Stresses around Quiescent Engineered Three-Dimensional Epithelial Tissues. *Biophys. J.* **2012**, *103* (1), 152–162. https://doi.org/10.1016/j.bpj.2012.05.048.

(60) Steinwachs, J.; Metzner, C.; Skodzek, K.; Lang, N.; Thievessen, I.; Mark, C.; Münster, S.; Aifantis, K. E.; Fabry, B. Three-Dimensional Force Microscopy of Cells in Biopolymer Networks. *Nat. Methods* **2016**, *13* (2), 171–176. https://doi.org/10.1038/nmeth.3685.

(61) Engler, A.; Bacakova, L.; Newman, C.; Hategan, A.; Griffin, M.; Discher, D. Substrate Compliance versus Ligand Density in Cell on Gel Responses. *Biophys. J.* **2004**, *86* (1), 617–628. https://doi.org/10.1016/S0006-3495(04)74140-5.

(62) Pelham, R. J.; Wang, Y. L. Cell Locomotion and Focal Adhesions Are Regulated by Substrate Flexibility. *Proc. Natl. Acad. Sci. U. S. A.* **1997**, *94* (25), 13661–13665. https://doi.org/10.1073/pnas.94.25.13661.

(63) Legant, W. R.; Miller, J. S.; Blakely, B. L.; Cohen, D. M.; Genin, G. M.; Chen, C. S. Measurement of Mechanical Tractions Exerted by Cells in Three-Dimensional Matrices. *Nat. Methods* **2010**, *7* (12), 969–971. https://doi.org/10.1038/nmeth.1531.

(64) Miller, J. S.; Shen, C. J.; Legant, W. R.; Baranski, J. D.; Blakely, B. L.; Chen, C. S. Bioactive Hydrogels Made from Step-Growth Derived PEG–Peptide Macromers. *Biomaterials* **2010**, *31* (13), 3736–3743. https://doi.org/10.1016/j.biomaterials.2010.01.058.

(65) Legant, W. R.; Choi, C. K.; Miller, J. S.; Shao, L.; Gao, L.; Betzig, E.; Chen, C. S. Multidimensional Traction Force Microscopy Reveals Out-of-Plane Rotational Moments about Focal Adhesions. *Proc. Natl. Acad. Sci. U. S. A.* **2013**, *110* (3), 881–886. https://doi.org/10.1073/pnas.1207997110.

(66) Yang, M. T.; Fu, J.; Wang, Y. K.; Desai, R. A.; Chen, C. S. Assaying Stem Cell Mechanobiology on Microfabricated Elastomeric Substrates with Geometrically Modulated Rigidity. *Nat. Protoc.* **2011**, *6* (2), 187–213. https://doi.org/10.1038/nprot.2010.189.

(67) Tan, J. L.; Tien, J.; Pirone, D. M.; Gray, D. S.; Bhadriraju, K.; Chen, C. S. Cells Lying on a Bed of Microneedles.Pdf. *Proc. Natl. Acad. Sci.* **2002**, *100* (4), 1484–1489.

https://doi.org/10.1073/pnas.0235407100.

(68) Kim, D.; Wong, P. K.; Park, J.; Levchenko, A.; Sun, Y. Microengineered Platforms for Cell Mechanobiology. **2009**, 203–234. https://doi.org/10.1146/annurev-bioeng-061008-124915.

(69) Butler, J. P.; Toli-Nørrelykke, I. M.; Fabry, B.; Fredberg, J. J. Traction Fields, Moments, and Strain Energy That Cells Exert on Their Surroundings. *Am. J. Physiol. - Cell Physiol.* **2002**, *282* (3 51-3), 595–605. https://doi.org/10.1152/ajpcell.00270.2001.

(70) Sabass, B.; Gardel, M. L.; Waterman, C. M.; Schwarz, U. S. High Resolution Traction Force Microscopy Based on Experimental and Computational Advances. *Biophys. J.* **2008**, *94* (1), 207–220. https://doi.org/10.1529/biophysj.107.113670.

(71) Li, B.; Xie, L.; Starr, Z. C.; Yang, Z.; Lin, J. S.; Wang, J. H. C. Development of Micropost Force Sensor Array with Culture Experiments for Determination of Cell Traction Forces. *Cell Motil. Cytoskeleton* **2007**, *64* (7), 509–518. https://doi.org/10.1002/cm.20200.

(72) Fuard, D.; Tzvetkova-Chevolleau, T.; Decossas, S.; Tracqui, P.; Schiavone, P. Optimization of Poly-Di-Methyl-Siloxane (PDMS) Substrates for Studying Cellular Adhesion and Motility. *Microelectron. Eng.* **2008**, *85* (5–6), 1289–1293. https://doi.org/10.1016/j.mee.2008.02.004.

(73) Cheng, Q.; Sun, Z.; Meininger, G. A.; Almasri, M. Note: Mechanical Study of Micromachined Polydimethylsiloxane Elastic Microposts. *Rev. Sci. Instrum.* **2010**, *81* (10), 2008–2011. https://doi.org/10.1063/1.3488461.

(74) Ghassemi, S.; Rossier, O.; Sheetz, M. P.; Wind, S. J.; Hone, J. Gold-Tipped Elastomeric Pillars for Cellular Mechanotransduction. *J. Vac. Sci. Technol. B Microelectron. Nanom. Struct.* **2009**, *27* (6), 3088. https://doi.org/10.1116/1.3259953.

(75) Taylor, R. E.; Kim, K.; Sun, N.; Park, S. J.; Sim, J. Y.; Fajardo, G.; Bernstein, D.; Wu, J. C.; Pruitt,

B. L. Sacrificial Layer Technique for Axial Force Post Assay of Immature Cardiomyocytes. *Biomed. Microdevices* **2013**, *15* (1), 171–181. https://doi.org/10.1007/s10544-012-9710-3.

(76) Desai, R. A.; Yang, M. T.; Sniadecki, N. J.; Legant, W. R.; Chen, C. S. Microfabricated Post-Array-Detectors (MPADs): An Approach to Isolate Mechanical Forces. *J. Vis. Exp.* **2007**, No. 8, 1–5. https://doi.org/10.3791/311.

(77) Tooley, W. W.; Feghhi, S.; Han, S. J.; Wang, J.; Sniadecki, N. J. Thermal Fracture of Oxidized Polydimethylsiloxane during Soft Lithography of Nanopost Arrays. *J. Micromechanics Microengineering* **2011**, *21* (5), 054013. https://doi.org/10.1088/0960-1317/21/5/054013.

(78) Grayson, A. C. R.; Shawgo, R. S.; Johnson, A. M.; Flynn, N. T.; Li, Y.; Cima, M. J.; Langer, R. A BioMEMS Review: MEMS Technology for Physiologically Integrated Devices. *Proc. IEEE* **2004**, *92* (1), 6–21. https://doi.org/10.1109/JPROC.2003.820534.

(79) Petersen, K. E. Silicon as a Mechanical Material. *Micromechanics MEMS Class. Semin. Pap. to 1990* **1997**, *70* (5), 58–95. https://doi.org/10.1109/9780470545263.sect1.

(80) Hopcroft, M. A.; Nix, W. D.; Kenny, T. W. What Is the Young's Modulus of Silicon? *J. Microelectromechanical Syst.* **2010**, *19* (2), 229–238. https://doi.org/10.1109/JMEMS.2009.2039697.

(81) Madou, M. J. *Fundamentals of Microfabrication*; 2002. https://doi.org/10.1201/9781482274004.

(82) Galbraith, C. G.; Sheetz, M. P. A Micromachined Device Provides a New Bend on Fibroblast Traction Forces. *Proc. Natl. Acad. Sci. U. S. A.* **1997**, *94* (17), 9114–9118. https://doi.org/10.1073/pnas.94.17.9114.

(83) Jagannathan Rajagopalan; Alireza Tofangchi; Saif, M. T. A. Drosophila Neurons Actively Regulate Axonal Tension in Vivo. *Biophys. J.* **2010**, *99* (10), 3208–3215.

https://doi.org/10.1016/j.bpj.2010.09.029.

(84) Haase, K.; Pelling, A. E. Investigating Cell Mechanics with Atomic Force Microscopy. *J. R. Soc. Interface* **2015**, *12* (104). https://doi.org/10.1098/rsif.2014.0970.

(85) Polacheck, W. J.; Chen, C. S. Measuring Cell-Generated Forces: A Guide to the Available Tools. *Nat. Methods* **2016**, *13* (5), 415–423. https://doi.org/10.1038/nmeth.3834.

(86) Petersen, N. O.; McConnaughey, W. B.; Elson, E. L. Dependence of Locally Measured Cellular Deformability on Position on the Cell, Temperature, and Cytochalasin B. *Proc. Natl. Acad. Sci.* **1982**, *79* (17), 5327–5331. https://doi.org/10.1073/pnas.79.17.5327.

(87) Chaudhuri, O.; Parekh, S. H.; Lam, W. A.; Fletcher, D. A. Combined Atomic Force Microscopy and Side-View Optical Imaging for Mechanical Studies of Cells. *Nat. Methods* **2009**, *6* (5), 383–387. https://doi.org/10.1038/nmeth.1320.

(88) Tortonese, M. Marco Tortonese. *Eng. Med. Biol.* **1997**, No. April.

(89) Kirmizis, D.; Logothetidis, S. Atomic Force Microscopy Probing in the Measurement of Cell Mechanics. *Int. J. Nanomedicine* **2010**, *5* (1), 137–145. https://doi.org/10.2147/ijn.s5787.

(90) Alonso, J. L.; Goldmann, W. H. Feeling the Forces: Atomic Force Microscopy in Cell Biology. *Life Sci.* **2003**, *72* (23), 2553–2560. https://doi.org/10.1016/S0024-3205(03)00165-6.

(91) Lam, W. A.; Chaudhuri, O.; Crow, A.; Webster, K. D.; Li, T. De; Kita, A.; Huang, J.; Fletcher, D. A. Mechanics and Contraction Dynamics of Single Platelets and Implications for Clot Stiffening. *Nat. Mater.* **2011**. https://doi.org/10.1038/nmat2903.

(92) Zemel, A.; De, R.; Safran, S. A. Mechanical Consequences of Cellular Force Generation. *Current Opinion in Solid State and Materials Science*. Elsevier Ltd October 2011, pp 169–176. https://doi.org/10.1016/j.cossms.2011.04.001.

(93) Roca-Cusachs, P.; Conte, V.; Trepat, X. Quantifying Forces in Cell Biology. *Nat. Cell Biol.* **2017**, *19* (7), 742–751. https://doi.org/10.1038/ncb3564.

(94) Obenaus*, A. M.; Mollica*, M. Y.; Sniadecki, N. J. (De)Form and Function: Measuring Cellular Forces with Deformable Materials and Deformable Structures. *Adv. Healthc. Mater.* **2020**, *9* (8), 1–16. https://doi.org/10.1002/adhm.201901454.

(95) Lee, J.; Leonard, M.; Oliver, T.; Ishihara, A.; Jacobson, K. Traction Forces Generated by Locomoting Keratocytes. *J. Cell Biol.* **1994**, *127* (6 II), 1957–1964. https://doi.org/10.1083/jcb.127.6.1957.

(96) Dembo, M.; Wang, Y. L. Stresses at the Cell-to-Substrate Interface during Locomotion of Fibroblasts. *Biophys. J.* **1999**, *76* (4), 2307–2316. https://doi.org/10.1016/S0006-3495(99)77386-8.

(97) Schwarz, U. S.; Soiné, J. R. D. Traction Force Microscopy on Soft Elastic Substrates: A Guide to Recent Computational Advances. *Biochim. Biophys. Acta - Mol. Cell Res.* **2015**, *1853* (11), 3095–3104. https://doi.org/10.1016/j.bbamcr.2015.05.028.

(98) Pushkarsky, I.; Tseng, P.; Black, D.; France, B.; Warfe, L.; Koziol-White, C. J.; Jester, W. F.; Trinh, R. K.; Lin, J.; Scumpia, P. O.; Morrison, S. L.; Panettieri, R. A.; Damoiseaux, R.; Di Carlo, D. Elastomeric Sensor Surfaces for High-Throughput Single-Cell Force Cytometry. *Nat. Biomed. Eng.* **2018**, *2* (2), 1. https://doi.org/10.1038/s41551-018-0207-0.

(99) Griffin, B. P.; Largaespada, C. J.; Rinaldi, N. A.; Lemmon, C. A. A Novel Method for Quantifying Traction Forces on Hexagonal Micropatterned Protein Features on Deformable Poly-Dimethyl Siloxane Sheets. *MethodsX* **2019**, *6*, 1343–1352. https://doi.org/10.1016/j.mex.2019.05.011.

(100) Ono, A.; Westein, E.; Hsiao, S.; Nesbitt, W. S.; Hamilton, J. R.; Schoenwaelder, S. M.; Jackson, S. P. Identification of a Fibrin-Independent Platelet Contractile Mechanism Regulating Primary Hemostasis and Thrombus Growth. *Blood* **2008**, *112* (1), 90–99. https://doi.org/10.1182/blood-2007-12-127001.

(101) Tutwiler, V.; Litvinov, R. I.; Lozhkin, A. P.; Peshkova, A. D.; Lebedeva, T.; Ataullakhanov, F. I.; Spiller, K. L.; Cines, D. B.; Weisel, J. W. Kinetics and Mechanics of Clot Contraction Are Governed by the Molecular and Cellular Composition of the Blood. *Blood* **2016**, *127* (1), 149–159. https://doi.org/10.1182/blood-2015-05-647560.

(102) Williams, E. K.; Oshinowo, O.; Ravindran, A.; Lam, W. A.; Myers, D. R. Feeling the Force: Measurements of Platelet Contraction and Their Diagnostic Implications. *Semin. Thromb. Hemost.* **2019**, *45* (3), 285–296. https://doi.org/10.1055/s-0038-1676315.

(103) White, J. G. Platelet Structure. In *Platelets*; 2007; pp 45–73. https://doi.org/10.1016/B978-012369367-9/50765-5.

(104) Hechler, B.; Dupuis, A.; Mangin, P. H.; Gachet, C. Platelet Preparation for Function Testing in the Laboratory and Clinic: Historical and Practical Aspects. *Res. Pract. Thromb. Haemost.* **2019**, *3* (4), 615–625. https://doi.org/10.1002/rth2.12240.

(105) Hanke, J.; Ranke, C.; Perego, E.; Köster, S. Human Blood Platelets Contract in Perpendicular Direction to Shear Flow. *Soft Matter* **2019**, *15* (9), 2009–2019. https://doi.org/10.1039/c8sm02136h.

(106) Yu, H.; Xiong, S.; Tay, C. Y.; Leong, W. S.; Tan, L. P. A Novel and Simple Microcontact Printing Technique for Tacky, Soft Substrates and/or Complex Surfaces in Soft Tissue Engineering. *Acta Biomater.* **2012**, *8* (3), 1267–1272. https://doi.org/10.1016/j.actbio.2011.09.006.

(107) MacNearney, D.; Mak, B.; Ongo, G.; Kennedy, T. E.; Juncker, D. Nanocontact Printing of Proteins on Physiologically Soft Substrates to Study Cell Haptotaxis. *Langmuir* **2016**, *32* (50), 13525–13533. https://doi.org/10.1021/acs.langmuir.6b03246.

(108) Palchesko, R. N.; Zhang, L.; Sun, Y.; Feinberg, A. W. Development of Polydimethylsiloxane Substrates with Tunable Elastic Modulus to Study Cell Mechanobiology in Muscle and Nerve. *PLoS One* **2012**, *7* (12), e51499. https://doi.org/10.1371/journal.pone.0051499.

(109) Rodriguez, M. L.; Beussman, K. M.; Chun, K. S.; Walzer, M. S.; Yang, X.; Murry, C. E.; Sniadecki, N. J. Substrate Stiffness, Cell Anisotropy, and Cell–Cell Contact Contribute to Enhanced Structural and Calcium Handling Properties of Human Embryonic Stem Cell-Derived Cardiomyocytes. *ACS Biomater. Sci. Eng.* **2019**, acsbiomaterials.8b01256. https://doi.org/10.1021/acsbiomaterials.8b01256.

(110) Blair, D.; Dufresne, E. The Matlab Particle Tracking Code Repository. *Part. code available http//physics. Georg. edu/matlab* **2008**.

(111) Han, S. J.; Oak, Y.; Groisman, A.; Danuser, G. Traction Microscopy to Identify Force Modulation in Subresolution Adhesions. *Nat. Methods* **2015**, *12* (7), 653–656. https://doi.org/10.1038/nmeth.3430.

(112) Pike, J. A.; Simms, V. A.; Smith, C. W.; Morgan, N. V.; Khan, A. O.; Poulter, N. S.; Styles, I. B.; Thomas, S. G. An Adaptable Analysis Workflow for Characterization of Platelet Spreading and Morphology. *Platelets* **2020**. https://doi.org/10.1080/09537104.2020.1748588.

(113) Carr, M. E.; Carr, S. L. Fibrin Structure and Concentration Alter Clot Elastic Modulus but Do Not Alter Platelet Mediated Force Development. *Blood Coagul. Fibrinolysis* **1995**, *6* (1), 79–86. https://doi.org/10.1097/00001721-199502000-00013.

(114) Chen, Z.; Lu, J.; Zhang, C.; Hsia, I.; Yu, X.; Marecki, L.; Marecki, E.; Asmani, M.; Jain, S.; Neelamegham, S.; Zhao, R. Microclot Array Elastometry for Integrated Measurement of Thrombus Formation and Clot Biomechanics under Fluid Shear. *Nat. Commun.* **2019**, *10* (1), 2051. https://doi.org/10.1038/s41467-019-10067-6.

(115) Lickert, S.; Sorrentino, S.; Studt, J. D.; Medalia, O.; Vogel, V.; Schoen, I. Morphometric Analysis of Spread Platelets Identifies Integrin AIIbβ3-Specific Contractile Phenotype. *Sci. Rep.* **2018**, *8* (1), 5428. https://doi.org/10.1038/s41598-018-23684-w.

(116) Tolić-Nørrelykke, I. M.; Wang, N. Traction in Smooth Muscle Cells Varies with Cell Spreading. *J.*

Biomech. **2005**, *38* (7), 1405–1412. https://doi.org/10.1016/j.jbiomech.2004.06.027.

(117) Tan, J. L.; Tien, J.; Pirone, D. M.; Gray, D. S.; Bhadriraju, K.; Chen, C. S. Cells Lying on a Bed of Microneedles: An Approach to Isolate Mechanical Force. *Proc. Natl. Acad. Sci.* **2003**, *100* (4), 1484–1489. https://doi.org/10.1073/pnas.0235407100.

(118) FDA. *Fatalities Reported to FDA Following Blood Collection and Transfusion Annual Summary for FY2017*; 2017.

(119) Dumont, L. J.; Kleinman, S.; Murphy, J. R.; Lippincott, R.; Schuyler, R.; Houghton, J.; Metzel, P. BLOOD COMPONENTS: Screening of Single-Donor Apheresis Platelets for Bacterial Contamination: The PASSPORT Study Results. *Transfusion* **2010**, *50* (3), 589–599. https://doi.org/10.1111/J.1537-2995.2009.02460.X.

(120) Getz, T. M.; Montgomery, R. K.; Bynum, J. A.; Aden, J. K.; Pidcoke, H. F.; Cap, A. P. Storage of Platelets at 4°C in Platelet Additive Solutions Prevents Aggregate Formation and Preserves Platelet Functional Responses. *Transfusion* **2016**, *56* (6), 1320–1328. https://doi.org/10.1111/trf.13511.

(121) Reddoch, K. M.; Montgomery, R. K.; Rodriguez, A. C.; Meledeo, M. A.; Pidcoke, H. F.; Ramasubramanian, A. K.; Cap, A. P. Endothelium-Derived Inhibitors Efficiently Attenuate the Aggregation and Adhesion Responses of Refrigerated Platelets. *Shock* **2016**, *45* (2), 220–227. https://doi.org/10.1097/SHK.0000000000000493.

(122) Pidcoke, H. F.; Spinella, P. C.; Ramasubramanian, A. K.; Strandenes, G.; Hervig, T.; Ness, P. M.; Cap, A. P. Refrigerated Platelets for the Treatment of Acute Bleeding. *Shock* **2014**, *41* (Supplement 1), 51–53. https://doi.org/10.1097/SHK.0000000000000078.

(123) Nair, P. M.; Pidcoke, H. F.; Cap, A. P.; Ramasubramanian, A. K. Effect of Cold Storage on Shear-Induced Platelet Aggregation and Clot Strength. *J. Trauma Acute Care Surg.* **2014**, *77* (3), S88–S93. https://doi.org/10.1097/TA.0000000000000327.

(124) Montgomery, R. K.; Reddoch, K. M.; Evani, S. J.; Cap, A. P.; Ramasubramanian, A. K. Enhanced Shear-Induced Platelet Aggregation Due to Low-Temperature Storage. *Transfusion* **2013**, *53* (7), 1520–1530. https://doi.org/10.1111/j.1537-2995.2012.03917.x.

(125) Reddoch, K. M.; Pidcoke, H. F.; Montgomery, R. K.; Fedyk, C. G.; Aden, J. K.; Ramasubramanian, A. K.; Cap, A. P. Hemostatic Function of Apheresis Platelets Stored at 4°C and 22°C. *Shock* **2014**, *41* (Supplement 1), 54–61. https://doi.org/10.1097/SHK.0000000000000082.

(126) Becker, G. A.; Tuccelli, M.; Kunicki, T.; Chalos, M. K.; Aster, R. H. Studies of Platelet Concentrates Stored at 22 C and 4 C. *Transfusion* **1973**, *13* (2), 61–68. https://doi.org/10.1111/j.1537-2995.1973.tb05442.x.

(127) Johnson, L.; Tan, S.; Wood, B.; Davis, A.; Marks, D. C. Refrigeration and Cryopreservation of Platelets Differentially Affect Platelet Metabolism and Function: A Comparison with Conventional Platelet Storage Conditions. *Transfusion* **2016**, *56* (7), 1807–1818. https://doi.org/10.1111/trf.13630.

(128) Six, K. R.; Devloo, R.; Compernolle, V.; Feys, H. B. Impact of Cold Storage on Platelets Treated with Intercept Pathogen Inactivation. *Transfusion* **2019**, *59* (8), 2662–2671. https://doi.org/10.1111/trf.15398.

(129) KM, H.; H, F.; A, T.; KL, B.; TP, S.; JH, H. Mechanisms of Cold-Induced Platelet Actin Assembly. *J. Biol. Chem.* **2001**, *276* (27), 24751–24759. https://doi.org/10.1074/JBC.M011642200.

(130) Winokur, Rebecca, Hartwig, J. H. Mechanism of Shape Change in Chilled Human Platelets | Elsevier Enhanced Reader. *Blood* **1995**.

(131) Woulfe, D.; Jiang, H.; Morgans, A.; Monks, R.; Birnbaum, M.; Brass, L. F. Defects in Secretion, Aggregation, and Thrombus Formation in Platelets from Mice Lacking Akt2. *J. Clin. Invest.* **2004**, *113* (3), 441. https://doi.org/10.1172/JCI20267.

(132) Beussman*, K. M.; Mollica*, M. Y.; Leonard, A.; Miles, J.; Hocter, J.; Song, Z.; Stolla, M.; Han, S. J.; Emery, A.; Thomas, W. E.; Sniadecki, N. J. Black Dots: High-Yield Traction Force Microscopy Reveals Structural Factors Contributing to Platelet Forces. *Acta Biomater.* **2021**, 1–38. https://doi.org/10.1016/j.actbio.2021.11.013.

(133) Miles, J.; Bailey, S. L.; Obenaus, A. M.; Mollica, M. Y.; Usaneerungrueng, C.; Byrne, D.; Fang, L.; Flynn, J. R.; Corson, J.; Osborne, B.; Houck, K.; Wang, Y.; Shen, Y.; Fu, X.; Dong, J.-F.; Sniadecki, N. J.; Stolla, M. Storage Temperature Determines Platelet GPVI Levels and Function in Mice and Humans. *Blood Adv.* **2021**, *5* (19), 3839–3849. https://doi.org/10.1182/bloodadvances.2021004692.

(134) Schwarz, U. S.; Balaban, N. Q.; Riveline, D.; Bershadsky, A.; Geiger, B.; Safran, S. A. Calculation of Forces at Focal Adhesions from Elastic Substrate Data: The Effect of Localized Force and the Need for Regularization. *Biophys. J.* **2002**, *83* (3), 1380–1394. https://doi.org/10.1016/S0006-3495(02)73909-X.

(135) Huang, Y.; Schell, C.; Huber, T. B.; Şimşek, A. N.; Hersch, N.; Merkel, R.; Gompper, G.; Sabass, B. Traction Force Microscopy with Optimized Regularization and Automated Bayesian Parameter Selection for Comparing Cells. *Sci. Reports 2019 91* **2019**, *9* (1), 1–16. https://doi.org/10.1038/s41598-018-36896-x.

(136) Nier, V.; Jain, S.; Lim, C. T.; Ishihara, S.; Ladoux, B.; Marcq, P. Inference of Internal Stress in a Cell Monolayer. *Biophys. J.* **2016**, *110* (7), 1625–1635. https://doi.org/10.1016/J.BPJ.2016.03.002.

(137) Molina, R.; Katsaggelos, A. K.; Mateos, J. Bayesian and Regularization Methods for Hyperparameter Estimation in Image Restoration. *IEEE Trans. Image Process.* **1999**, *8* (2), 231–246. https://doi.org/10.1109/83.743857.

(138) Szegedy, C.; Vanhoucke, V.; Ioffe, S.; Shlens, J. Rethinking the Inception Architecture for Computer Vision. *Proc. IEEE Conf. Comput. Vis. Pattern Recognit.* **2016**, 2818–2826.

(139) Hagmann, J.; Grob, M.; Welman, A.; Van Willigen, G.; Burger, M. M. Recruitment of the LIM Protein Hic-5 to Focal Contacts of Human Platelets. *J. Cell Sci.* **1998**, *111* (15), 2181–2188.

(140) Zarka, R.; Horev, M. B.; Volberg, T.; Neubauer, S.; Kessler, H.; Spatz, J. P.; Geiger, B. Differential Modulation of Platelet Adhesion and Spreading by Adhesive Ligand Density. *Nano Lett* **2019**, *19*. https://doi.org/10.1021/acs.nanolett.8b03513.

(141) Sniadecki, N. J.; Chen, C. S. Microfabricated Silicone Elastomeric Post Arrays for Measuring Traction Forces of Adherent Cells. *Methods Cell Biol.* **2007**, *83* (07), 313–328. https://doi.org/10.1016/S0091-679X(07)83013-5.

(142) Beussman, K. M.; Rodriguez, M. L.; Leonard, A.; Taparia, N.; Thompson, C. R.; Sniadecki, N. J. Micropost Arrays for Measuring Stem Cell-Derived Cardiomyocyte Contractility. *Methods* **2016**, *94*, 43–50. https://doi.org/10.1016/j.ymeth.2015.09.005.

(143) Mangin, P. H.; Onselaer, M.-B.; Receveur, N.; Lay, N. Le; Hardy, A. T.; Wilson, C.; Sanchez, X.; Loyau, S.; Dupuis, A.; Babar, A. K.; Miller, J. L.; Philippou, H.; Hughes, C. E.; Herr, A. B.; Ariëns, R. A.; Mezzano, D.; Jandrot-Perrus, M.; Gachet, C.; Watson, S. P. Immobilized Fibrinogen Activates Human Platelets through Glycoprotein VI. *Haematologica* **2018**, *103* (5), 898. https://doi.org/10.3324/HAEMATOL.2017.182972.

Appendix A: Bad Blood – Blood Research's Perpetuation of Racism & Standards Moving Forward

Racism has long intersected and been reinforced by blood research including conceptual invention of "pure-bloodness", inclusion of overtly racist remarks about the temperament of different races within scientific publications, and use of blood type data as evidence for the inception of biological races. While blood research's historical perpetuation of racism is egregious, it isn't ancient history – it continues today. In recent studies, race is commonly treated as a biological variable, identification and mention of racism is avoided, and race is commonly confounded with genetics or ancestry. As blood researchers, we should recognize how our field has historically and continues to perpetuate racism and determine standards moving forward.

The perpetuation of racism by blood research

In the early 1900s, Dr. Karl Landsteiner mixed blood components from different donors and found two opposite results: sometimes the blood remained an unchanged blood drop while other times, it clumped together so obviously that the difference is visible by the untrained, naked eye. This observation was the foundation for the A, B, O blood typing system we have today and led to widespread successful blood transfusions [1].

Soon after the identification of blood types, interest grew in the frequency of blood types by race. Drs. Ludwik and Hanka Hirschfeld divided blood donors into three groups:

- "European Type" which included "Italian, German, Austrian, Bulgarian, Serbian, and Greek",
- "Intermediate Type" which included "Arab, Turk, Russian, and Jew", and
- "Asio-African Type" which included "Malagasy, Negro, Annamese, and Indian."

The Hirschfields invented a “biochemical race index” and defined it as the ratio of people of some race with Type A to B blood, wherein the highest scores were in northern European people and the lowest in Asian and African people. Disguised as science, the Hirschfield’s studies have racist assumptions and characterizations weaved throughout their paper. Their results casually discuss the “anatomical characteristics, mode of life, occupation, and temperament” of races and whether these racial characteristics trend with their biochemical race index. They ultimately conclude that the existence of Type A and B blood and their biochemical race index results suggest two hypotheses about the beginning of humanity. First, “when man appeared on the Earth, A and B were present in the same proportions in different races” and that the frequencies changed over time. They conclude that this hypothesis is “improbable”. Second, that that “two different biochemical races” arose in different places and the frequencies of Type A and B are due to “mutual infiltration of these races” [2]. These hypotheses are grounded in the false assumption that race is biological [3-4] and the authors conflate frequency of blood types, race, and ancestry throughout their work. Nonetheless, the notion that blood types are evidence of distinct biological races was perpetuated by blood researchers for decades and published in even the most esteemed journals, such as *Science* [5].

Even in blood studies not explicitly examining or drawing any conclusions about race, race is often still a part of the data collection and reporting without explanation as to the reasoning. In a study on the heredity of blood types, blood types of mothers and children were studied. Next to about half of the families, an asterisk is placed indicating which families were “Negro families” [6]. Additionally, papers by leaders in the field causally dismissed data that did not support their hypotheses with notions of “pure bloodedness” and assumption that biological race exists. For example, Dr. Alexander Wiener writes “the explanation for the large deviation in the Chinese series is that not all the Chinese tested were full-blooded [and] it is quite possible that some individuals were included where there had been crossing with other races” [7].

TABLE V
Mother-Child Combinations

No.	Mother	Children			
1*	A_2MNRh_2	A_2MNRh ♀			
2	A_1MRh_1	$BMNRh_1$♂	$A_1MNRh_1Rh_2$ ♀	$A_1MNRh_1Rh_2$ ♀	$BMRh_1Rh_2$ ♀
3*	$OMNRh_1$	$OMNRh$ ♀			
4	$OMNRh$-	A_1MRh_1 ♀	$OMNRh$ ♀		
5*	$ONRh$-	$ONRh$♂			
6*	$BNRh$	$BNRh_1$ ♀			
7	$OMNRh_1$	$OMRh_1$ ♀	$OMNRh_1$♂		
8	$OMNRh_1$	$OMNRh_1$ ♀	A_2NRh_1♂	A_1MNRh_1 ♀	A_1NRh_1 ♀
9*	$BNRh_1$	A_1BNRh_1			
10	$BMNRh_1$	$BMNRh_1$ ♀	$BMNRh_1$ ♀		
11*	A_1MNRh_2	A_1MRh ♀			
12	$OMNRh_1Rh_2$	$ONRh_1$ ♀	$OMNRh_1$♂	$A_{1,2}MRh_1$♂	$A_{1,2}NRh_1Rh_2$♂
13	$OMNRh$-	A_1MNRh_1 ♀			
14	$A_1BMNRh_1Rh_2$	$A_1NRh_1Rh_2$ ♀	A_1MRh_1♂		
15	$BMNRh_1$	$OMNRh_1$♂	$ONRh_1$♂		
16	$OMRh_1$	$OMRh_1$♂			
17	A_1MNRh_1	$OMNRh_1$♂	A_1MNRh_1♂	A_1MRh_1 ♀	
18	A_1BMRh_1	A_1MRh♂			
19	A_1NRh_1	A_2BMNRh_1♂			
20‡	$ONRh$-	A_1MNRh-♂	A_1MNRh_1 ♀		
21	A_1BMNRh_1	A_1BMNRh-♂			
22*	A_1MNRh	A_1BMRh_2♂	A_1MRh_2 ♀		
23	$OMNRh_1Rh_2$	$OMRh_1Rh_2$ ♀	$ONRh_1$♂	$OMRh_1$ ♀	
24*	$BNRh_2$	$ONRh$ ♀	$OMNRh_2$ ♀	$BNRh$♂	
25	$OMNRh_2$	$ONRh_1$ ♀			
26	A_2MNRh_2	A_2BMRh_2♂			
27	$OMNRh$-	$ONRh_2$♂			
28*	$OMNRh$	$OMNRh$♂			
29	$BMNRh_1$	$BMNRh_1$ ♀			
30	A_2MRh-	A_2MNRh_1			
31	$OMRh_1$	$A_1MNRh_1Rh_2$♂			
32*	$BNRh_1$	$BNRh$ ♀	$BMNRh$♂		
33*	$OMNRh$-	$OMRh$- ♀			
34	A_1MRh_1	$OMRh_1$ ♀			
35	$A_1MNRh_1Rh_2$	$A_1NRh_1Rh_2$♂			
36*§	$OMNRh_1$	$A_1MRh_1Rh_2$♂	$OMRh_1Rh_2$ ♀	$OMNRh$ ♀	$A_1MRh_1Rh_2$ ♀
		$OMNRh_1Rh_2$♂	$ONRh_1Rh_2$♂		
37	$OMNRh$-	$OMNRh_1$♂	$OMNRh_1$ ♀		
38*	$OMNRh$	$ONRh$ ♀			
39	A_1MNRh_1	$BMNRh_1$ ♀	A_1BMNRh-♂		
40*	A_1MNRh_1	A_1MNRh_1♂	A_1MNRh_1 ♀		
41	A_1MNRh_1	$OMNRh_1$♂‖	$OMNRh_1$♂‖		
42*	A_1NRh	A_2NRh♂			
43*	A_1MRh_1	$OMRh_1$♂			
44	$A_1MNRh_1Rh_2$	$OMNRh_1Rh_2$ ♀	$ONRh_1Rh_2$♂	A_1MNRh_1 ♀	
45	$BNRh_1Rh_2$	$BMNRh_1$			
46	$BMRh_2$	$OMRh_2$ ♀			
47	A_1BNRh_1	$BMNRh_1$♂	A_1NRh_1♂		
48	A_1MNRh_2	$OMNRh_2$♂			
49*	$BNRh$-	$ONRh$♂	$ONRh$ ♀		
50*	$BMRh_1Rh_2$	$BMNRh_1$♂	$BMNRh_1$♂	$OMNRh_1Rh_2$ ♀	
51	A_1MNRh_1	A_1MNRh_1♂	A_1MNRh-♂		
52	$A_2NRh_1Rh_2$	A_2MNRh_1♂	A_1MNRh_1 ♀	A_2MNRh_2 ♀	
53*	A_1MNRh	A_1MNRh♂	A_1MNRh_2♂	A_1MRh♂	
54*	$OMNRh$	$BMRh$♂			
55	$BMRh'$	$OMRh_2$♂	A_1MNRh'		
56	A_1MRh_2	A_1MRh_2♂	$OMRh$-♂	$OMRh_1Rh_2$ ♀	$OMRh_1Rh_2$♂
		$OMRh_2$♂	$OMRh_2$ ♀		
57	$OMRh_2$	$OMNRh_1$♂			
58*	A_1MRh_2	$OMRh$ ♀	A_1MRh_2 ♀	A_1MNRh♂	A_1MRh_2♂

* Negro families.
‡ Younger child in this family had erythroblastosis.
§ The last two children of this family resulted from a different father.
‖ Identical twins.

Racism is interweaved in blood research beyond blood types, heredity studies, and rationalization of biological races. While direct blood transfusions were relatively widely successful by 1940, collecting blood from a donor and storing it for later continued to be a technical challenge. It was unknown how stored blood changed over time and what measures could be taken to preserve the function of blood during storage. Dr. Charles Drew took on this problem in his doctorate research. He analyzed stored blood over time, characterizing changes in potassium, sodium, pH, and blood cell counts and examining how conditions of blood draw such as presence of anticoagulants and the blood draw container affect function after storage. Due to only a few medical schools accepting Black applicants and other forms of systemic racism, only 2% of physicians were Black in 1940 [8-9]. As a Black physician, Dr. Charles Drew was largely outnumbered by his white colleagues who were commonly publishing overt racism amongst their science.

Notably, in his 356-page dissertation, Dr. Drew brings up race twice: first, where he describes the blood type findings above. He correctly points out, “A survey of the literature indicates that men of all races have agglutinogens common to mankind in general. Given a blood sample, there is at present no agglutination test which will alone elucidate the race of the donor.” Second, in Dr. Drew’s trial blood bank program, he mentions that race is a variable collected for each blood donor [10].

Dr. Drew’s trial blood bank program that eventually became the model of modern blood banks and in 1941, the Red Cross Blood Donor Program launched, and Dr. Drew became the medical director of the first blood bank. Although all scientific evidence supported the fact that blood type – not race – is what matters when matching blood donors and recipients, the Red Cross initially excluded Black blood donors. Dr. Drew publicly criticized this discrimination and called it “unscientific and insulting to African Americans.” When the program did begin to accept Black donors in 1942, it segregated the blood [11-12].

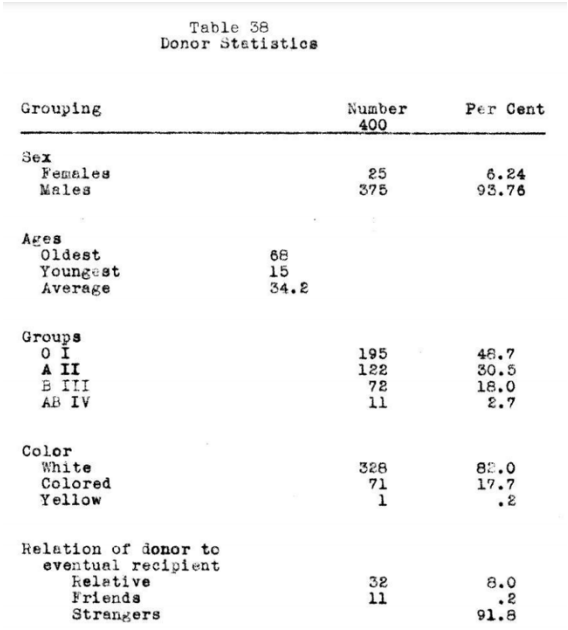

Table 38
Donor Statistics

Grouping		Number 400	Per Cent
Sex			
Females		25	6.24
Males		375	93.76
Ages			
Oldest	68		
Youngest	15		
Average	34.2		
Groups			
O I		195	48.7
A II		122	30.5
B III		72	18.0
AB IV		11	2.7
Color			
White		328	82.0
Colored		71	17.7
Yellow		1	.2
Relation of donor to eventual recipient			
Relative		32	8.0
Friends		11	.2
Strangers			91.8

Dr. Drew said of this, “It is fundamentally wrong for any great nation to willfully discriminate against such a large group of its people… It is unfortunate that such a worthwhile and scientific bit of work should have been hampered by such stupidity” [8]. The Red Cross continued to require labeling blood by race until 1950 and some states continued this requirement until 1972 [11].

Treating race as a biological variable is not ancient history in our field. In the last years, 35 articles have been published in the prestigious journal *Blood* that mention race or ethnicity while only one article mentions racism. It is still routine for peer-reviewed publications in our field to treat race as a biological variable and/or to conflate race and ancestry. For example, an article published in *Blood* less than a year ago was titled “Racial variation in ITP prevalence and chronic disease phenotype suggests biological differences” where the authors investigate whether Black children have lower incidence “because of

differences in disease biology based on race and ethnicity" [13]. These authors conflate race and ancestry, treat race as a biological variable so directly that they include in the title of their paper, and fail to discuss the potential influence that systemic racism as a potential confounding factor of this health inequity. A *Blood* review published in 2020 states "this effect of race has been estimated to account for 7% of the total variance in von Willebrand Factor levels" [14] again treating race as a biological variable that accounts for a quantifiable biological difference.

Standards for inclusion of race or racial inequities in blood research

Medical doctors, researchers, and critical race scholars have provided guidelines that biomedical researchers should follow when including race or considering racial health inequities [15-16]. Some of these expert suggestions, as they relate to conducting and reviewing blood research include:

1. Race is a social, political construct and not a biological variable [3, 15-17], so the reason for its inclusion in a biomedical study should be specified. If the research includes blood collection from human subjects and race and/or ethnicity is collected, the justification for collecting this information should be provided to the study volunteers as well as in the publication. Choices of racial and/or ethnic categories should be selected carefully and defined clearly, since these terms do not have universal definitions. Publications should report whether subjects self-reported or were assigned racial and/or ethnic categories.
2. More genetic diversity exists within a racial group than between racial groups and race cannot be used as a substitute for genetics [3, 15-17]. Suggestion of genetic differences must be supported by genetic studies. Additionally, race should not be confounded with ancestry. When describing an ancestry-linked health disparity such a Sickle Cell Disease, it should be clear that this disparity is not due to race but rather is due to ancestry of regions with malaria such as sub-Saharan Africa, some parts of South America, India, Saudi Arabia, and some parts of the Mediterranean.
3. Health inequities are largely caused by racism and/or ancestry and it is appropriate to name racism in scientific studies. When describing why Black people have a higher stroke mortality rates than white people, racism should be named and systemic and institutional factors such as access to health insurance and regular healthcare, travel time to receive emergency care, and inequitable treatment from medical professionals should be a part of the discussion. Experts who

have studied racism and its intersections with and perpetuation by medicine should be referenced.

As a field, many blood researchers have perpetuated race as a biological variable, even going so far as to use blood type data as evidence for the inception of biological races. Overtly racist remarks about “temperament”, “anatomical characteristics”, and “pure-bloodedness” were published in scientific journals. Even in recent studies, race is frequently used as a biological variable, identification of racism is avoided, and race is commonly confounded with genetics or ancestry. Understanding of our field’s perpetuation of racism and incorporation of these guidelines into our study designs, communications with subjects/patients, publications of our findings, and peer reviews is a critical step in our role as researchers.

Appendix B References

[1] Landsteiner, Karl. “On Agglutination Phenomena of Normal Human Blood” *Wiener Klinische Wochenschrif*t 1901

[2] Hirschfeld, Ludwik, Hirschfeld, Hanka. “Serological Differences Between the Blood of Different Races” *The Lancet* 1919

[3] McChesney, Kay Young. “Teaching Diversity: The Science You Need to Know to Explain Why Race is Not Biological*” SAGE* 2015

[4] Roberts, Dorthy. “Fatal Intervention” 2012

[5] Wiener, Alexander S. “The RH Factor and Racial Origins” *Science* 1942

[6] Wiener, Alexander S., Sonn, Eve B., Belkin, Ruth B. “Heredity of the Rh Blood Types” *Journal of Experimental Biology and Medicine* 1943

[7] Wiener, Alexander S., Sonn, Eve B., Belkin, Ruth B. “Distribution and Heredity of the Human Blood Properties, A, B, M, N, P And Rh” *Journal of Immunology* 1945

[8] U.S. National Library of Medicine, National Institutes of Health, Profiles in Science: Charles R. Drew. https://profiles.nlm.nih.gov/spotlight/bg/feature/blood

[9] Ly, Dan P. “Historical Trends in the Representativeness and Incomes of Black Physicians, 1900-2018” *Journal of General Internal Medicine* 2021

[10] Drew, Charles R. “Banked Blood: A Study in Blood Preservation” Dissertation https://collections.nlm.nih.gov/catalog/nlm:nlmuid-101584649X142-doc 1940

[11] Guglielmo, Thomas A. (PBS) “Desegregating blood: A civil rights struggle to remember” 2018

[12] American Chemical Society, “Dr. Charles Richard Drew ‘Father of the Blood Bank’” https://www.acs.org/content/acs/en/education/whatischemistry/african-americans-in-sciences/charles-richard-drew.html

[13] Kim, Taylor Olmsted et al. "Racial variation in ITP prevalence and chronic disease phenotype suggests biological differences." *Blood* 2020

[14] Ward, Soracha, O’Sullivan, Jamie M., O’Donnell, Jamie S. “The relationship between ABO blood group, von Willebrand factor, and primary hemostasis” *Blood* 2020

[15] Kaplan, Judith B., Bennett, Trude. “Use of Race and Ethnicity in Biomedical Publication” *JAMA* 2003

[16] Boyd, Rhea W., Lindo, Edwin G., Weeks, Lachelle D., McLemore, Monica R. “On Racism: A New Standard For Publishing On Racial Health Inequities.” *Health Affairs* 2020

[17] Chada, Noor, Kane, Madeleine, Lim, Bernadette, Rowland, Brenly. “Towards the Abolition of Biological Race in Medicine: Transforming Clinical Education, Research, and Practice. https://www.instituteforhealingandjustice.org/executivesummary